KIT

Karlsruher Institut für Technologie

Gralmonium — Granular Aluminum Nano-Junction Fluxonium Qubit

Zur Erlangung des akademischen Grades eines

Doktors der Naturwissenschaften
(Dr. rer. nat.)

von der KIT-Fakultät für Physik des
Karlsruher Instituts für Technologie (KIT)

genehmigte
Dissertation

von

M.Sc. Dennis Rieger

"Science is the universe trying to reverse engineer itself."

— ANONYMOUS

Abstract

Quantum information processing is a rapidly developing area of research that involves using quantum mechanical phenomena to perform computational tasks and solve problems in fields such as cryptography, machine learning, and chemistry. Universal quantum computers are expected to be much faster than classical computers for certain types of calculations, but they also face significant challenges in terms of hardware design, error correction, and scaling up the size of the systems. Trying to overcome these challenges, various types of hardware architectures are actively explored. Instead of relying on a single platform, a promising route can be to combine the advantages of different types of quantum information hardware. Among these approaches are hybrid architectures involving superconducting quantum circuits and spin-based systems. However, they require superconducting circuits which are compatible with relatively large magnetic fields on the order of hundreds of mT.

The main result of this thesis is the implementation of a fluxonium superconducting quantum bit entirely made of the high-kinetic-inductance material granular aluminum (grAl). Owing to the critical field of grAl in the Tesla range, the single-layer grAl fluxonium, which we nickname *gralmonium*, is magnetic field compatible by design. This holds true even for the gralmonium tunnel junction, which is given by a lithographically defined, self-structured *grAl nano-junction* with $\sim (20\,\mathrm{nm})^3$ volume. Remarkably, based on the measured qubit spectrum, which is similar to that of a standard fluxonium, the current-phase relation (CφR) of the nano-junction is indistinguishable from the purely sinusoidal form expected for an idealized tunnel Josephson junction (JJ). The coherence times of the gralmonium are in the microsecond range, which is comparable to superconducting qubits based on conventional mesoscopic tunnel JJ. Interestingly, we observe spontaneous jumps of the value of the Josephson energy on timescales from milliseconds to days, which indicate that the gralmonium is sensitive to the nanometric grAl volume of the junction.

But how does the agreement of the grAl nano-junction with a sinusoidal CφR quantitatively compare to Al-AlO$_x$-Al mesoscopic tunnel JJs, commonly employed in superconducting qubits? In order to address this question, as a second result of the thesis, we analyze the magnitude of Josephson harmonics in standard tunnel JJs. While the idealized CφR is only expected to occur in the limit of vanishingly low-transparency channels in the barrier, a mesoscopic model of tunneling through an inhomogeneous AlO$_x$ barrier predicts percent-level contributions from higher Josephson harmonics. Indeed, the $\sin\varphi$ approximation fails to accurately describe the energy spectra of transmon artificial atoms across samples from various laboratories, and including higher harmonic contributions in the transmon Hamiltonian leads to orders of magnitude better agreement between measured and modeled

spectroscopy. The required relative magnitude of the second harmonic is in the percent range across the measured samples.

The fact that both coherence and CφR of the grAl nano-junction are compatible with standard tunnel JJs establishes the gralmonium and similar circuits as a promising platform for hybrid architectures. Moreover, the susceptibility of the gralmonium to the nano-junction and its vicinity can be utilized as a detector sensitive to interactions on the nanometer scale. On the other hand, the observation of Josephson harmonics in standard tunnel JJs opens a new chapter for the design, measurement and analysis of superconducting circuits. While this work focuses on the consequences for transmon qubits, the results prompt follow-up research for other circuits based on tunnel JJs. In the future, Josephson harmonics can not only serve as a powerful benchmark for tunnel barriers from a material science perspective but they can also be embraced as a tool for circuit design and for further improvements of readout and gate fidelities in superconducting quantum hardware.

Acknowledgements

After all this time, I look back and can only consider myself a lucky person. By a series of coincidental timings, I found myself doing research in one of the most exciting fields of our time and had the opportunity to work with extraordinary people. My deepest gratitude goes to everyone involved during these years. Starting with my master's project and even more so in my PhD, I had the honor to discover the best of two worlds both in science and in supervision. Mirroring the hybrid spirit of the project, it was a joy to experience the duality of perspectives, opinions and styles in navigating the academic landscape.

Wolfgang, thank you for being my Doktorvater. When I started my PhD, you showed such an unbelievable presence in the labs that I felt protected from anything that could ever go wrong. It was a true pleasure to work with such an exceptional figure in science and I learned so much from you. Without the luxury of your expertise in cryogenics, many of the results would not have been possible to achieve. Thank you for your guidance and mentorship throughout the years. You helped with new perspectives whenever needed, and with trust and patience when the next milestone was clear. I always felt encouraged and appreciated by you for my work and more than welcome to discuss anything at any time. How you are at least one step ahead of anyone and anything, will never stop to impress me!

Ioan, thank you for your supervision in this hybrid PhD journey. It was your first lecture at KIT that ignited my spark to work in quantum technology and laid the foundations for my research. Your skill and charisma in interacting with people is absolutely fascinating! Thank you for all the time spent improving talk slides or polishing papers, and thank you for your help to not only achieve results but also advertise them to the world. The fun atmosphere and discussions we had in your office and at (or on our trips to) conferences and seminars will be lasting memories.

Simon, there is no way I can express enough gratitude to you. We first met when you joined the group as a bachelor student with Patrick, and it was the start of something exceptional. Your investment in our joint projects was unlimited and they would in no way have been so successful without you. Over the years, we have grown from students to colleagues to friends and we have learned a lot from each other. Thank you and Jasmijn for making even the most-restricted pandemic times enjoyable with lunch at your place. The fact that we never really stopped this tradition is very telling. I truly wish for anyone to experience the level of synergy that we achieved together in sharing the daily workload, managing the labs, measuring and understanding results, and producing publications. I feel incredibly fortunate for having you at my side for most of my PhD.

Contents

List of Publications

Authors marked with † have contributed equally.

[1] **D. Rieger**†, S. Günzler†, M. Spiecker, P. Paluch, P. Winkel, L. Hahn, J. K. Hohmann, A. Bacher, W. Wernsdorfer, and I. M. Pop, "Granular aluminium nanojunction fluxonium qubit", Nat. Mater. **22**, 194–199 (2023).

[2] D. Willsch†, **D. Rieger**†, P. Winkel, M. Willsch, C. Dickel, J. Krause, Y. Ando, R. Lescanne, Z. Leghtas, N. T. Bronn, P. Deb, O. Lanes, Z. K. Minev, B. Dennig, S. Geisert, S. Günzler, S. Ihssen, P. Paluch, T. Reisinger, R. Hanna, J. H. Bae, P. Schüffelgen, D. Grützmacher, L. Buimaga-Iarinca, C. Morari, W. Wernsdorfer, D. P. DiVincenzo, K. Michielsen, G. Catelani, and I. M. Pop, "Observation of Josephson Harmonics in Tunnel Junctions", arXiv, `10.48550/arXiv.2302.09192` (2023).

[3] **D. Rieger**†, S. Günzler†, M. Spiecker, A. Nambisan, W. Wernsdorfer, and I. M. Pop, "Fano Interference in Microwave Resonator Measurements", Phys. Rev. Appl. **20**, 014059 (2023).

[4] K. Borisov, **D. Rieger**, P. Winkel, F. Henriques, F. Valenti, A. Ionita, M. Wessbecher, M. Spiecker, D. Gusenkova, I. M. Pop, and W. Wernsdorfer, "Superconducting granular aluminum resonators resilient to magnetic fields up to 1 Tesla", Appl. Phys. Lett. **117**, 120502 (2020).

[5] P. Winkel, K. Borisov, L. Grünhaupt, **D. Rieger**, M. Spiecker, F. Valenti, A. V. Ustinov, W. Wernsdorfer, and I. M. Pop, "Implementation of a Transmon Qubit Using Superconducting Granular Aluminum", Phys. Rev. X **10**, 031032 (2020).

[6] P. Winkel†, I. Takmakov†, **D. Rieger**, L. Planat, W. Hasch-Guichard, L. Grünhaupt, N. Maleeva, F. Foroughi, F. Henriques, K. Borisov, J. Ferrero, A. V. Ustinov, W. Wernsdorfer, N. Roch, and I. M. Pop, "Nondegenerate Parametric Amplifiers Based on Dispersion-Engineered Josephson-Junction Arrays", Phys. Rev. Appl. **13**, 024015 (2020).

[7] M. Spiecker, P. Paluch, N. Gosling, N. Drucker, S. Matityahu, D. Gusenkova, S. Günzler, **D. Rieger**, I. Takmakov, F. Valenti, P. Winkel, R. Gebauer, O. Sander, G. Catelani, A. Shnirman, A. V. Ustinov, W. Wernsdorfer, Y. Cohen, and I. M. Pop, "Two-level system hyperpolarization using a quantum Szilard engine", Nat. Phys. **19**, 1–6 (2023).

[8] D. Gusenkova, F. Valenti, M. Spiecker, S. Günzler, P. Paluch, **D. Rieger**, L.-M. Pioraş-Ţimbolmaş, L. P. Zârbo, N. Casali, I. Colantoni, A. Cruciani, S. Pirro, L. Cardani, A. Petrescu, W. Wernsdorfer, P. Winkel, and I. M. Pop, "Operating in a deep underground facility improves the locking of gradiometric fluxonium qubits at the sweet spots", Appl. Phys. Lett. **120**, 054001 (2022).

[9] D. Gusenkova, M. Spiecker, R. Gebauer, M. Willsch, D. Willsch, F. Valenti, N. Karcher, L. Grünhaupt, I. Takmakov, P. Winkel, **D. Rieger**, A. V. Ustinov, N. Roch, W. Wernsdorfer, K. Michielsen, O. Sander, and I. M. Pop, "Quantum Nondemolition Dispersive Readout of a Superconducting Artificial Atom Using Large Photon Numbers", Phys. Rev. Appl. **15**, 064030 (2021).

[10] I. Takmakov[†], P. Winkel[†], F. Foroughi, L. Planat, D. Gusenkova, M. Spiecker, **D. Rieger**, L. Grünhaupt, A. V. Ustinov, W. Wernsdorfer, I. M. Pop, and N. Roch, "Minimizing the Discrimination Time for Quantum States of an Artificial Atom", Phys. Rev. Appl. **15**, 064029 (2021).

List of Figures

List of Tables

Part I

Overview & Main Results

1 Introduction

This chapter introduces the key concepts of the manuscript. We start by motivating the idea of hybrid hardware implementations for quantum information processing. The next section focuses in more detail on superconducting circuits with the Josephson effect enabling the implementation of quantum bits such as transmon and fluxonium. After presenting the main advantages and limitations of superconducting hardware, the appeal of spin-based hybrid architectures is discussed. Finally, superconducting granular aluminum is introduced as a promising material to implement quantum circuits for hybrid applications involving magnetic field.

1.1 Motivation & Manuscript Overview

Quantum information processing has emerged as an exciting frontier in the field of information technology with the potential to revolutionize various industries and scientific disciplines [11–16]. In particular, the realization of universal quantum computing promises to exponentially speed up specific algorithms compared to classical computing methods [17–21]. Since fulfilling this promise can be considered the holy grail of quantum computing research, we should motivate briefly where the potential speed-up comes from. Interestingly, by doing so, it is possible to grasp both why quantum computing is powerful in theory and why realizing it in practice is a significant challenge.

How strongly particular quantum protocols and algorithms — such as Shor's factorization [22, 23] or Grover's search algorithm [24] — harness a quantum advantage over classical methods can be an intricate discussion even among tech giants [19, 25] and experts [26, 27]. Unarguably though, the fundamental ingredients at the heart of quantum information are *superposition* and *entanglement*. The first concept, superposition, is what is typically also discussed in popular media and refers to the fact that, in contrast to a classical bit, a quantum bit (qubit) can be in a superposition of its basis states,

$$|\Psi\rangle = \alpha\,|0\rangle + \beta\,|1\rangle\,, \quad \text{with } |\alpha|^2 + |\beta|^2 = 1\,. \tag{1.1}$$

The second ingredient, entanglement, contributes to the exponential scaling of the computational space. This can be seen by considering the state of a multi-qubit register with N qubits,

$$|\Psi\rangle = \alpha_0\,|00\ldots00\rangle + \alpha_1\,|00\ldots01\rangle + \ldots + \alpha_{(2^N-1)}\,|11\ldots11\rangle\,, \quad \text{with } \sum_i |\alpha_i|^2 = 1\,, \tag{1.2}$$

which is given by the superposition of all possible 2^N basis states. In this context, entanglement refers to the striking observation that the superposition state Eq. (1.2) of a quantum register contains states which are impossible to write as a product of the individual qubits composing the register: the qubits can be entangled, as for example in the state $|\Psi\rangle = (|00\ldots00\rangle + |11\ldots11\rangle)/\sqrt{2}$. With the possibility of superposition and entangled states, quantum computing offers a paradigm shift in computing and starts to be impossible to replicate on classical hardware when the number of qubits involved is sufficiently large.

Despite their simplicity, Eqs. (1.1) and (1.2) can be used to illustrate many of the challenges faced when trying to implement these fundamental concepts of quantum computing in practice. First of all, the individual qubits should be able to store their quantum state, Eq. (1.1), for as long as possible without suffering from decoherence. Moreover, high-fidelity techniques are required to initialize the state of the qubit, manipulate it with gates (similar to logic gates in classical computing) and measure the final state of interest. Finally, the number of qubits should be scaled up sufficiently to profit from the exponentially growing computational space indicated by Eq. (1.2). Scaling up the size of the register is particularly difficult as the performance of and control over individual qubits must be maintained while allowing to couple (and, therefore, entangle) different qubits. The challenge of implementing scalable quantum computing hardware has already been discussed and formalized more than 20 years ago in the DiVincenzo criteria [28].

> ❝*While they are typically among the first concepts in quantum computing to learn about, one can appreciate the relevance of DiVincenzo's criteria even more after a few years working in the field.*❞

The difficulty of scaling up and connecting many qubits while maintaining their individual performance makes evident that building quantum computation hardware implies to find a compromise in fulfilling the different requirements. For this reason, a variety of innovative approaches are pursued to implement reliable and scalable quantum computing hardware, for example based on trapped ions [29, 30], optics [31, 32], superconducting [19, 21] or semiconducting electronics [33, 34], and magnetic molecules [35–37]. Interestingly, many of DiVincenco's criteria can be fulfilled individually in each of the different approaches. For example, superconducting qubits are amongst the most promising platforms for quantum computing because they are typically well-controlled, macroscopic circuits with gate and readout fidelities approaching the thresholds for quantum error correction [38–42]. However, as macroscopic solid-state objects, they can suffer more easily from various sources of decoherence than atomic-scale systems, which are typically well isolated [43].

Beyond optimizing individual quantum hardware platforms, a promising avenue is the development of hybrid implementations that combine different types of quantum information hardware in order to exploit their unique strengths while mitigating their respective weaknesses. In this way, the compromise of balancing different requirements can be distributed across the subsystems instead of sacrificing advantages of one of the systems. Examples of

hybrid quantum systems include semiconductor quantum dots coupled to superconducting circuits [44] and nanomechanical resonators coupled to nitrogen-vacancy centers [45] or superconducting qubits [46]. In particular, hybrid architectures involving spin-based qubits and superconducting circuits have gained increasing research interest [37, 47–50]. The main idea behind this approach is to combine the long-coherence time offered by single spins, for example in magnetic molecules, with the fast and well-controlled readout and manipulation available with superconducting hardware. Naturally, there are two caveats inherent to the idea of coupling spins and superconducting circuits: the superconductor should be compatible with magnetic fields required to control the spin constituent and one has to bridge the gap from the macroscopic circuit to the nanoscopic scale on which individual spins operate.

> *"The motivation to build a hybrid architecture is based on the hope that the combined advantages of the two constituents outweigh the combined disadvantages."*

The first main result of this manuscript is the implementation of a circuit with the potential to address both of these concerns, a granular aluminum nano-junction fluxonium qubit which we nickname *gralmonium* [1]. By fabricating the full circuit from a single layer of the high kinetic inductance supercondutor granular aluminum (grAl), the gralmonium is designed to utilize the magnetic field resilience inherent to grAl for a fluxonium qubit. Moreover, the tunnel junction of the fluxonium is replaced by a lithographically defined volume of grAl on the order of $(20\,\text{nm})^3$, the *grAl nano-junction*, which besides implementing a field-resilient nonlinearity also offers an increased local sensitivity to the junction and its vicinity. Remarkably, both the spectrum and coherence of the gralmonium are measured to be comparable with conventional fluxonium qubits. However, frequency fluctuations in the gralmonium spectrum imply the presence of unexpected fluctuations of the grAl nano-junction parameters, indeed indicating a high susceptibility of the circuit to the small grAl volume.

Prompted by the surprisingly standard current-phase relation (CφR) extracted for the grAl nano-junction, the second main result of the thesis is the observation of Josephson harmonics in standard Al-AlO$_x$-Al tunnel junctions [2]. This result is based on measurements on various transmon devices from different laboratories. Contrary to the common expectation of a purely sinusoidal CφR, both a mesosocopic model of tunneling through an inhomogeneous AlO$_x$ barrier and the measured transmon spectroscopy reveal higher harmonic contributions on the percent level. As a consequence of Josephson harmonics, the transmon charge dispersion can significantly deviate from the expectation based on standard transmon modeling, which considers only a sinusoidal CφR. The applicability of these results to other superconducting circuits involving tunnel JJ evidences the relevance of Josephson harmonics to refine the understanding for superconducting circuit models and experiments.

This manuscript is delivered in two parts. The first part presents the main results of the thesis and the second part includes more detailed information similar to the supplementary

material of the corresponding publications. The main part is structured as follows: After the remaining introductory sections, Chapter 2 presents the most relevant features and measurements of the gralmonium qubit. Chapter 3 gives context for interpreting the nano-junction current-phase relation by discussing Josephson harmonics in conventional tunnel Josephson junctions. The main part is concluded in Chapter 4, which also gives perspectives on the implications of the results and relevant follow-up research. The second part of the manuscript covers in particular the experimental setup and sample holder (Appendix A), fabrication and additional measurements of the gralmonium circuit (Appendix B) and details on Josephson harmonics (Appendix C).

1.2 Superconducting Quantum Circuits

Superconducting circuits are amongst the most promising platforms for implementing quantum information hardware, and the largest quantum processors to date have been realized with superconducting circuits. Fundamentally, the approach is based on the lossless flow of current in superconductors, which enables the storage and manipulation of, in principle, long-lived electromagnetic excitations in resonant circuits. Probably the most intriguing feature of superconducting circuits is that a quantum state — typically associated with atomic-scale particles — can be hosted by macroscopic objects on the scale of hundreds of micrometers and involving many thousands of atoms.

As a consequence, superconducting circuits can be designed and fabricated using established methods such as finite element electromagnetic simulations and thin film lithography. Similar to classical electrical engineering, the basic building blocks of superconducting circuits are capacitors and inductors, which can be assembled to circuits with tailored purpose. Combined with the aforementioned design and fabrication techniques, this approach to quantum information hardware offers a high level of control for implementing the quantum system of interest.

> *"I will probably never stop being amazed*
> *about the idea that we can lay out some metal*
> *wires on a chip, cool them down and they start*
> *to behave as a quantum object."*

The transition from classical to quantum is formalized in the framework of *circuit quantization*, a set of rules to systematically derive the quantum Hamiltonian of a circuit from its lumped element representation [51, 52]. Per the correspondence principle and equivalent to the role of position and momentum in quantum mechanics, the flux Φ in inductors and charge Q on capacitor pads are promoted to conjugate variables for quantum circuits,

$$[Q, \Phi] = i\hbar \quad \Leftrightarrow \quad [n, \varphi] = i. \tag{1.3}$$

In the right hand side version of the commutator we have introduced two dimensionless operators, the number of Cooper pairs $n = Q/2e$ and the superconducting phase $\varphi =$

$2\pi\Phi/\Phi_0$, with h being Planck's constant, e the charge of an electron and $\Phi_0 = h/2e$ the superconducting magnetic flux quantum. As an example, using the formalism of circuit quantization, the Hamiltonian of the quantum LC circuit can be quantized as

$$H = \frac{Q^2}{2C} + \frac{\Phi^2}{2L} = \hbar\omega_{\mathrm{r}}\left(a^\dagger a + \frac{1}{2}\right),$$

(1.4)

in which a ($a^\dagger$) are the bosonic creation (annihilation) operators of the harmonic oscillator and $\omega_{\mathrm{r}} = 1/\sqrt{LC}$ is the resonant frequency.

1.2.1 Josephson Effect

In order to implement superconducting circuits which can be used to store and manipulate non-classical states, it is essential to have a nonlinear circuit element at hand, in addition to the linear capacitive and inductive building blocks. For this reason, the Josephson effect plays a fundamental role in superconducting circuits as it provides a lossless source for a nonlinear relation between the current through and the superconducting phase across a circuit element. Josephson predicted that the supercurrent through two superconducting electrodes separated by a thin insulator should be given by [53–55]

$$I(\varphi) = I_{\mathrm{c}} \sin\varphi$$

(1.5)

in which I_{c} is the maximum (critical) supercurrent sustained by the junction. The importance of the Josephson effect can be compared to the relevance of diodes in classical electrical engineering, which enable the implementation of digital hardware due to their nonlinear current-voltage relation.

Since Josephson's prediction, many types of so-called "weak links" have been studied with generally more complicated current-phase relations [56]. While, so far, tunnel Josephson junctions (JJs) have been considered to be sufficiently well described by the purely sinusoidal Josephson CφR given in Eq. (1.5), we will discuss in detail the validity and limitations of this simplification in Chapter 3. For simplicity, in this introductory chapter we keep the treatment of the tunnel JJ on the level of the purely sinusoidal Josephson CφR.

The energy contribution of a Josephson tunnel JJ in a circuit is given by integrating the CφR, which yields the Josephson energy-phase relation (EφR),

$$E(\varphi) = -E_{\mathrm{J}} \cos\varphi.$$

(1.6)

Here, $E_{\mathrm{J}} = \Phi_0 I_{\mathrm{c}}/2\pi$ is denoted the Josephson energy of the junction which is linked to the critical current. Note that associating the superconducting phase operator with the position variable turns out practical as, in this case, the EφR Eq. (1.6) can be considered a nonlinear potential term for a "phase particle". Instead, if φ was associated with the momentum, one would have to deal with a "nonlinear mass". Despite this assignment of position and momentum variables, the nonlinearity of the JJ is a form of kinetic inductance

as it arises from the motion (here tunneling) of Cooper pairs across the barrier. The notion of the JJ implementing a nonlinear inductance becomes evident by expanding the cosine potential of Eq. (1.6). While the first order of the expansion would correspond to a perfectly linear inductance with associated quadratic potential, the higher orders become increasingly relevant for increasing ϕ.

1.2.2 Superconducting Quantum Bits

Based on the nonlinearity of the Josephson junction (JJ) as a circuit element, a variety of superconducting quantum bits have been developed. In general, the different approaches try to find the best compromise between the various characteristics relevant for implementing a qubit. In particular, each design comes with a different degree of sensitivity to the various noise and loss channels affecting the coherence times of the qubit. Moreover, the possibility to perform fast gates can be limited by the anharmonicity of the qubit, i.e. the difference in transition frequency between the first and second transition of the circuit. Eventually, also the simplicity of the circuit design and its fabrication are highly relevant to make academic or industrial research on devices accessible.

> "We tend to call these circuits qubits but we should be well aware that their higher level spectrum can matter."
>
> — A Supervisor

A typical approach to outline the developments in superconducting circuits would be to follow the history of superconducting qubits starting from the Cooper-pair box (CPB): one of the first implementations of a superconducting artificial atom with the JJ connected to a superconducting island [57–59]. In the following, we instead take a state-of-the-art perspective and introduce two of the currently most common types of superconducting qubits, which are based on fundamentally different ways to harness nonlinearity from the Josephson junction: the *transmon* and *fluxonium* qubit. For each qubit we make links to historical developments in the field and highlight the advantages of the respective design.

Transmon

As shown in Fig. 1.1a, the transmon is a superconducting circuit in which the JJ is shunted by a large capacitor such that the Josephson energy E_J is much larger than the charging energy $E_C = e^2/2C$ of the capacitor [60], in which e is the charge of an electron. The standard transmon Hamiltonian with a purely cosine energy-phase relation reads

$$H = 4E_C(n - n_g)^2 - E_J \cos\varphi, \tag{1.7}$$

in which n_g is the offset charge (in number of cooper pairs) on the capacitor plate, for example induced by electric fields or due to quasiparticles. The index of n_g refers to the
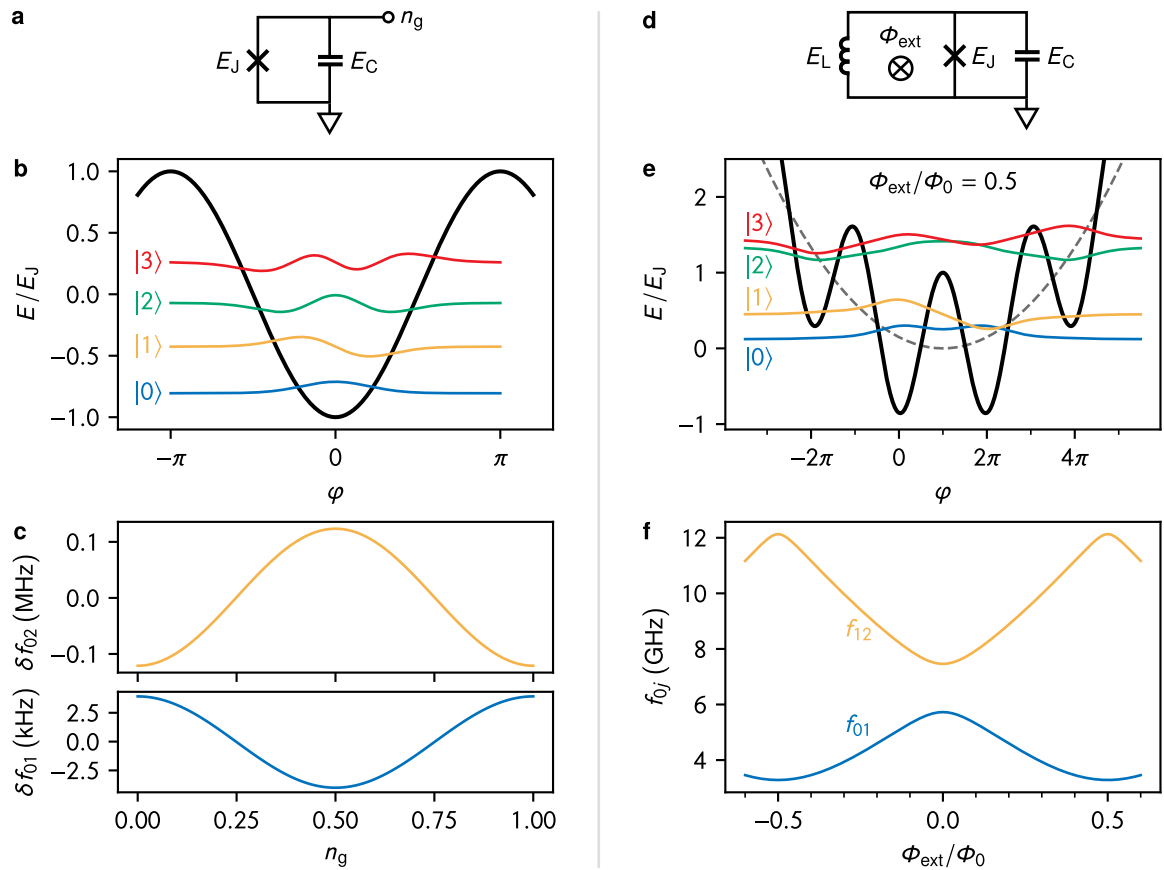
Figure 1.1: Two common superconducting qubits: transmon (left column) and fluxonium (right column). The rows show the lumped element circuit schematic, the energy landscape and wavefunctions, and the change of the spectrum with the respective external degree of freedom for the transmon (left column) and fluxonium qubit (right column). The first row (panels **a**,**d**) shows the lumped element circuit schematics with the relevant energy scales of the circuit elements: the Josephson energy E_J for the junction, the charging energy E_C of the capacitor and, for the fluxonium, the inductive energy E_L. The transmon features exponentially suppressed sensitivity to the offset charge n_g (cf. panel c) while for the fluxonium the external flux Φ_{ext} threading the loop between inductor and JJ is an important tuning parameter. **b**,**e** Potential energy landscape (black line) and first four wavefunctions offset by their eigenenergy. For the transmon, the plot resembles an anharmonic oscillator in a potential well defined by the JJ (cf. Eq. (1.7)). In contrast, the fluxonium physics at $\Phi_{ext}/\Phi_0 = 0.5$ (half flux bias) is dominated by tunneling between the potential wells (cf. Eq. (1.9)). The dashed gray parabola is the inductive energy contribution, which the Josephson potential oscillates around. The parameters used for the transmon are $E_J/h = 10\,\mathrm{GHz}$, $E_C/h = 0.2\,\mathrm{GHz}$ and for the fluxonium $E_J/h = 10\,\mathrm{GHz}$, $E_C/h = 10\,\mathrm{GHz}$ and $E_L = 0.3\,\mathrm{GHz}$. **c** Charge dispersion vs. offset charge n_g of the first two transmon levels. Note the orders of magnitude difference between the maximum charge dispersion of the first (bottom panel) and second transition (top panel). **f** Fluxonium spectrum vs. external flux Φ_{ext}. The potential and wavefunctions in panel e correspond to the spectrum at $\Phi_{ext}/\Phi_0 = 0.5$.

notion that, in principle, one can control the offset charge by applying a "gate" voltage to the capacitor.

In the transmon regime $E_J/E_C \geq 50 \gg 1$, the system dynamics correspond to the one of a phase particle with mass given by the capacitance C living in the potential well defined by the JJ (Fig. 1.1b). For this reason, the spectrum and wavefunctions are reminiscent of a quantum harmonic oscillator. However, in contrast to a harmonic system, the nonlinearity

of the Josephson potential leads to non-equidistant energy-levels with the fundamental transition frequency approximately given by [60]

$$hf_{01} \approx \sqrt{8E_J E_C} - E_C \, , \tag{1.8}$$

and an anharmonicity $\alpha/h = f_{12} - f_{01} \approx -E_C$, where h is Planck's constant. The main benefit of the transmon regime is the suppression of the charge dispersion $\delta f_{0j} = f_{0j}(n_g) - f_{0j}(0)$ of the energy levels j (cf. Fig. 1.1c), which scales exponentially with the ratio $-\sqrt{8E_J/E_C}$. In contrast, for the CPB in the opposite regime of $E_J/E_C \sim 1$, the offset charge has to be stabilized at values for which the spectrum is first-order charge insensitive in order to maximize the coherence, which is challenging in practice [59, 61, 62]. Note that while the transmon regime, in principle, promises to be exponentially insensitive to charge noise, it is still an important design consideration to ensure that the charge dispersion does not limit the dephasing time and the anharmonicity is not lowered more than necessary [60].

Since its initial publication more than 15 years ago, the transmon has been in the focus of research both in academia and industry leading to some of the largest quantum processors to date [19, 21, 63, 64]. This success is largely due to the simplicity and robustness of the circuit design and fabrication compared to other types of superconducting qubits. Moreover, coherence times of transmons on the order of several $100\,\mu s$ have been achieved [65, 66] by lowering the dielectric losses in the capacitor interfaces, which are currently one of the main limitations for more coherent devices [43, 66].

Fluxonium

In a fluxonium qubit, the JJ and capacitor across the junction are in parallel with a so-called superinductance, forming a superconducting loop interrupted by the JJ (cf. Fig. 1.1c) [67]. The name superinductance refers to the regime in which the characteristic impedance of the inductance exceeds the superconducting resistance quantum $R_q = h/(2e)^2$. Accordingly, the standard fluxonium Hamiltonian with a purely cosine energy-phase relation reads

$$H = 4E_C n^2 + \frac{1}{2}E_L \left(\varphi - 2\pi \frac{\Phi_{ext}}{\Phi_0}\right)^2 - E_J \cos\varphi \, , \tag{1.9}$$

in which $\Phi_0 = h/2e$ is the superconducting magnetic flux quantum, $E_L = (\Phi_0/2\pi)^2/L_q$ the inductive energy and Φ_{ext} the external flux through the fluxonium loop. Depending on the external flux bias (and the energy scales E_J, E_c, E_L) the fluxonium circuit can be continuously tuned from predominently one relevant potential well (around $\Phi_{ext} = 0$) to a system dominated by tunneling between two symmetric potential wells (at $\Phi_{ext} = 0.5\Phi_0$). In the latter case, shown in Fig. 1.1e, the frequency of the first transition at half flux bias is approximately given by the phase slip rate [68].

$$f_{01}(\Phi_{ext} = 0.5\Phi_0) = \frac{4}{\sqrt{\pi}}\left(8E_J^3 E_C\right)^{1/4} e^{-\sqrt{8E_J/E_C}} \, , \tag{1.10}$$

which shows that the transition is exponentially sensitive in $\sqrt{8E_J/E_C}$. The result is intuitive considering that E_J corresponds to the height of the tunnel barrier and E_C to

the inverse mass of the phase particle in the double-well potential. Consequently, the fluxonium half-flux frequency depends strongly on the ratio of the energy scales while for the transmon, the transition frequency depends on their product, and, thus, their absolute values (cf. Eq. (1.8)).

Compared to the transmon qubit, the fluxonium features a much larger anharmonicity (cf. Fig. 1.1e,f) which is a prerequisite to implement fast and high-fidelity gates [69, 70]. Moreover, using a superinductor to shunt the junction results both in insensitivity to charge noise as well as reduced sensitivity to flux noise compared to early implementations of flux based qubits [67, 71–73]. However, the challenges associated with implementing the superinductor increase fabrication complexity. Over the last decade, different solutions have been established to realize superinductors in practice. The historically first implementation is based on JJ arrays, in which multiple JJs with $E_J/E_C \gg 1$ are connected in series to implement a sufficiently large and linear inductance [67, 74]. Alternatively, high-kinetic inductance superconductors can be used, for example NbTiN [75], $Ti_xAl_{1-x}N$ [76, 77] or granular aluminum [78]. Finally, contrary to popular belief [67, 79], it has recently been shown that superinductors can also be implemented based on the geometric inductance of pure aluminum with sophisticated engineering of the wire layout [80, 81].

Interestingly, after primarily being in the spotlight of academic research, fluxonium qubits are actively considered as a promising qubit platform for upcoming generations of industrial superconducting quantum processors [70, 82]. In terms of coherence, the longest documented coherence time of a superconducting qubit $T_2^* \approx 1.5\,\text{ms}$ to date has been recently demonstrated in a fluxonium qubit [74]. We note that, in order to reach this value, the device has been decoupled from the readout mode — an example of the trade-off between different desired qubit properties mentioned in the introduction. Similar to the transmon and other superconducting circuits, an analysis of the decoherence budget reveals that improvements in sample fabrication and materials used are key factors to further improve the performance of fluxonium devices [70, 74, 77].

1.2.3 Circuit Quantum Electrodynamics (cQED)

On top of the coherence of and control over a qubit's state, the ability to perform a high-fidelity measurement of the state is crucial. Inspired by the Nobel-Prize-winning field of cavity quantum electrodynamics, which treats the interaction of atoms and other particles with photons as the quanta of light [83], the framework of *circuit quantum electrodynamics* (cQED) explores the coupling of superconducting artificial atoms to bosonic readout modes. Since the seminal papers [84, 85], the cQED architecture has been established as a standard technique for the readout of superconducting qubits.

Of particular relevance is the dispersive readout regime in which a two-level system with transition frequency ω_q and the readout ("cavity") mode at ω_r are weakly coupled with a coupling rate g such that g is much smaller than the frequencies ω_q, ω_r as well as the detuning $\Delta = \omega_q - \omega_r$. In this case, the qubit, readout and their interaction

can be described by a rotating-wave approximation ($g \ll \omega_q, \omega_r$) and an approximately diagonalized ($g/\Delta \ll 1$) form of the Jaynes-Cummings-Hamiltonian,

$$H/\hbar \approx \frac{1}{2} \left(\omega_q + \chi \right) \sigma_z + \left(\omega_r a^\dagger a + \chi \sigma_z \right) a^\dagger a \,. \tag{1.11}$$

Due to the last term in Eq. (1.11), the readout mode acquires a dispersive shift of $\chi = g^2/\Delta$ depending on the qubit state. In this approximation, the readout is quantum non-demolition (QND), which implies that the state of the qubit is preserved after its projection.

> "*The T_2^* is not only a matter of the qubit itself but also about the quality of your readout.*"
>
> — A Supervisor

The success of the dispersive readout scheme, often combined with near quantum-limited amplification and Purcell filters, is evident in the realization of single-shot readout for superconducting qubits with fidelities on the level of 99 % and beyond on timescales of ~ 100 ns [9, 10, 86–90]. However, understanding the nature of non-QND effects in measurements of superconducting qubits becomes increasingly relevant. A variety of possible explanations have been discussed over the last decade, as these deviations from QND readout can be visible at much lower readout powers than expected [91–94]. For this reason, it is important to be aware of the limitations for the approximations going into Eq. (1.11). Particularly, the assumption of an ideal two-level system is not realistic given the finite anharmonicity and presence of the higher level spectrum in superconducting circuits, especially in weakly anharmonic transmons. Moreover, non-perturbative terms which are ignored in the rotating wave approximation can become relevant [95–97].

1.3 Spin-cQED Hybrid Architectures

As we have seen in the previous sections, superconducting circuits excel as a platform for quantum information due to established techniques to manipulate and readout the quantum state with high fidelity on sub-microsecond timescales, enabled by engineering circuit elements and their interactions. In contrast, the weakness of superconducting hardware as mesoscopic objects is their sensitivity to the plethora of uncontrolled degrees of freedom present in solid-state physics.

Pretty much the opposite challenges compared to superconducting circuits emerge when using the spin of electrons, magnetic atoms or molecular magnets to store and manipulate quantum information. As atomic-scale objects, they are typically well-isolated from the environment with coherence times reaching seconds or even hours in the case of nuclear spins [98, 99]. However, for the same reason, it is challenging to increase the coupling to the spin degree of freedom sufficiently to address and read out the spin. To overcome this challenge, a variety of readout schemes have been developed based on transport measurements including molecular spin-transistors [100], carbon-nanotube quantum dots [101] or scanning-probe techniques [102].

What these approaches have in common is that they bridge the gap between the nanoscopic scale of single spin systems and macroscopic objects. In this regard, superconducting circuits are a promising constituent for hybrid quantum systems, owing to their flexibility in tailoring electromagnetic couplings. Indeed, coupling superconducting resonators or qubits to spins based on electron-spin-resonance (ESR) has been an active area of research for more than a decade [103–106]. By confining the mode volume of the magnetic field of a resonant circuit, the coupling can be enhanced to be sensitive to an ensemble of few spins [47]. These efforts have culminated in the recent success of the readout of single spins by using a superconducting single-photon detector in the readout chain [49, 50].

In this thesis, we work towards an alternative approach for a hybrid spin-cQED architecture based on the kinetic inductance of superconductors, which arises due to the inertia of cooper pairs to alternating current. In contrast to geometric inductance, no magnetic field is associated with current flowing through a kinetic inductance. As a consequence, coupling via the kinetic inductance could be used to implement longitudinal readout schemes instead of transverse ESR-type coupling [107, 108]. Similar to the approaches discussed above, the goal is to implement a magnetic field-resilient circuit which is locally sensitive to the magnetic field of few or ultimately single spins.

1.4 Granular Aluminum Circuits in Magnetic Field

The goal of spin-cQED hybrid applications imposes a significant design constraint on the superconducting circuit: it should be resilient to magnetic fields relevant for operating the spin constituent, which are typically in the 100 mT range. For example, using aluminum — a well-established material for low-loss superconducting circuits [43] — for hybrid applications is challenging due to its low critical field $B_c = 10$ mT. In principle, it is possible to increase the in-plane field-resilience by reducing the film thickness to values on the order of 10 nm. However, the versatility of nonlinear devices based on standard mesoscopic Josephson junctions with dimensions in the $(100 \text{ nm})^2$ range is limited due to a Fraunhofer-pattern suppression of the critical current [109, 110]. In contrast, working towards a kinetic inductance based circuit puts disordered superconductors such as NbN [111–114], NbTiN [75, 115, 116], TiN [117–119] or InO [120] in the focus.

In this work, the material of choice is superconducting granular aluminum (grAl), which is composed of crystalline aluminum grains, 2–4 nm in diameter, separated by an amorphous aluminum oxide (AlO_x) matrix [121, 122]. As a consequence, compared to pure aluminum, grAl features an enhanced critical temperature on the order of $T_c \approx 2$ K with a dome-like dependence on the sheet resistivity [123] as well as a substantially increased kinetic inductance reaching up to nH/□ at a film thickness of 20 nm [124, 125]. Moreover, the material can be fabricated with standard evaporation techniques by adding an oxygen atmosphere while evaporating aluminum. Importantly, grAl has been established as a low-loss material for superconducting circuits [124–126] and has already been used, among others purposes, for implementing the superinductance of flux-based qubits [78, 127], and even the nonlinear inductance of a transmon qubit [5].

Although a critical magnetic field of several Tesla can be expected for granular aluminum based on DC measurements [128, 129], it is essential to confirm that grAl remains a low-loss material for microwave circuits in magnetic fields. In addition, the situation for thin film geometries used in superconducting circuits can be different from the intuition for bulk superconductivity. In general, for a superconductor subject to magnetic field, two main effects are relevant: (i) the suppression of the superconducting gap and (ii) screening currents trying to shield the field. Both mechanisms influence the kinetic inductance of a superconductor like grAl. The first effect is relevant because the kinetic inductance is directly related to the superconducting gap and the suppression thereof. The second contribution arises from the screening currents already taking up part of the critical current. In this way, the inductance is increased similar to the nonlinearity of the Josephson inductance.

> "*A thin film grAl resonator goes to the therapist. "I'm such a disordered mess, my inner self is never free. Am I even a superconductor if I cannot shield myself?", it complains. "No worries," says the therapist, "don't compare yourself to others so much. You only have to shield yourself…a little bit."*"

Due to the geometry of thin-film grAl circuits with thickness in the tens of nanometer, the two mechanisms are relevant to different degree depending on the orientation of the applied magnetic field with respect to the plane of the film. In the following, we discuss the two effects and their influence on grAl circuits in more detail using the frequency dependence and internal loss measurements of grAl stripline resonators similar to the ones in Ref. [4]. All measurements shown are taken on samples fabricated with a sheet indutance on the order of $2\,\text{nH}/\square$, for which the remaining contribution of the geometric inductance can be considered irrelevant [130]. The samples are measured in a cylindrical copper sample holder (see Appendix A for more details) and cooled down in a Sionludi dilution cryostat equipped with a compact 3D vector magnet.

Resilience to In-Plane Magnetic Field

In Fig. 1.2 we show measurements for the magnetic field being applied parallel to the plane of the thin-film (i.e. substrate surface). In this case the screening currents are minimal and the dominant effect is the suppression of the gap. Based on Mattis-Bardeen theory, for $T \ll T_\text{c}$, the kinetic inductance L_k is inversely proportional to the superconducting gap Δ [131, 132] and using the field-dependence of the gap, $\Delta(B_\parallel) = \sqrt{1 - (B_\parallel/B_\text{c})^2}$ with critical field B_c, the relative frequency change of a resonator for $B \ll B_\text{c}$ can be approximated by

$$\frac{\Delta f_\text{r}(B_\parallel)}{f_\text{r}(0)} = \frac{f_\text{r}(B_\parallel) - f_\text{r}(0)}{f_\text{r}(0)} \approx -\frac{1}{2}\frac{L_\text{kin}(B_\parallel)}{L_\text{kin}(0)} \approx -\frac{1}{4}\left(\frac{B_\parallel}{B_\text{c}}\right)^2 , \qquad (1.12)$$

where $f_\text{r}(0)$ and $L_\text{kin}(0)$ are the resonant frequency and kinetic inductance in zero magnetic field, respectively. While the resulting parabolic frequency shift corresponds to B_c in the
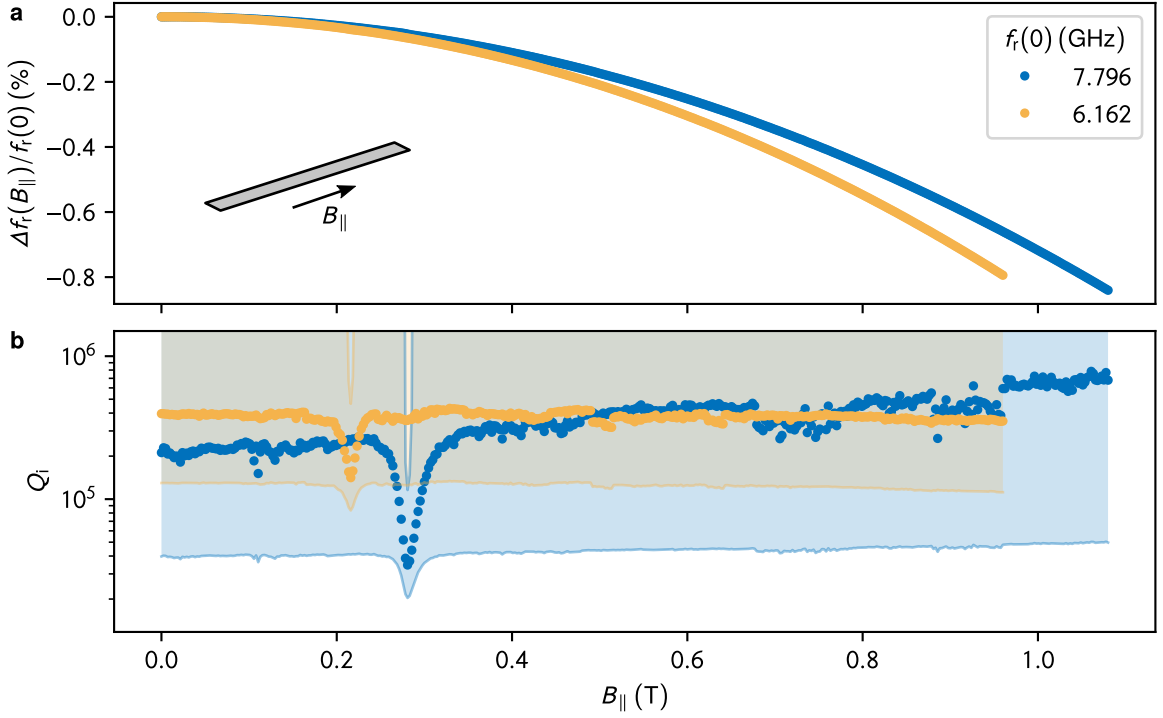
Figure 1.2: Resilience of grAl resonators up to 1 T. **a** $\Delta f_r/f_r$ in magnetic field $B_\parallel$ applied in-plane to the thin film (cf. sketch) for two stripline grAl resonators with resonatn frequencies at zero field $f_r(0)$ as indicated in the legend. The dependence is parabolic as expected from Eq. (1.12). **b** Internal quality factor Q_i for the same field range as shown in panel a. The markers correspond to Q_i and the shaded areas to the systematic Fano uncertainty range introduced in Ref. [3] and calculated for an isolation of -15 dB. Note the pronounced dip in Q_i at $B_\parallel = 0.22$ T and 0.28 T for the lower and higher frequency resonator, respectively.

range of several Tesla (cf. Fig. 1.2a), it should be mentioned that these values extracted based on the approximation Eq. (1.12) have limited significance. We note that for each $B_\parallel$, the out-of-plane field $B_\perp$ has been tuned such that f_r is maximal in order to compensate for misalignment of $B_\parallel$ with the plane of the film.

Importantly, as we show in Fig. 1.2b, the internal losses of grAl resonators are resilient to parallel magnetic field up to at least 1 T and stay on the level of $Q_i \approx 10^5$ measured in zero field [124, 125]. We note that this type of frequency-dependent measurement can be subject to a systematic source of error due to Fano-type interference [3]. Interestingly, a pronounced decrease in Q_i occurs at magnetic fields $B_\parallel$ corresponding to the fields where the Zeemann energy splitting of spins 1/2 with Landé factor $g = 2$ are resonant with the respective f_r, i.e. $hf_r = g\mu_B B_\parallel$. While similar features have been observed in other superconductors or different substrates and are commonly attributed to paramagnetic impurities of the substrate or interfaces [115, 116, 133, 134], the precise origin of this spin ensemble in grAl remains unknown. Among possible candidates are oxygen adsorbates [135, 136], trapped quasiparticles [137] and, in particular for grAl, spins localized in the oxide between the aluminum grains [138].
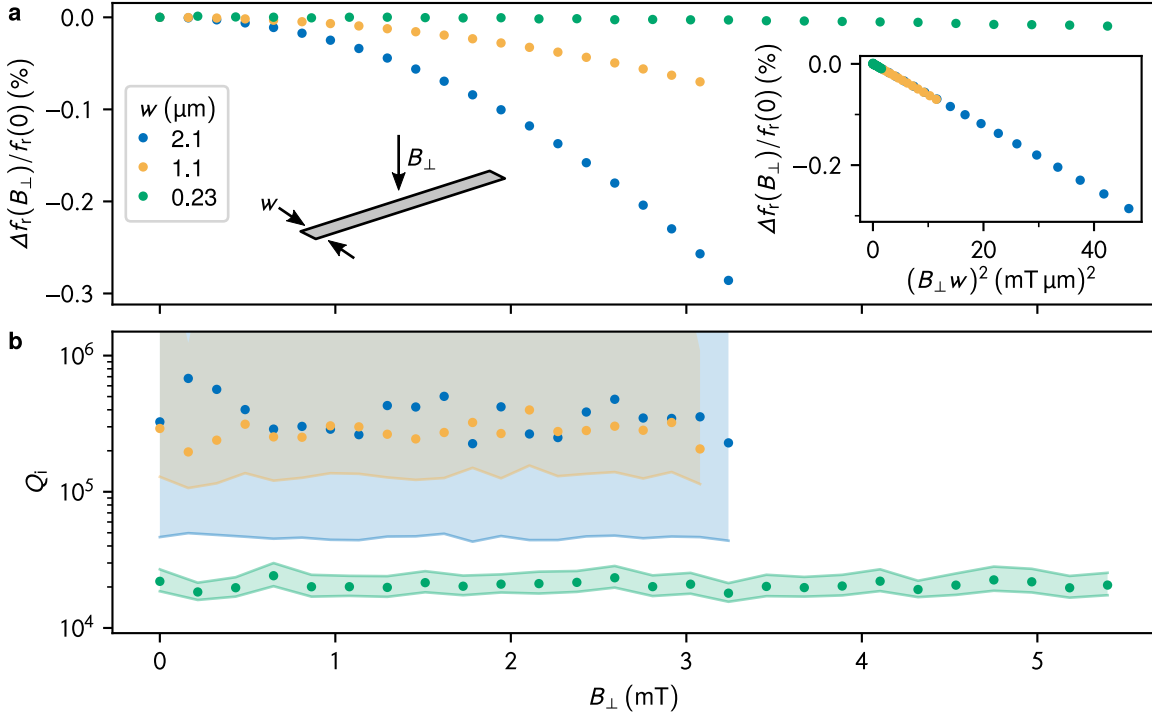
Figure 1.3: Sensitivity of grAl resonators to out-of-plane field. **a** Relative frequency shift $\Delta f_\mathrm{r}/f_\mathrm{r}$ in magnetic field $B_\perp$ applied perpendicular to the thin film (cf. sketch) for three stripline grAl resonators with different widths w as indicated in the legend. The parabolic dependency is weaker the narrower the width. The inset confirms the quadratic dependence on $B_\perp$ and w as expected from Eq. (1.13). **b** Internal quality factor Q_i for the same field range as shown in panel a. The markers correspond to Q_i and the shaded areas to the systematic Fano uncertainty range introduced in Ref. [3] and calculated for an isolation of $-15\,\mathrm{dB}$.

Out-of-plane Sensitivity

For magnetic field applied perpendicular to the plane of the film, the phenomenon causing the measured frequency shift is different. For typical resonator geometries, screening currents lead to the dominating change in kinetic inductance, and the contribution from the gap suppression is vanishing, as we will see in the following. The change in kinetic inductance due to screening currents is given by $L_\mathrm{k}(I)/L_\mathrm{k}(0) = \sqrt{1 + (I/I^*)^2}$, in which I^* is a parameter on the order of the critical current [112, 132, 139]. In order to get the dependence on perpendicular field, the relevant film property is the effective screening length $\lambda_\perp = \lambda_\mathrm{L}^2/t$, which enhances the London penetration depth λ_L when the film thickness $t \ll \lambda_\mathrm{L}$. For a grAl film with λ_L on the order of micrometers [121, 140] and thickness $t = 20\,\mathrm{nm}$, we get $\lambda_\perp \sim 50\,\mathrm{\mu m}$. As a consequence, for a stripline resonator with length $l \gg \lambda_\perp$ and width $w \ll \lambda_\perp$, the screening currents increase proportional to $B_\perp \cdot w$ [115, 141]. Since the critical current increases linearly in w, the relative frequency shift of the grAl resonator in small out-of-plane magnetic fields can be approximated by

$$\frac{\Delta f_\mathrm{r}(B_\perp)}{f_\mathrm{r}(0)} \approx -\frac{1}{2}\frac{L_\mathrm{kin}(B_\perp)}{L_\mathrm{kin}(0)} \propto -\left(\frac{I}{I^*}\right)^2 \propto -\left(B_\perp w\right)^2 . \tag{1.13}$$

This dependency is confirmed in Fig. 1.3a by measuring resonators with different widths made from the same grAl film. Note that the field range explored in the measurement is on the order of mT, about 3 orders of magnitude lower in comparison to in-plane field required for similar frequency shifts (cf. Fig. 1.2a).

As shown in Fig. 1.3b, the internal losses are also resilient to out-of-plane magnetic field in this range. However, this is true only in the regime below a geometry-dependent threshold field $B_{\perp,\text{th}}$, in which the internal losses remain on the order of the zero-field value and the frequency shift is given by Eq. (1.13). In contrast to this *reversible regime*, grAl resonators enter an *irreversible regime* above $B_{\perp,\text{th}}$, in which the frequency shift becomes hysteretic and Q_i shows stochastic jumps in value [4]. Moreover, in this regime crossings with field-dependent modes can be observed, which can be attributed to fluxons coupled to the microwave current of the resonator and tuned in frequency by the magnetic field. Typical values for $B_{\perp,\text{th}}$ are on the order of 1 mT for 10 μm-wide resonators [4] but can be increased to several mT by reducing the resonator width as shown in Fig. 1.3.

In summary, the intrinsic losses of grAl resonators are resilient to magnetic fields up to 1 T aligned in-plane to the film and, depending on the geometry of the circuit, resilient to order of mT magnetic fields out-of-plane to the film. Notably, also the nonlinearity inherent to the kinetic inductance of grAl has been shown to be resilient to in-plane magnetic field up to ~ 100 mT [5], as discussed in more detail in Section 2.1.2. The compromise of sufficient resilience to in-plane magnetic fields but a remaining sensitivity, which can be tuned by geometry, makes grAl a promising material choice for hybrid applications.

2 Gralmonium: Granular Aluminum Nano-Junction Fluxonium Qubit

In this chapter the first main result of the manuscript is presented: a single-layer granular aluminum (grAl) fluxonium qubit, nicknamed *gralmonium.* First, we discuss how grAl circuit elements can be designed to implement varying degrees of nonlinearity. Next, we outline how this work is related to the previous implementation of a transmon qubit with a grAl Josephson element. After introducing a grAl-based replacement for a tunnel junction, the *grAl nano-junction,* the circuit design and model for the gralmonium is discussed. Experimental results on the spectroscopy and time domain characterization of the gralmonium match all expectations for a conventional fluxonium, apart from conspicuous fluctuations in parameters related to the nano-junction. The chapter ends with the observation that the nano-junction current-phase relation is indistinguishable from the expectation for a standard tunnel junction. This chapter is adapted in parts from Rieger, Günzler et al., Nat. Mater. 22, 194–199, 2023 (Ref. [1]).

2.1 Design Considerations

2.1.1 Nonlinearity of Granular Aluminum Circuit Elements

As discussed in the introductory chapter, the goal of implementing a magnetic-field resilient circuit with the potential to detect the state of a few spins imposes two main design constraints. We have already seen in Section 1.4 that grAl circuit elements fulfill the first requirement which is to be compatible with magnetic fields on the order of $\sim 100\,\text{mT}$ relevant for the operation of spin-based qubits. The second constraint is the possibility to realize a circuit element which is sensitive to the spin state. The rapid decay of the magnetic dipole field with the cubed distance $1/r^3$ [142] suggests that such a detector element would need dimensions on the nanometer scale.

Consequently, in this section, we discuss the versatility offered by grAl to implement various circuit elements and focus on the dependence of their properties on film parameters and dimensions of the element. As illustrated in Fig. 2.1a, the microstructure of grAl, composed of crystalline aluminum grains in an amorphous aluminum-oxide matrix, corresponds to a 3D network of Josephson junctions. Note that the junctions in this
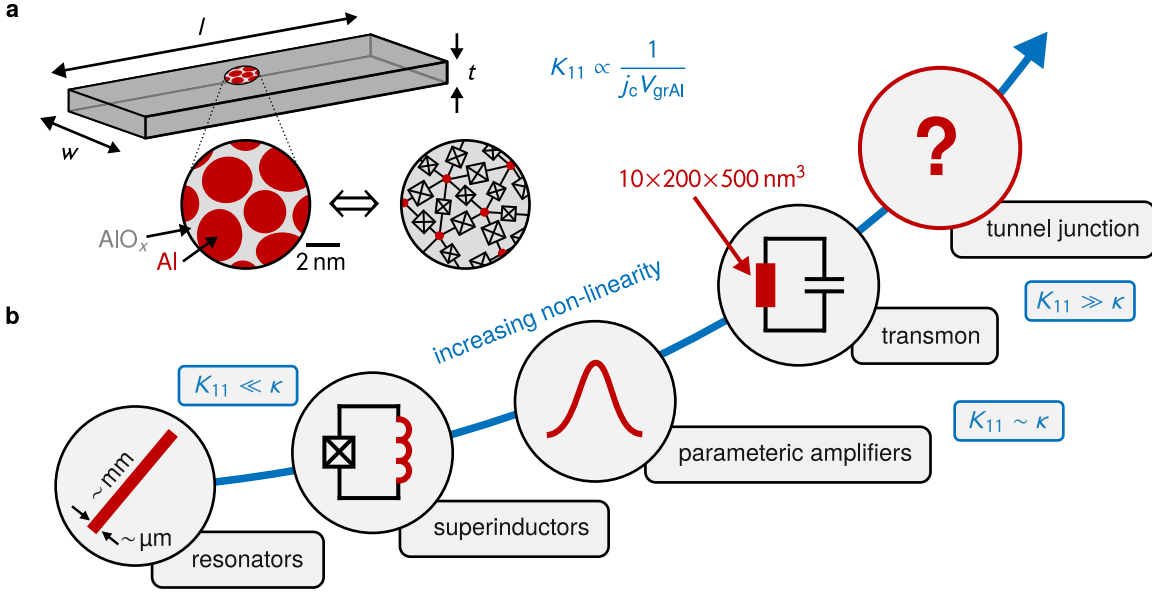
Figure 2.1: Nonlinearity of granular aluminum (grAl) circuit elements. **a** The microstructure of grAl, consisting of crystalline aluminum grains in an amorphous aluminum oxide matrix (sketched in the zoom-in), can be modeled as a 3D Josephson junction network. As a consequence the self-Kerr coefficient K_{11} of grAl circuit elements scales inversely proportional to the critical current density j_c of the film and the volume $V_{grAl} = lwt$ of the grAl element with length l, width w, and thickness t **b** The scale of nonlinearity which can be covered by grAl elements by tailoring their dimensions. While K_{11} can be designed much smaller than the linewidth κ, for example for resonators and superinductors, an elevated nonlinearity can be used for paramteric amplification. Expanding on the implementation of a transmon qubit with a grAl volume on the order of $(100\,\text{nm})^3$ as the nonlinear Josephson element, this thesis addresses the question if a tunnel junction can be replaced by a sufficiently small volume of grAl. Note that the scale is only qualitative on purpose as the notion of K_{11} and κ is not precisely defined when transitioning from full grAl resonators to increasingly smaller circuit components being made from grAl.

network do not necessarily coincide with the physical aluminum grains [138, 143]. Based on this intrinsic structure, the circuit quantum electrodynamics of a rectangular strip of grAl carrying a homogeneous current along one dimension, can be modeled as a 1D array of Josephson junction for frequencies well below the plasma frequency of the film [144]. The resulting self-Kerr coefficient of the grAl element is given by

$$K_{11} \propto \frac{\omega_1^2}{j_c V_{grAl}}, \tag{2.1}$$

in which ω_1 is the frequency of the fundamental mode, j_c is the critical current density of the film and V_{grAl} is the volume of the grAl element (cf. Fig. 2.1a). Note that j_c decreases with a power law inversely to the sheet resistivity of the grAl film [140, 145]. Remarkably, the predicted scaling of Eq. (2.1) has been confirmed experimentally across many orders of magnitude [144].

The key dependency of Eq. (2.1) for fabricating grAl circuit elements from a particular film is conceptualized in Fig. 2.1b: for fixed frequency ω_1 and critical current density j_c, the nonlinearity of a grAl circuit element increases inversely proportional to the volume of the element. As a consequence, the geometry of a grAl wire is a crucial tuning knob for tailoring

its nonlinearity. On the low nonlinearity side of the scale are grAl resonators [4, 125, 130] and grAl superinductors [78, 127] with typical dimensions on the order of $\sim \mu$m in width and 100s of μm in length. As required for these objects, their self-Kerr coefficient $K_{11} \sim$ Hz is sufficiently small such that the grAl volume implements a quasi-linear inductance. By increasing the nonlinearity, a grAl circuit element can be utilized to achieve parametric amplification [146] similar to Refs. [147–149].

> "*If we trust a model over several orders of magnitude, we might as well extrapolate it by one more.*"

Utilizing a grAl inductance with volume $10 \times 200 \times 500\,\text{nm}^3$, a transmon-type superconducting qubit has been implemented in Ref. [5] in which the self-Kerr $K_{11} \approx 4.5\,\text{MHz}$ exceeds the linewidth of the mode by two orders of magnitude. Building on this result and trying to implement an even smaller grAl circuit element, starts to test he limits of the model underyling Eq. (2.1), especially as the dimensions of the grAl volume approach the scale of only a few aluminum grains in the film. For this reason, this thesis addresses the question how far the versatility of nonlinear grAl circuit elements can be extended and if a sufficiently small grAl volume can effectively replace a conventional tunnel junction.

2.1.2 From GrAl Transmon to GrAl Fluxonium

The possibility to use order of $(100\,\text{nm})^3$ volumes of grAl as nonlinear Josephson elements, as explored in previous works in the group [5, 140], serve as valuable guidance. In particular, the $10 \times 200 \times 500\,\text{nm}^3$ nonlinear grAl inductance of the transmon qubit in Ref. [5] confirms that magnetic field resilience and low microwave losses are still given for a grAl circuit element which contains only a few thousand Al nano-grains. In this section, we briefly discuss the implications and limitations of the grAl transmon approach in order to motivate why a fluxonium-type circuit is suitable and necessary for utilizing even smaller nonlinear grAl elements.

A key design aspect for the grAl transmon is that the grAl volume serving as the Josephson element of the circuit must be shunted by a low-impedance capacitance in order not to dilute the nonlinearity with additional (linear) inductance. This requirement is realized in Ref. [5] by evaporating two additional layers of pure aluminum in a multi-angle fabrication. Although the shunting layers ensure that the circuit is in the qubit regime, i.e. the self-Kerr exceeds the linewidth $K_{11} \gg \kappa$ (cf. Section 2.1.1 and Fig. 2.1), the low anharmonicity of the circuit can limit the manipulation and readout timescales. While further decreasing the grAl volume would help to increase the nonlinearity, there are two practical challenges in scaling down the unshunted grAl element for this type of circuit design. First, it will be difficult to evaporate the two shunting layers in such close proximity to each other that a sub $(100\,\text{nm})^2$ area of grAl remains uncovered. Second, the grAl element can be easily short-circuited by electrostatic discharge when it is galvanically connected to ideally very low-impedance, large capacitance pads.

Establishing the perspective of grAl for hybrid applications beyond the resonator measurements discussed in the introductory Section 1.4, the grAl transmon has been shown to be resilient up to in-plane magnetic fields of $\sim 100\,\mathrm{mT}$. However, in this field range, the circuit starts to be limited by the pure alumnium shunting layers. Since the low-impedance capacitance is essential for the circuit design, the aluminum layers could be replaced by superconductors with higher critical field. Unfortunately, alternatives like niobium are more difficult to include in a multi-layer fabrication with granular aluminum, for example due to the risk of lossy niobium oxides [150] or finite contact resistance between the layers. Apart from that, the interface between high- and low-impedance layers will lead to locally increased current densities and can lead to interference effects in magnetic field[146].

In terms of readout, the transmon in Ref. [145] is measured in resonance fluorescence as it is directly coupled to a waveguide, which dominates the energy relaxation of the qubit. Further decoupling the circuit would increasingly impair a fast and high-fidelity readout. On the contrary, a cQED dispersive readout scheme with the transmon coupled to a dedicated readout mode would offer (approximately) quantum non-demolition readout (cf. Section 1.2.3). However, for a fixed-frequency transmon, the dispersive shift decreases quadratically with the frequency detuning between qubit and readout mode, which reduces the reliability of finding resonator-qubit pairs in a suitable coupling regime.

In total, while many aspects of the grAl transmon can be further improved, in the best case the resulting circuit would approach the properties of conventional cQED transmons. In contrast, a fluxonium-type of circuit offers a natural solution for many of the limitations discussed above. First of all, in the fluxonium the nonlinear circuit element is shunted by a high-impedance superinductor, which can be implemented with grAl [78, 127], avoids the need for an additional shunting layer and, thus, simplifies the fabrication process. Additionally, the superinductor comes with the practical advantage of protecting the small grAl volume from discharge by limiting the current. Moreover, dispersive readout can be implemented despite the high-impedance environment by sharing kinetic inductance with a readout resonator similar to Refs. [78, 151]. Finally, for the purpose of coupling spins to the circuit, the fluxonium transition frequency at half-flux bias would profit from an exponential sensitivity to the parameters of the grAl Josephson element (cf. Section 1.2.2).

Of course, opting for a fluxonium circuit operated in strong magnetic fields can also bear risks. One obvious caveat compared to a fixed frequency transmon could be the reliance and sensitivity of the fluxonium to out-of-plane flux (cf. Section 1.2.2). On the other hand, this degree of freedom can also be a powerful tool, e.g. to analyze the qubit at different frequencies and to select coupled qubit-resonator pairs directly based on flux sweeps. The latter idea is based on how the frequency extrema of the first fluxonium transition are related to its circuit parameters: while the zero-flux frequency can be bounded by the fluxonium inductance and capacitance, the half-flux frequency is most sensitive to the Josephson energy. Lastly, by using high-resistivity grAl the length of the required superinductor and, consequently, the loop area relevant for the out-of-plane sensitivity can be scaled down compared to previous grAl-superinductor fluxoniums [125]. The remaining design question is if it is feasible to implement a grAl volume small enough to operate in the phase-slip regime required for a fluxonium tunnel junction.

2.2 GrAl Nano-Junction

As outlined in the previous sections, in order to implement a fluxonium tunnel junction using a small volume of grAl, the suitable approach is to utilize a high-resistivity grAl film and aim to minimize the dimensions of the grAl element. With this strategy in mind, what are realistic dimensions that should be aimed for and which level of nonlinearity would we expect for such an element? In the following, we estimate an answer to these questions by extrapolating the values documented in Ref. [140].

Given a measured critical current on the order of $I_c \sim 1\,\mu A$ for a grAl element with sheet resistivity in the range $\rho \approx 3000\text{--}6000\,\mu\Omega\,cm$ and cross-section $\sim 20{\times}200\,nm^2$, we find that with a reduction in width by one order of magnitude, one could implement a grAl element with critical current $I_c \lesssim 100\,nA$ corresponding to a Josephson energy of $E_J/h \lesssim 100\,GHz$. Indeed, this would be the relevant order of magnitude for which the junction is placed in the phase-slip regime $E_J \sim E_C$ (cf. Eq. (1.10)), provided that the capacitance across the junction is small. As we expect $C \ll 1\,fF$ (corresponding to $E_C \gtrsim 20\,GHz$) for electrodes with the mentioned dimensions, the regime required to implement a tunnel junction appears to be within reach.

> "*The size of the grAl volume for replacing a fluxonium tunnel junction creates an interesting high-risk high-reward synergy: the fluxonium will only work if the junction is small enough but we will only know that the junction is small enough if we can measure a fluxonium.*"

Based on this estimation, it is clear that one has to lithographically define a volume ε^3 of grAl with dimensions on the order of $\varepsilon \approx 20\,nm$. In the following, we denote this grAl element the *grAl nano-junction*. Owing to its small dimensions, this circuit element is not only testing the limits of modeling the grAl microstructure (cf. Section 2.1.1) but also the limits of reliable thin film lithography. In principle, the feature size can still be directly written with high-resolution e-beam lithography, for example by a combination of using conductive substrate like silicon, thin photo resist layers or an etching-based fabrication approach. However, on insulating sapphire — an established low-loss substrate for superconducting circuits thanks to its simplicity in handling and preprocessing — proximity effects considerably influence the exposure and impair e-beam lithography on the $\sim 10\,nm$ scale.

Fig. 2.2 summarizes the approach developed to fabricate grAl nano-junctions with adequate reproducibility based on lift-off lithography on sapphire substrate. As shown in Fig. 2.2a, in order to fine-tune the width of the junction, the diagonal distance of two wires separated by a few tens of nm is adjusted (green arrows) to maximize the yield of junctions which are connected. Example scanning electron microscope (SEM) images of a $\varepsilon \approx 20\,nm$ wide nano-junction (left panel) and a disconnected version (right panel) are shown in Fig. 2.2b. After optimizing the diagonal distance and the exposure parameters, a significant fraction
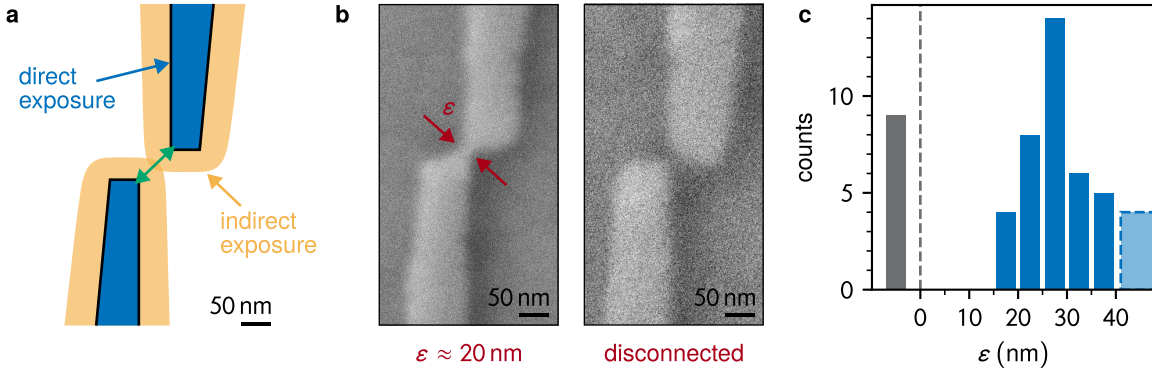
Figure 2.2: Fabrication of the grAl nano-junction. **a** Sketch of lithography pattern to fabricate the nano-junction. The geometry directly written with an electron beam and the area effectively exposed due to proximity effects are shown in blue and yellow, respectively. As indicated by the green arrows, the overlap leading to the nano-junction can be tuned by adjusting the diagonal distance between the corners of the leads (green arrow). **b** Scanning electron microscope (SEM) images of a connected nano-junction (left panel) and an disconnected version (right panel). The width of the nano-junction $\varepsilon \approx 20$ nm is indicated by the red arrows. **c** Histogram of measured nano-junction widths ε based on 50 SEM images similar to the ones shown in panel b. The gray bar at $\varepsilon < 0$ shows the number of interrupted junctions, and the rightmost bar with dashed outline includes all widths $\varepsilon \geq 40$ nm.

of the nano-junctions in a fabrication run are in the target range for the width, as illustrated by the histogram of measured widths for 50 nano-junctions in Fig. 2.2c.

2.3 Gralmonium Qubit

2.3.1 Circuit Design

Equipped with the preliminary considerations of the previous sections, here, we discuss how the grAl nano-junction is embedded into a single-layer grAl fluxonium circuit, which we nickname gralmonium. As shown in Fig. 2.3, the gralmonium circuit including its readout antenna covers the whole scale of nonlinearity from resonator to nano-junction sketched in Fig. 2.1. The sample is patterned from a single layer of grAl with thickness 20 nm and sheet resistance 1.5 kΩ/$\square$ on a sapphire substrate (cf. Appendix B.1). The readout antenna (Fig. 2.3a) is formed by a 4 µm × 700 µm stripline of grAl, for which we expect a low nonlinearity on the order of a self-Kerr coefficient $K_{11} \sim 10$ Hz [4, 144]. The gralmonium qubit is galvanically coupled to the readout by sharing 8 µm of the antenna as part of the fluxonium loop (Fig. 2.3b), similar to Refs. [78, 151]. The superinductor is given by a 170 nm wide and approximately 50 µm long grAl wire. In order to reduce the sensitivity to out-of-plane magnetic field, the loop area is decreased compared to a rectangular shape by arranging the wire in a meander pattern.

The wire of the flux loop is locally confined to a width of $\varepsilon = 20$ nm (Fig. 2.3c), implementing the ε^3 volume of the grAl nano-junction (cf. Section 2.2). Given the ≈ 4 nm grain size in grAl [122] and the superconducting coherence length of our grAl film, which we estimate in
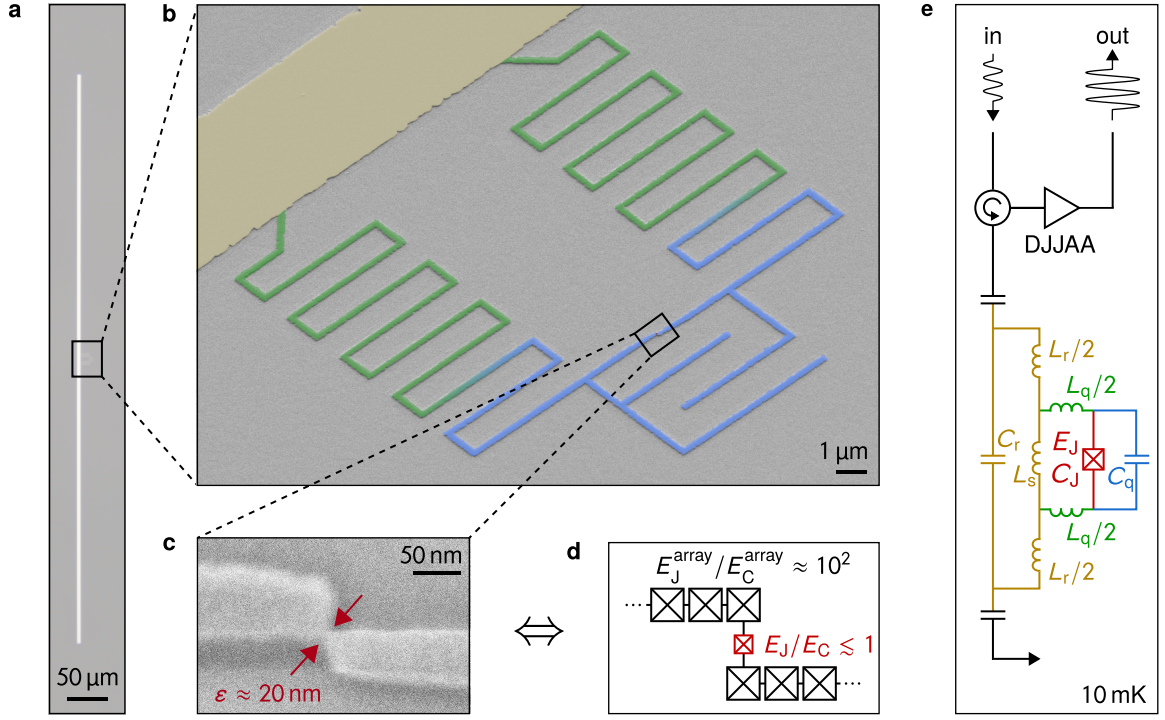
Figure 2.3: Microscope images and circuit schematics of the gralmonium sample. **a** Optical microscope image of the readout resonator with the gralmonium qubit located in the center. The resonator is implemented as a rectangular grAl strip antenna of width 4 μm and length 700 μm. **b** Zoom-in on the qubit as a false-colored scanning electron microscope (SEM) image showing the meandered grAl superinductor loop [78] (green) galvanically coupled to the readout antenna (ocher). The loop is closed by a coplanar interdigitated capacitor (blue) in parallel with the grAl nano-junction. **c** Zoom-in on the grAl nano-junction similar to Fig. 2.2b. The grAl volume on the order of ε^3 with $\varepsilon \approx 20$ nm is realized by locally confining the loop wire (red arrows). **d** Circuit model of the effective one-dimensional JJ chain implemented by the grAl nano-junction and the surrounding superinductor. **e** Lumped element circuit schematic of the gralmonium sample consisting of the qubit inductively coupled to the readout resonator. The colors of the nano-junction, qubit capacitor C_q, qubit superinductor L_q, resonator capacitor C_r, inductor L_r and shared inductor L_s match the overlay colors in panel b. The circuit is measured in single-port reflection in a cylindrical copper sample holder (cf. Appendix A) anchored at the mixing chamber stage of a dilution cryostat ($T \approx 10$ mK), with a Dimer Josephson Junction Array Amplifier (DJJAA) [6]. This figure is adapted from Fig. 1 in Ref. [1].

the range of 5 nm $< \xi < 10$ nm $< \varepsilon$ [121, 152], the nano-junction consists of a 3D network of Josephson junctions. However, the operating frequency of the circuit is well below the plasma frequency (≈ 70 GHz [123, 144]), which is why for both the nano-junction and the superinductor wire, the 3D network can be effectively considered a 1D array of SIS JJs [144] (Fig. 2.3d). While, in practice, it cannot be ruled out that the nano-junction is formed by multiple Al-AlO$_x$ interfaces, a single effective Josephson energy E_J and capacitance C_J is used to describe it analogous to a standard SIS JJ with sinusoidal current phase relation [56]. This assumption is tested by analyzing the spectrum of the gralmonium in Section 2.3.2 and more thoroughly by checking for the presence of Josephson harmonics in Section 2.4.

The difference between the effective wire JJs and the nano-junction is the order of magnitude different Josephson coupling due to the reduced cross-section. While for the superconductor we estimate $E_J^{\text{array}}/E_C^{\text{array}} \approx 10^2$, the nano-junction is expected to be in the

relevant regime for a tunnel junction in a fluxonium, $E_{\mathrm{J}}/E_{\mathrm{C}} \lesssim 1$ (cf. also Section 2.1.2). The two contributing factors for this difference are both the small Josephson coupling and intrinsic capacitance $C_{\mathrm{J}} < 1\,\mathrm{fF}$ of the nano-junction.

> " *Some people like to give funny nicknames to (even slight variations of) qubit circuits, others try to avoid it. I feel like it is a fun game to play and my new personal favorite added to the list of artificial atoms — such as transmon [60], fluxonium [67], X-mon [153], gatemon [154], gralmonium [3] — is definitely the recent "flowermon" [155].* "

The lower bound for the total charging energy of the gralmonium is fixed by adding a coplanar interdigitated capacitor C_{q} (blue in Fig. 2.3b,e) in parallel to the nano-junction such that $E_{\mathrm{C}}^{\Sigma} \approx E_{\mathrm{J}}$. Note that owing to the compact layout of the superinductor loop, the meanders close to the junction partially contribute to the intended C_{q}. This is indicated by the color gradient between green (inductive) and blue (capacitive) in Fig. 2.3b. Although the circuit is distributed due to its dense layout, we can model gralmonium in terms of an effective lumped element representation as illustrated in Fig. 2.3e as long as the operating frequencies are lower than other modes present in the distributed circuit. For the measurements discussed in the following, the sample is mounted in a sub-wavelength copper tube (see Appendix A) and measured in single-port microwave reflection employing a parametric quantum amplifier [6].

2.3.2 Spectroscopy

As mentioned in Section 2.1.2, the fluxonium-based circuit offers an efficient way to test for nano-junctions and gralmonium qubits in the intended regime: if a functioning qubit is coupled to the resonator, the resonator flux sweep shows avoided level crossings at the external flux values, at which the qubit and resonator modes match, as shown in Fig. 2.4a. Importantly, the crossings repeat periodically in flux (cf. Appendix B.2), as expected for fluxonium qubits. This is in contrast to similar crossings visible in grAl resonators subject to out-of-plane magnetic field above their geometry dependent threshold (cf. Section 1.4 and Ref. [4]). While in total more than 20 functioning gralmonium devices have been identified across more than 10 different wafers (cf. Appendix B.7), in the following we focus the discussion on one main device, which has been measured in most detail.

In Fig. 2.4b, we map out the spectrum of the gralmonium up to $14\,\mathrm{GHz}$ by following the qubit mode with two-tone spectroscopy, i.e. by monitoring the readout resonator while applying a second microwave tone at varying drive frequency f_{d}. Interestingly, the gralmonium spectrum with half-flux and zero-flux frequencies of $4.0\,\mathrm{GHz}$ and $10.8\,\mathrm{GHz}$, respectively, is reminiscent of conventional fluxonium spectra. Indeed, a joint fit of the f_{ge}
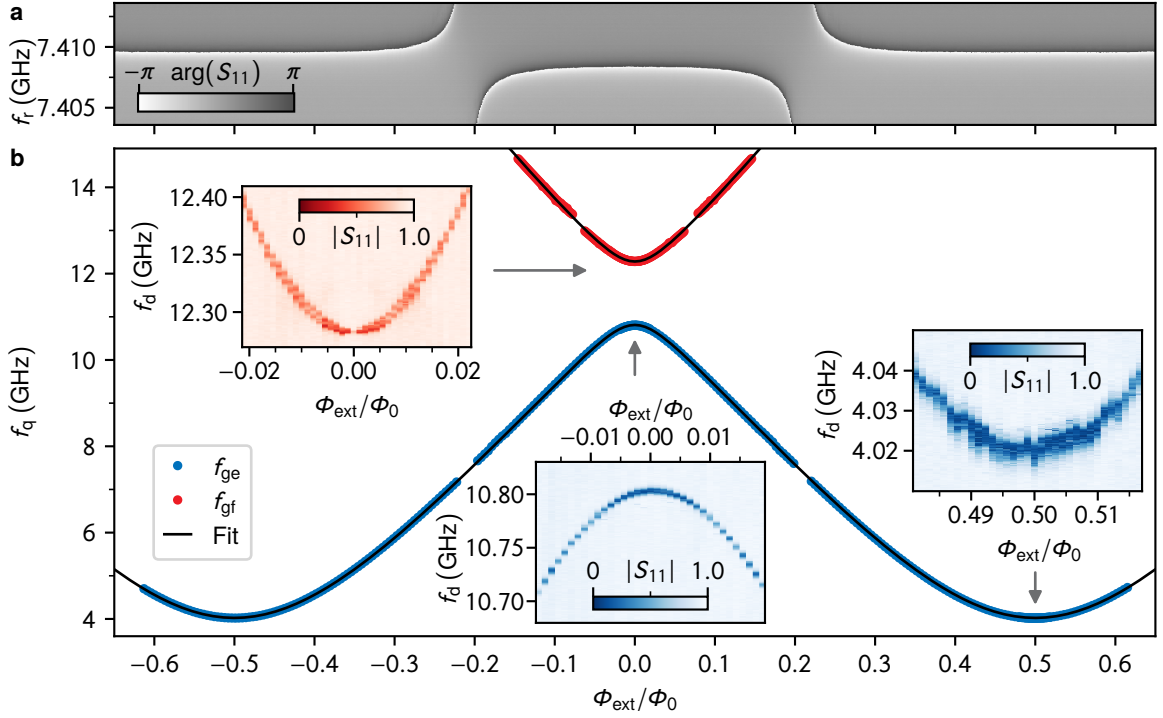
Figure 2.4: Gralmonium spectroscopy vs. external flux Φ_{ext}. a Phase response $\arg(S_{11})$ of the readout resonator measured in single-port reflection. Avoided level crossing are visible at the flux values at which the qubit mode matches the resonator frequency. **b** Two-tone spectroscopy of the gralmonium, performed by applying a second drive tone at f_d while monitoring the resonator response. The markers show extracted data for the transitions $|g\rangle \rightarrow |e\rangle$ (blue) and $|g\rangle \rightarrow |f\rangle$ (red). The empty ranges around 7.4 GHz and 13.1 GHz are due to the qubit mode crossing the resonator and the first superinductor mode, respectively. The black lines show a fit to the spectrum with the resulting qubit parameters $L_q = 285$ nH, $E_J/h = 23.4$ GHz and $C_\Sigma = C_q + C_J = 1.26$ fF as indicated in Fig. 2.3 and Table 2.1. In the insets, we present raw spectroscopy data at the flux sweet spots; the color scale corresponds to the reflection amplitude $|S_{11}|$ normalized to the maximum. This figure is adapted from Fig. 2 in Ref. [1].

and f_{gf} transition frequencies (blue and red in Fig. 2.4) based on numerical diagonalization [78, 156] of the standard fluxonium Hamiltonian [67],

$$H = 4E_C^\Sigma n^2 + \frac{1}{2}E_L\left(\varphi - 2\pi\frac{\Phi_{\text{ext}}}{\Phi_0}\right)^2 - E_J\cos\varphi, \tag{2.2}$$

matches the data (black lines). Here, the grAl nano-junction is modeled with a purely sinusoidal current-phase relation and effective Josephson energy E_J (cf. Fig. 2.3d); φ and n are the operators corresponding to phase difference across the junction and the normalized number of Cooper pairs, respectively; $\Phi_0 = h/2e$ is the superconducting magnetic flux quantum, $E_L = (\Phi_0/2\pi)^2/L_q$ the inductive energy and Φ_{ext} the external flux through the gralmonium loop. The agreement between the gralmonium spectrum and the assumption of a purely sinusoidal current-phase relation for the nano-junction is discussed in detail in Section 2.4.

Based on the fit to the spectrum, we extract a Josephson energy $E_J = 23.4$ GHz of the nano-junction, which agrees with the expected range for the dimensions of the grAl volume

Parameter	Value	Energy scale
Critical current	$I_c = 48.7\,\text{nA}$	$E_J/h = 23.4\,\text{GHz}$
Inductance	$L_q = 285\,\text{nH}$	$E_L/h = 0.573\,\text{GHz}$
Total capacitance	$C_\Sigma = 1.26\,\text{fF}$	$E_C^\Sigma/h = 15\,\text{GHz}$

Table 2.1: Overview of gralmonium circuit parameters. The values are based on the fit to the spectrum shown in Fig. 2.4b. Note that they correspond to an effective, lumped element description of the gralmonium circuit as introduced in Fig. 2.3. The extracted capacitance is the total capacitance across the junction $C_\Sigma = C_J + C_q$, including the coplanar interdigitated capacitor.

involved (see Section 2.2). Moreover, as expected, the total fitted capacitance across the junction $C_\Sigma = C_q + C_J$ is 1.26 fF is dominated by the fixed contribution from the geometrical capacitance $C_q \sim 0.8\,\text{fF}$. An overview of the fit parameters extracted from the spectrum is given in Table 2.1.

> "*If we only ever measured one "hero device", the gralmonium would be a prime contribution to the possible reproducibility crisis in science [157]. Fortunately, with a sense of pride and accomplishment, we have reproduced functioning qubits over several years, on different wafers, with different designs, across different clean-room facilities.*"

Discussing the features in the spectrum in more detail, we note that the $|g\rangle \rightarrow |f\rangle$ transition is suppressed around zero-flux (Fig. 2.4b, top left inset), which fulfills the fluxonium selection rules [67]. Contrary to expectations, the linewidth of the $|g\rangle \rightarrow |e\rangle$ transition does not get narrower when approaching the sweet spots at half- and zero-flux (Fig. 2.4b, bottom and right inset). Instead, a toggling of the qubit frequency is observed, particularly visible in the half-flux spectroscopy (bottom right inset) and occuring on a timescale of minutes (corresponding to a few traces in the data). This observation indicates the presence of critical current fluctuations as a dominating decoherence source (beyond flux noise) and will be discussed in more detail in the following section.

2.3.3 Time Domain Characterization

In order to utilize the gralmonium — as a qubit for quantum information or a detector circuit — sufficient energy relaxation (T_1) and coherence times (T_2) are important. The first is essential to enable dispersive readout of the qubit state without decay of the state populations over the time of the measurement $t_m \ll T_1$. Moreover, T_1 gives an upper bound for the coherence ($T_2 \leq 2T_1$). The coherence T_2 quantifies the decay of knowledge about the qubit state. Regarding the usage as a detector, T_2 also limits the frequency resolution achievable for detecting external signals since dephasing T_φ corresponds to the noise on the qubit frequency.
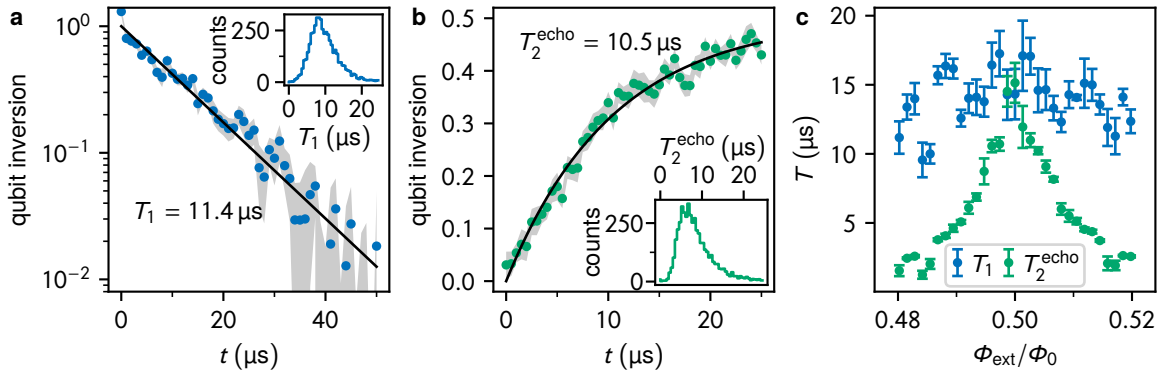
Figure 2.5: Energy relaxation and coherence of the gralmonium at half-flux bias. **a** Example of a free decay energy relaxation and **b** spin Hahn echo measurement. The black lines corresponds to exponential fits with decay times $T_1 = 11.4\,\mu s$ and $T_2^{echo} = 10.5\,\mu s$, respectively. The markers are the mean of 20 iterations, each based on 100 averaged single shot qubit measurements, and the gray error bands show the standard error of the mean over the 20 iterations. The insets contain histograms of the decay times extracted from 2000 individual iterations. **c** Extracted decay times T_1 and T_2^{echo} when sweeping the external flux around the half-flux sweet spot. The colors match the experiments in panels a,b; the markers and errorbars correspond to the mean and standard error of the mean of values from 5 repetitions of the flux sweep. This figure is adapted from Fig. 3 in Ref. [1].

In Fig. 2.5 we show standard time domain measurements of the gralmonium at half-flux. The free decay energy relaxation follows a single exponential with decay times on the order of 10 µs (Fig. 2.5a). Note that this value is comparable to fluxonium qubits based on conventional tunnel JJ, especially when considering the relatively high half-flux frequency of 4.0 GHz, for example compared to Ref. [78]. One possible limiting factor for the T_1 could be dielectric loss in the compact interdigitated capacitor [158] in parallel to the nano-junction (cf. Fig. 2.3b, highlighted in blue). Interestingly, the values for T_1 are similar between free decay experiments and quantum jump traces (cf. Appendix B.5). This can be an indication of the energy relaxation being independent of readout photon number, similar to other fluxonium qubits with grAl superinductor [9, 10].

> " *To use it as a detector, it should just be a decent qubit and does not need to break a world record for coherence.* "
>
> — A Supervisor

Hahn echo experiments with a single refocusing π-pulse are also described by an exponential decay with decay time $T_2^{echo} \sim 10\,\mu s$, which is on the order of T_1. As shown in Fig. 2.5, the regime of $T_2^{echo} \sim T_1$ is only reached close to the half-flux sweet spot due to the first-order insensitivity to flux noise. Note that the echo measurements discussed here are filtering low-frequency noise, which explains the visible improvement when approaching half-flux compared to Fig. 2.4 (bottom right inset). Based on the flux dependence, we analyze the coherence budget in Appendix B.3. For additional time domain measurements at zero-flux bias, see Appendix B.4.

So far, the gralmonium has been conforming to the expectations of a standard fluxonium in many aspects. In the following, we will see that Ramsey measurements prelude the
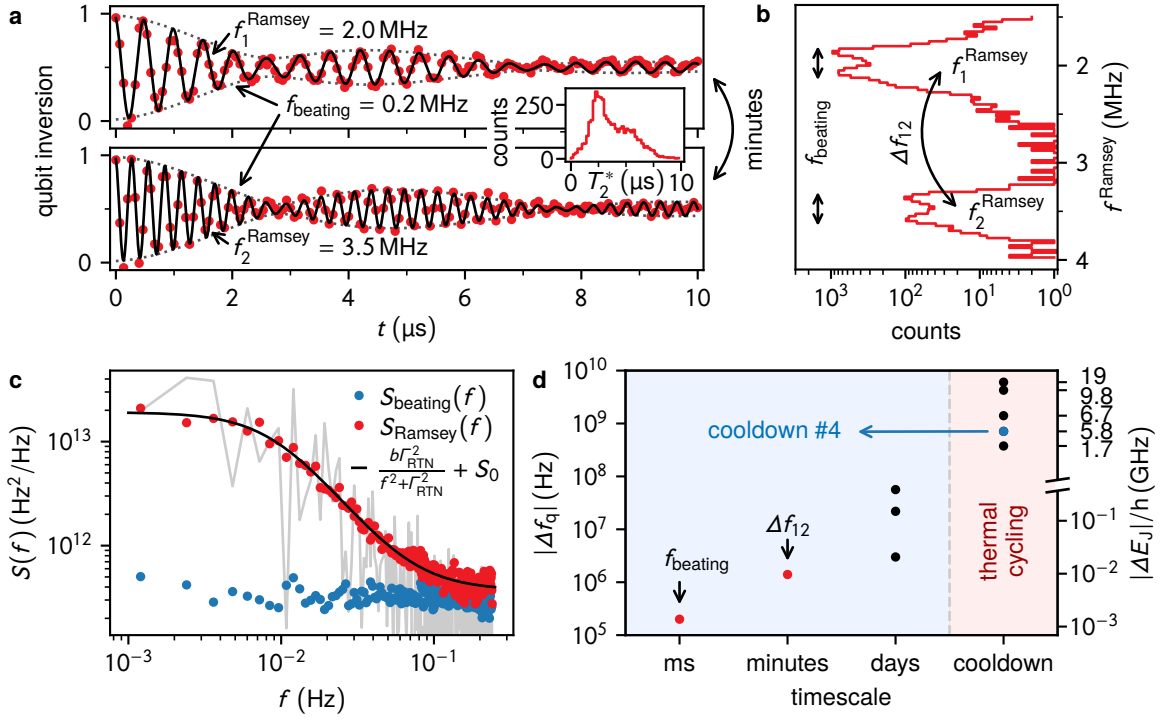
Figure 2.6: Fluctuations of the gralmonium frequency on different timescales. **a** Ramsey fringes show a beating pattern, which indicates a toggling between two qubit frequencies $f_{beating} = 0.2\,\text{MHz}$ apart (dotted gray envelope of two-frequency sinusoidal fit in black). Although the measurements in both panels were taken with nominal detuning of $2\,\text{MHz}$ the different Ramsey frequency shows a jump in the average qubit frequency by $\Delta f_{12} = 1.5\,\text{MHz}$. The inset shows a histogram of the extracted T_2^* is in the range of $1-10\,\mu\text{s}$. **b** A joint histogram of the two frequencies extracted from Ramsey fringes similar to the ones in panel a gives an overview of the involved frequency scales. **c** The power spectral density of the Ramsey frequency follows a Lorentzian shape which confirms random telegraphic noise with a rate of $\Gamma_{RTN} = 9.4\,\text{mHz}$. **d** Overview of the different timescales on which the qubit frequency changes. As shown in panels a-c, the beating $f_{beating}$ and telegraphic toggling Δf_{12} occur on a timescale of milliseconds (i.e. faster than individual points in the Ramsey measurements) and minutes, respectively. Every few days during a cooldown, the qubit frequency changes by $10-100\,\text{MHz}$ and the largest shifts are observed after thermal cycling of the cryostat. We identify changes in the nano-junction Josephson energy E_J (cf. right hand axis) as the main cause of the frequency fluctuations (see maintext). This figure is adapted from Fig. 3 and Fig. S11 in Ref. [1].

departure from these expectations. As shown in Fig. 2.6a, individual Ramsey traces at half-flux exhibit a beating of the fringes, which can be captured with a two-frequency sinusoidal fit enveloped by an exponential with decay time $T_2^* = 4.5\,\mu\text{s}$ This result corresponds to a toggling of the qubit between two transition frequencies $f_{beating} = 0.2\,\text{MHz}$ apart and on a timescale faster than the acquisition of single measurement values. We estimate this timescale to be on the order of milliseconds.

Continuing on larger timescales, the comparison of the top and bottom panel in Fig. 2.6a evidences that the average qubit frequency jumps by $1.5\,\text{MHz}$ every few minutes. Both the beating and frequency jumps are visualized in Fig. 2.6b as a histogram of the extracted Ramsey frequencies — equivalent to a Fourier transform of the fringes vs. time. Note that similar frequency fluctuations are visible also in continuous wave spectroscopy (Fig. 2.4b, bottom right inset). Indeed, the power spectrum of the qubit frequencies is dominated

by a Lorentzian, which is associated with random telegraphic noise. The switching rate $\Gamma_{\mathrm{RTN}} = 9.4\,\mathrm{mHz}$ extracted from a fit to the power spectrum confirms the timescale of the fluctuations. In addition to the described fluctuations, we observe 10–100 MHz jumps of the gralmonium frequency at half-flux every few days. Interestingly, this is the case despite the sample remaining at cryogenic temperature. Finally, as summarized in Fig. 2.5d, the largest changes in the gralmonium spectrum occur after thermal cycling of the sample.

Interestingly, the magnitude of the frequency fluctuations changes systematically with flux and is consistent with different sets of nano-junction parameters (see Appendix B.6). In fact, since the gralmonium half-flux frequency is designed to be exponentially sensitive to $E_{\mathrm{J}}/E_{\mathrm{C}}^{\Sigma}$ of the nano-junction (cf. Eq. (1.10) in Section 1.2.2) it is not surprising that the qubit is susceptible to microscopic changes in the $(20\,\mathrm{nm})^3$ volume of the grAl nano-junction or its close vicinity. In particular, the spectrum is most sensitive to E_{J} changes (Fig. 2.5e, right hand axis) because E_{C}^{Σ} is upper-bounded by the coplanar capacitance C_{q}.

> “*It looks like the gralmonium is indeed a very*
> *sensitive detector circuit, as it is designed to be.*
> *The question is: what is it detecting?*”

There are many possible sources for the fluctuations intrinsic to the grAl nano-junction, which cannot be disentangled without further measurements. One possible source could be structural changes like tunneling crystalline defects, vacancies, interstitial impurities or adsorbed molecules [43]. Alternatively, given the possibility of multiple connected AlO_x interfaces forming the effective nano-junction, charge-noise could be introduced via Aharonov–Casher interference [159] of local charges. Somewhat ironical with regard to the main motivation of implementing the gralmonium, the list of culprits also includes paramagnetic impurities, which could influence the nano-junction via magnetic field. The outlook on narrowing down the origin of the fluctuations is discussed in Chapter 4.

2.4 Josephson Harmonics in the GrAl Nano-Junction

We concluded in Section 2.3.2 that the gralmonium spectrum can be modeled assuming the sinusoidal Josephson current-phase relation Eq. (1.5) with a single effective Josephson energy E_{J} for the grAl nano-junction. In the following, we quantify how accurate this assumption is by testing the agreement between the measured gralmonium spectrum and different current-phase relations. As shown in Fig. 2.7a, in addition to the purely sinusoidal CφR, we use two CφRs including higher harmonics $\sin(m\varphi)$, $m > 1$ [2, 56]. The corresponding energy-phase relations (EφR; cf. Fig. 2.7b) are used as the Josephson term in the Hamiltonian Eq. (2.2), which can be numerically digaonalized similarly to the methodology for the standard fluxonium Hamiltonian [156]. For each version of the EφR, we fit the Hamiltonian parameters to the measured gralmonium spectrum vs. external flux (cf. Fig. 2.4b). Note that we include the coupling to the readout resonator in the model for the standard EφR in order to describe the avoided-level crossings between qubit and resonator; this task becomes computationally intensive for non-sinusoidal CφRs.
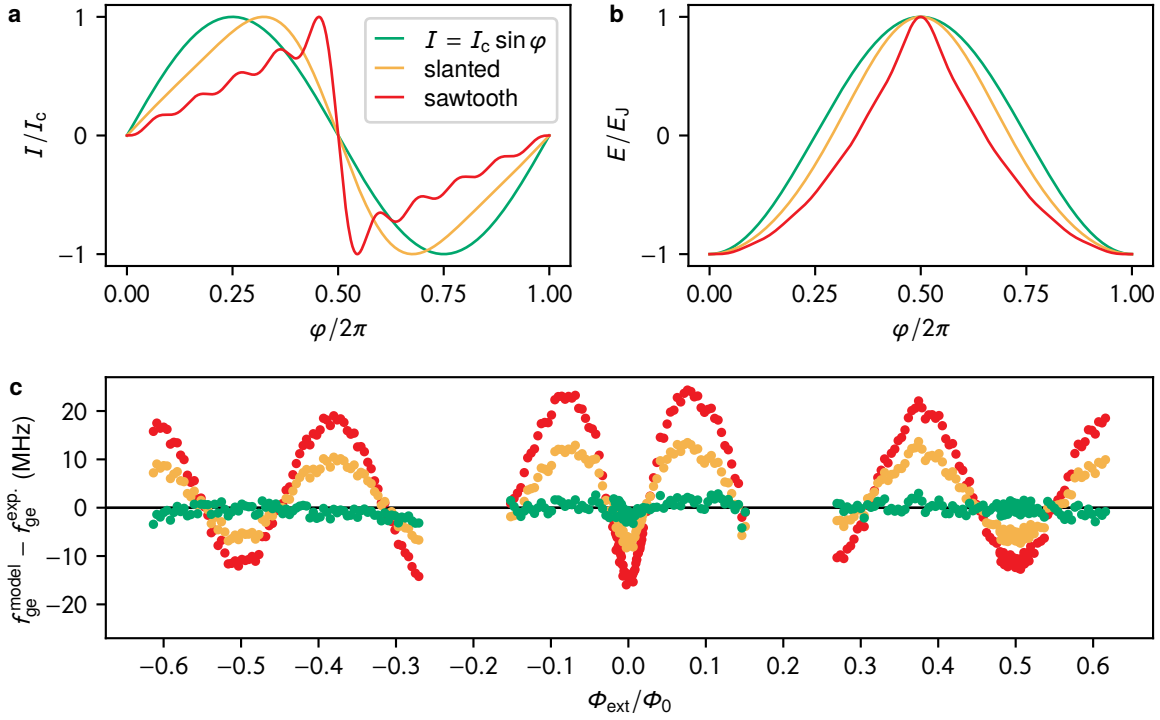
Figure 2.7: Testing for harmonics in the grAl nano-junction. **a** Current-phase relations (CφRs) used for the comparison to the measured data: The purely sinusoidal CφR, $I = I_c \sin \varphi$, is shown in green. Alternatively, a slanted CφR, $I = I_c (\sin \varphi - 0.25 \sin 2\varphi + 0.05 \sin 3\varphi)$ (orange), and a CφR close to a sawtooth, $I = I_c \sum_{m=1}^{10} (-1)^{(m+1)} \sin(m\varphi)/m$ (red) is tested. **b** Energy-phase relations (EφRs) given by integrating the CφRs in panel a. Note how the maximum of the potential at $\varphi = \pi$ gets sharper for the more slanted CφRs including higher harmonics. **c** Difference between the modeled and experimental transition frequency f_{ge} vs. external flux Φ_{ext}. The modeled frequencies f_{ge}^{model} are extracted by numerically diagonalizing and fitting the Hamiltonian Eq. (2.2) with the Josephson potential given by the EφRs in panel b to the measured frequencies $f_{ge}^{exp.}$. The interval ± 1 GHz around the avoided level crossing with the resonator ($|\Phi_{ext}/\Phi_0| \approx 0.2$) is excluded from the data. This figure is adapted from Fig. S5 in Ref. [1].

Fig. 2.7c shows the remaining deviations between modeled and measured transition frequencies $f_{ge}^{model} - f_{ge}^{exp.}$. Notably, the purely sinusoidal model (green) agrees with the experimental data within the resolution of the measurement ± 2 MHz and without systematic deviations. On the contrary, the CφRs with higher harmonic contributions lead to systematic and one order of magnitude larger deviations (orange and red). Given the spread of the measured data, we can place an upper bound of 5 % for the second harmonic contribution in the grAl nano-junction CφR. Lowering this bound would require higher resolution spectroscopy data.

In summary, analyzing the Josephson harmonics in the grAl nano-junction shows no deviation from the standard sinusoidal CφR assumed for SIS tunnel JJ within the experimental resolution. On the one hand, this confirms the modeling of the nano-junction as a zero-dimensional tunnel JJ and shows that the nano-junction, indeed, is effectively a replacement for a standard tunnel JJ in the gralmonium. On the other hand, this result draws attention to the question of what the reference value for the contribution of higher Josephson harmonics in standard Al-AlO$_x$-Al tunnel JJ would be. The next chapter is

dedicated to answering this question and enabling a quantitative comparison to the value determined for the grAl nano-junction in the gralmonium qubit.

3 Josephson Harmonics in Tunnel Junctions

We have seen in the previous chapter that the grAl nano-junction current-phase relation (CφR) is indistinguishable from a purely sinusoidal form. In order to provide context for this statement, this chapter documents the second main result of the thesis: the observation of corrections to the sinusoidal CφRs in conventional Al-AlO$_x$-Al tunnel Josephson junctions (JJs) in the form of harmonics. The chapter starts by giving an overview of CφR in different types of Josephson weak links. Starting from the CφR of single conduction channels, we derive an expectation for the magnitude of harmonics in a tunnel JJ based on a mesoscopic model of the barrier inhomogeneity. Next, we show that spectroscopy measurements of transmon qubits across several laboratories serve as a sensitive probe of the Josephson potential. This allows us to quantify the magnitude of Josephson harmonics in these samples. Finally, the implications for transmons beyond the spectrum are discussed. This chapter is adapted in parts from Willsch, Rieger et al., arXiv:2302.09192, 2023 (Ref. [2]).

3.1 Setting an Expectation for Josephson Harmonics

3.1.1 CφR in Different Types of Weak Links

Since Josephson's initial prediction [53] and further theoretical treatment [54, 55] of the tunnel current across superconducting electrodes separated by a thin insulating barrier, an extensive body of theoretical and experimental work has refined the initial understanding for the Josephson effect [56]. Soon after Josephson's seminal work, the effect has been studied and measured in a variety of other *weak links*, in which the superconducting electrodes are separated by a normal metal region, semiconductor or geometrical constriction, among others [160]. Notably, in his description of the sinusoidal current-phase relation (CφR) for tunnel junctions, Josephson himself already makes the following statement [54]:

> *The microscopic theory [53] shows that, in the limit of weak coupling, only first harmonics enter [and they] are good approximations for the barriers normally used in tunneling experiments.*

> — B. D. Josephson (1964)

The quote makes clear that the purely sinusoidal CφR is an idealized assumption and, in reality, the microscopic structure of the junction and the charge transport across it can play a role for an accurate modeling of the Josephson effect.

In fact, with the exception of tunnel junctions, non-sinusoidal CφRs are a common occurrence in all other types of weak links. As an example, for superconductor-constriction-superconductor (ScS) weak links, in which a continuous superconducting film is locally confined to dimensions on the order of the coherence length, the expected form of the CφR strongly depends on the length and transverse dimensions of the constriction as well as the temperature [56]. Generally, the supercurrent across a Josephson weak link can be described in terms of an *Andreev reflection* picture [161]: electron-like quasiparticles get reflected as holes on one side of the weak link and the holes are reflected as electrons on the other interface. Via this cyclic process of Andreev reflections, Cooper pairs are effectively transported across the junction. Electron-hole interference in the weak link region leads to standing waves with quantized energy levels, referred to as *Andreev bound states* [162].

Andreev physics can be particularly well studied in weak links, in which the superconducting electrodes are separated by a normal metal (SNS) or semiconductor region. The main reason is that these types of structures can be designed to contain only a low number of individual conduction channels. Moreover, the transparency of the channels can be tuned via gate electrodes in the vicinity of the weak link. The shape of the Andreev bound state CφR and its dependency on the channel properties is fundamental for applying the Andreev picture to tunnel junctions, as we will see in more detail in the following sections. Interestingly, in recent years, the approach of integrating gate-tunable semiconductor nanowire weak links as Josephson elements in microwave superconducting circuits and cQED schemes has gained increasing interest with applications including hybrid superconductor-semiconductor qubits [154, 163], parametric amplification [164] and Andreev-spin qubits [165, 166].

> "*A junior and a senior physicist walk into a bar. The junior says:*
> "*I have never heard about harmonics in tunnel junctions before.*
> *This is exciting news!", agitatingly waving a preprint in the air.*
> *The senior berates him: "Oh, this is well known for decades!".*
> *Both turn to the authors of the Josephson Harmonics paper and*
> *complain: "So why do you only realize this NOW?".*"

Given the extensive body of literature on the intricate details of CφRs in various weak links, why is the purely sinusoidal Josephson CφR ordinarily considered a good approximation for tunnel junctions? We will address this question in Section 3.1.3 after being equipped with an understanding of the properties of the Andreev bound state CφR in individual conduction channels.

3.1.2 Single Conduction Channel Current-Phase Relation

The energy of an Andreev bound state for a conduction channel with transmission coefficient (also typically denoted transparency) $0 \leq T \leq 1$ is given by [56]

$$E_{\pm}(\varphi) = \pm \Delta \sqrt{1 - T \sin^2(\varphi/2)} \,, \tag{3.1}$$

where Δ is the superconducting gap of the electrodes and φ the phase across the junction. The two branches indicated with $+$ and $-$ refer to the different directions of the supercurrent. Fig. 3.1a shows the Andreev bound state energy-phase relation (EφR) for different transparencies T. In the low-transparency limit the two branches remain close to the gap Δ (green curve) while for high transparency $T \to 1$ the branches would become non-differentiable and touch at $\varphi = \pi$ (red curve).

The corresponding CφR of a single conduction channel is proportional to the derivative of the EφR Eq. (3.1),

$$I(\varphi) = \frac{e\Delta}{2\hbar} \frac{T \sin \varphi}{\sqrt{1 - T \sin^2(\varphi/2)}} \,, \tag{3.2}$$

in which e is the electron charge and $\hbar$ the reduced Planck constant. Inherited from the shape of the EφR, the CφR is close to sinusoidal for $T \to 0$ and approaches a sawtooth-like shape for $T \to 1$ (cf. Fig. 3.1b). Since it is a periodic function of φ, the shape of the CφR can be analyzed intuitively as a Fourier series

$$I(\varphi) = \frac{e\Delta}{2\hbar} \sum_{m=1}^{\infty} c_m(T) \sin(m\varphi) \,, \tag{3.3}$$

with the Fourier coefficients $c_m(T)$ of the m-th Josephson harmonic in the CφR depending on the transparency of the channel.

The relative magnitude of the coefficients is shown in Fig. 3.1c for different transparencies, illustrating several relevant properties. First of all, the sign of the coefficients alternates between odd and even orders. Moreover, the magnitude decays the higher the order such that the harmonics are generally a correction to the purely sinusoidal contribution given by c_1. Finally, the harmoncis stay relevant to much higher order for higher transparency channels compared to low-transparency channels. For this reason, both limits are discussed in more detail in the following.

Low-Transparency Limit

In the limit of $T \ll 1$ the single channel CφR, Eq. (3.2), reduces to the familiar purely sinusoidal Josephson CφR, $I = I_c \sin \varphi$, with the critical current given by the channel transparency T and the prefactor of Eq. (3.2). In this limit, the remaining relative magnitude of each harmonic relative to the previous would be on the order of [2]

$$\frac{c_{m+1}}{c_m} \sim -\frac{m - 1/2}{4m} T \,, \tag{3.4}$$
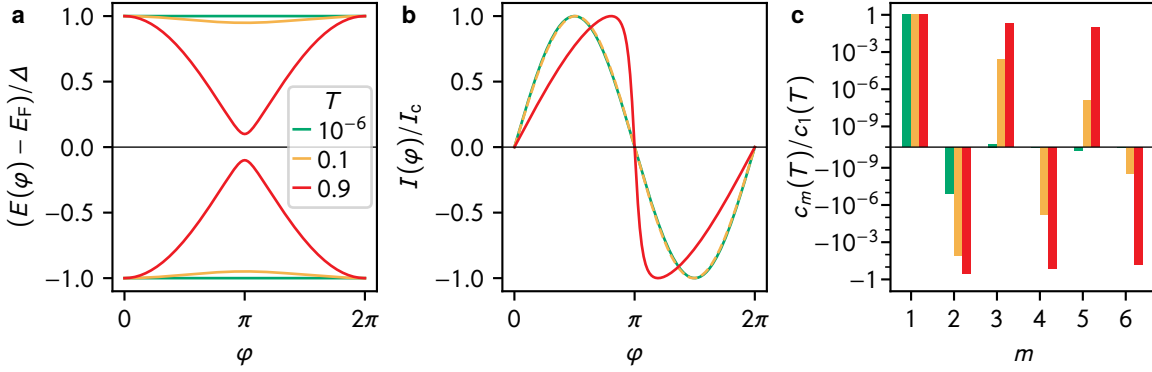
Figure 3.1: Current-phase-relation of single conduction channels. **a** Energy-phase relations of an Andreev bound state in a weak link for different channel transparencies T as given by Eq. (3.1). The energy is relative to the Fermi energy E_F and normalized by the superconducting gap of the electrodes Δ. **b** Current-phase relations (CφRs) corresponding to the transparencies in panel a as given by Eq. (3.2). Each CφR is normalized to its maximum current, the critical current I_c. The CφR for $T = 0.1$ is plotted as a dashed line to leave visible the one for $T = 10^{-6}$. **c** Order m fourier coefficients $c_m(T)$ of the CφRs in panel b normalized to the coefficient of the first order c_1. Note the alternating sign of the coefficients and the transparency-dependent decay in magnitude. The bars of coefficients below a magnitude of $|c_m| < 10^{-9}$ are exaggerated to remain visible. The colors in panels b and c correspond to the ones in panel a.

which is proportional to the transparency T itself. For example, the second harmonic only contributes at a level of $-T/8$ relative to the first harmonic (cf. green bar for $m = 2$ and $T = 10^{-6}$ in Fig. 3.1c). As a consequence the presence of harmonics can indeed be considered irrelevant for a channel with sufficiently low transparency .

Fully Open Point Contact

In the opposite limit, a single channel with $T \rightarrow 1$ would correspond to a fully open point contact, for which the CφR is shaped sawtooth-like with coefficients [2]

$$\frac{c_{m+1}}{c_1} = (-1)^{(m+1)} \frac{3m}{4m^2 - 1} \; . \tag{3.5}$$

This limit can be seen as the upper limit for the higher harmonic contributions in Eq. (3.3) as values of the Fourier coefficients c_m above the ones in Eq. (3.5) would be unphysical.

3.1.3 Mesoscopic Model of a Tunnel Junction

Based on the results of the previous section, we can discuss the case of typical tunnel junctions employed in superconducting circuits. In this case, the charge transport across (and the CφR of) the full junction is given by the sum over contributions from multiple conduction channels [56, 167, 168], as sketched in Fig. 3.2a. Inherited from the low-transparency limit of a single channel (see previous section), the total CφR would also be purely sinusoidal if all channels have sufficiently low transparency.

Since, in this case, the critical current of the JJ is proportional to the sum of transparencies and the resistance of the JJ is on the order of the superconducting resistance quantum, one can estimate the number of conduction channels and their transparency by assuming a perfectly homogeneous barrier. Concretely, for an Al-AlO$_x$-Al junction with dimensions on the order of $(100\,\text{nm})^2$, one finds a number of channels on the order of 10^6 with transparency $T \sim 10^{-6}$ [169, 170]. In some sense, estimating the transparency with this approach is a "self-fulfilling prophecy" as it relies on summing the transparencies of sinusoidal contributions, which is apparently validated by the resulting value of $T \ll 1$.

Realistically, a perfectly homogeneous barrier is only an approximation of the complex microscopic reality for conduction channels in a mesoscopic tunnel JJ. Due to the many degrees of freedom involved, the CφR can be seen as a unique finger print linking the microscopic charge transport and the macroscopic supercurrent through the junction. Since, in principle, one would need to consider as many degrees of freedom in the total CφR as conduction channels, it is convenient to reduce this complexity by modeling the large number of conduction channels as a distribution of transparencies $\rho(T)$ described by only a few parameters. This approach allows to get an intuition for the expected magnitude of harmonics in tunnel JJs.

In fact, some universal distributions of the form $\rho(T) \propto T^{-p}/\sqrt{1-T}$ are discussed in the literature, corresponding to different assumptions about the properties of the weak link [56, 171–173]. Specifically, $p = 1/2$ describes a chaotic dot connected to superconducting leads by ballistic point contacts [174], $p = 1$ represents the KO-1 model by Kulik and Omelyanchuk [175] and $p = 3/2$ a disordered interface [171]. Interestingly, these distributions have in common that they diverge both for $T \to 0$ and $T \to 1$. However, due to the parameters for typical AlO$_x$ barriers and aluminum electrodes, one should not expect an AlO$_x$ tunnel JJ to be described by these universal distributions [2].

Instead, we base our own model on the observation that standard AlO$_x$ barriers, grown by static oxidation of evaporated aluminum electrodes, are inhomogeneous in nature. For example, these inhomogeneities can include contaminants, atomic scale defects [176] and random crystalline orientations of the grains forming the electrodes. As a minimal contribution, we should expect the thickness of the barrier to be varying around an average thickness on the order of 2 nm as supported by transmission electron microscope (TEM) images (cf. Fig. 3.2b) as well as molecular dynamics simulations (Fig. 3.2c) similar to the ones in [177, 178]. The images and simulations (see Appendix C.6 for details) reveal that typical thickness variations are on the order of several 10 % of the average thickness. Based on this observation and measurements reported in the literature [179, 180], we can model the local barrier thickness d as a Gaussian distribution truncated for $d \geq 0$ with average thickness $\bar{d}$ and standard deviation σ_d,

$$\rho(d; \bar{d}, \sigma_d) = \frac{2\Theta(d)}{1 + \text{Erf}(\bar{d}/\sqrt{2}\sigma_d)} \frac{1}{\sqrt{2\pi}\sigma_d} \exp\left(-\frac{(d - \bar{d})^2}{2\sigma_d^2}\right), \qquad (3.6)$$

as illustrated in Fig. 3.2d (bottom panel). Here, Θ is the Heaviside step function and Erf the error function, ensuring $d \geq 0$ and normalization of the distribution, respectively.
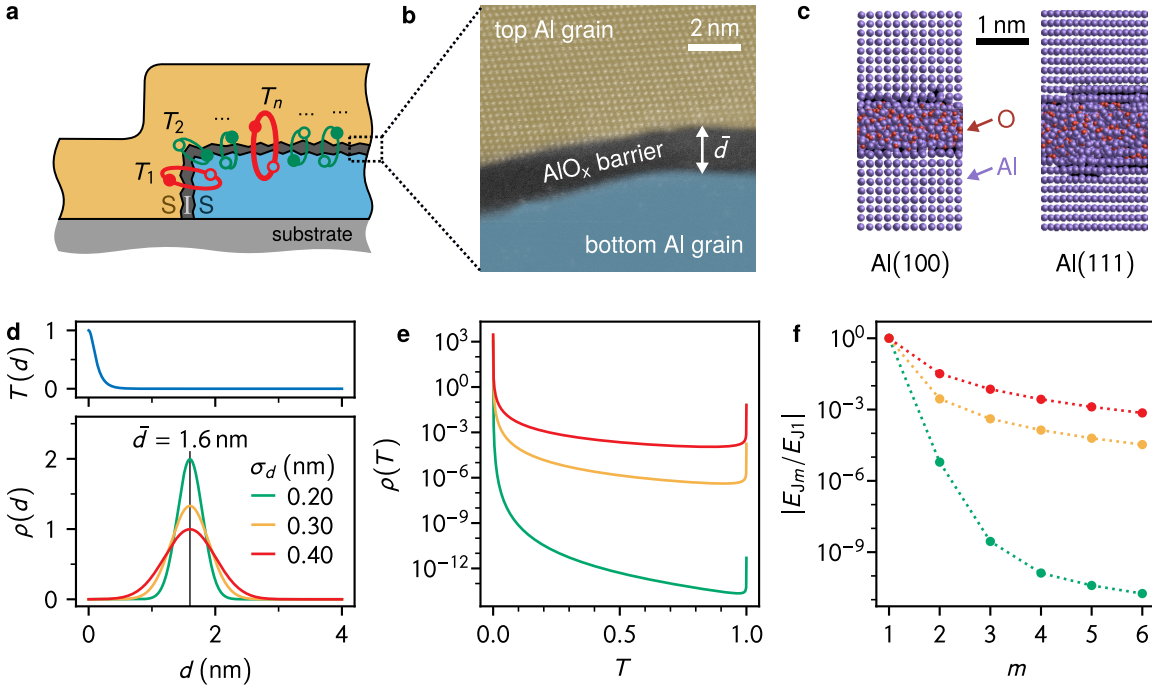
Figure 3.2: Mesoscopic model of harmonics in a tunnel junction. **a** Schematic of the cross-section of a superconductor-insulator-superconductor (SIS) tunnel JJ. The charge transport across the barrier is given by a large number (of order 10^6) of conduction channels with a distribution of transparencies T_n as sketched for multiple low-and a few high-transparency channels in green and red, respectively. **b** False-colored high-angle annular dark field scanning transmission electron microscope (HAADF-STEM) image of an AlO_x tunnel barrier fabricated by shadow evaporation. The average barrier thickness $\bar{d}$ is on the order of 2 nm (white arrow). Due to zone axis alignment, individual columns of atoms are resolved in the top electrode and reveal atomic-scale variations in the barrier thickness. Additional STEM images with thickness variations and structural defects such as grain boundaries are shown in Appendix C.6. **c** Molecular dynamics simulation of AlO_x barrier growth. Note the thickness variations within the same crystalline orientation of the Al electrodes and, in particular, between Al(100) and Al(111). **d** Gaussian distributions of thickness $\rho(d)$ with different standard deviations σ_d around an average thickness $\bar{d} = 1.6$ nm (bottom panel). The top panel shows the thickness-dependence of transparency for a rectangular tunnel barrier (cf. Eq. (3.7)), which is used to calculate the transparency distributions $\rho(T)$ shown in panel **e**. Note that all distributions have the most weight towards $T \to 0$ but also show a divergence for $T \to 1$. The relative contribution of the low-transparency regime $T \ll 1$ decreases with larger thickness variation σ_d. **f** Relative magnitude of Josephson harmonics in the energy-phase relation (cf. Eq. (3.8)) for the transparency distributions in panel e. Note that the magnitude of higher harmonics ($m \geq 2$) increases with stronger thickness variation σ_d. The colors in panels e and f correspond to the ones in panel d. Panels a-c of this figure are adapted from Fig. 2 in Ref. [2].

Assuming a rectangular tunnel potential for the barrier, the dependence of transparency (i.e. the transmission probability) on the thickness follows [181]

$$T(d) = \frac{1}{1 + a^2 \sinh(d/d_0)}, \quad (3.7)$$

with the parameters $a^2 = 2.87$ and $d_0 = 0.21$ nm describing height and width of the tunnel barrier and their values being calculated based on a literature review [2]. The dependency is shown in the top panel of Fig. 3.2d. Using Eq. (3.7), the Gaussian thickness distribution

of Eq. (3.6) can be transformed into the transparency distribution vs. thickness $\rho(T; \bar{d}, \sigma_d)$ as shown in Fig. 3.2e.

Similar to the aforementioned universal distributions in the literature, the mesoscopic model leads to the strongest contributions of transparencies towards $T \to 0$ and $T \to 1$. The first observation should be very well expected since almost all of the thicknesses in the Gaussian distribution lead to vanishing transparencies according to the exponential decay of Eq. (3.7) for $d \gg d_0$. The divergence at $T \to 1$ is explained by the fact that, although the probability for small thicknesses $d \to 0$ is vanishingly low in the Gaussian model, the thickness-dependence of the transparency Eq. (3.7) flattens towards $T = 1$ in the same regime. As a consequence, the relative weight of the high-transparency contributions is very sensitive to the standard deviation of thickness σ_d in respect to the average thickness $\bar{d}$.

Based on this result, the Josephson enegies of harmonics in the energy-phase relation can be calculated by integrating the Fourier coefficients $c_m(T)$ with weight given by the transparency distribution $\rho(T; \bar{d}, \sigma_d)$:

$$E_{Jm} = \frac{1}{m} \int_0^1 dT \, \rho(T; \bar{d}, \sigma_d) \, c_m(T) \, . \tag{3.8}$$

The relative Josephson energies $|E_{Jm}/E_{J1}|$ of order m resulting from the mesoscopic model are shown in Fig. 3.2f. Remarkably, the contribution of the second harmonic can be in the percent range for 20 % variations of the barrier thickness.

In summary, based on modeling the tunnel barrier with realistic assumptions on the inhomogeneity we expect percent-level higher harmonic contributions in the CφR of Al-AlO$_x$-Al tunnel JJs. While the mesoscopic model gives a powerful intuition for the magnitude of harmonics in standard AlO$_x$ tunnel JJs, it is important to also discuss the limitations of the approach. In particular, it should be emphasized that the magnitude of harmonics in the model mainly depends on the relative thickness variations $\sigma_d/\bar{d}$ instead of each parameter individually. As a consequence, the model should not be seen as a tool to accurately determine the absolute value of the average barrier thickness or its standard deviation. Moreover, the model cannot properly describe the harmonics in junctions close to the point-contact limit since the only way to capture such terms is by decreasing $\bar{d}/\sigma_d$ to unreasonably low values.

3.2 Transmon as a Testbed for the Energy-Phase Relation

Equipped with an expectation for the magnitude of harmonics in standard Al-AlO$_x$-Al tunnel junctions, the question is how to experimentally access these contributions. In fact, it can be challenging to measure percent-level corrections to a purely sinusoidal CφR with standard direct-current (DC) methods [56]. As an example, switching current measurements are mostly sensitive to the maximum height of the CφR and not the precise shape of it [140, 182]. Moreover, in SQUID-based experiments a tunnel junction is typically

used as a reference junction in order to characterize the non-sinusoidal CφR of another weak link of interest [183]. In general, for any experiment trying to determine the CφR, the phase across the junction is determined by the circuit into which it is embedded.

In this study we use transmon superconducting qubits (cf. Section 1.2.2 and Ref. [60]) to access Josephson harmonics in standard tunnel junctions. As shown in Fig. 3.3a the discrete levels of the transmon are a sensitive probe of the potential defined by the EφR of the junction. The main benefit of using transmons is their simple circuit topology, i.e. in principle the junction is only shunted by a large capacitor. Moreover, the transmon transitions in the GHz-regime can be measured with high accuracy by circuit quantum electrodynamics techniques such that even relative frequency deviations smaller than 10^{-3} are resolvable.

To support the findings with evidence across the community, we consider devices fabricated and measured in several laboratories: (i) a transmon from Karlsruhe Institute of Technology (KIT), measured in 3 successive cooldowns, (ii) a transmon from Ecole Normale Supérieure (ENS) Paris (same device as in Ref. [184]), (iii) a frequency-tunable transmon from University of Cologne (Köln) (similar setup and device as in Ref. [110]), and (iv) 20 qubits from the IBM *Hanoi* processor. All transmons are based on Al-AlO$_x$-Al tunnel junctions. For an overview of sample properties see Appendix C.1. For each qubit, the spectroscopy data includes the transition frequencies f_{0j} — measured in terms of j-photon transitions f_{0j}/j for the levels $j = 1, 2, \ldots$ — as well as the readout resonator frequencies $f_{\mathrm{r},j}$ depending on the transmon state $j = 0, 1$. Moreover, for the Köln sample the data contains the offset charge dispersion amplitudes δf_j.

In order to test the agreement with different junction CφRs, the measured transition frequencies are compared to the values obtained by diagonalizing different model Hamiltonians. As a baseline model, we use the *standard transmon model*,

$$H_{\mathrm{std}} = 4E_{\mathrm{C}}(n - n_{\mathrm{g}})^2 - E_{\mathrm{J}} \cos \varphi + H_{\mathrm{res}}, \tag{3.9}$$

as introduced in Eq. (1.7) but additionally considering the readout resonator interaction,

$$H_{\mathrm{res}} = \Omega a^\dagger a + Gn(a + a^\dagger) \tag{3.10}$$

where Ω is the bare resonator frequency, G is the electrostatic coupling strength between resonator and transmon, and $a^\dagger$ (a) is the bosonic creation (annihilation) operator of the resonator mode. Including H_{res} accounts for the dressing of the states due to hybridization between transmon and resonator [60, 85, 185, 186]. The free parameters $E_{\mathrm{C}}, E_{\mathrm{J}}, \Omega, G$ are obtained by solving the inverse eigenvalue problem [187–190] for the measured spectroscopy data (see Appendix C.3 for details).

Fig. 3.3b shows that the standard transmon model Eq. (3.9) fails to describe the measured frequency spectra for all samples. The deviations between model and experiment are much larger than the measurement uncertainty, for which a conservative upper bound would be 1 MHz, and they increase systematically with higher transition number. Trivially, the model is able to match the first two transition frequencies, f_{01} and f_{02} with the two free parameters E_{J} and E_{C}. In contrast, the third transition f_{03} can already deviate by more than
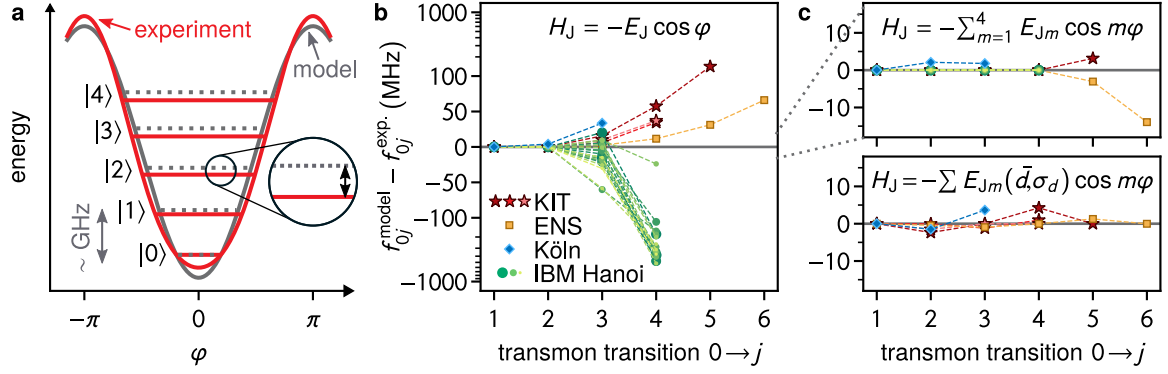
Figure 3.3: Transmon as a testbed for the energy-phase relation. **a** The discrete levels of a transmon qubit probe the Josephson potential. Thanks to the sensitivity of RF measurements even relative deviations lower than 10^{-3} can be detected between the transition frequencies in the GHz range expected for a purely $\cos\varphi$ potential (grey line and dotted grey levels) and potentials including higher harmonics (red). **b** Deviation between the frequencies f_{0j}^{model} predicted by the standard transmon model Eq. (3.9) and the measured transitions $f_{0j}^{\text{exp.}}$ for transmon devices at KIT (red stars), ENS (yellow squares), Köln (blue diamonds), and IBM (green circles). Three successive cooldowns are shown for the KIT sample in dark red to bright red. The Köln markers are based on one set of transition frequencies selected from a frequency sweep (cf. arrow in Fig. 3.5a). The IBM markers show 20 qubits of the IBM *Hanoi* processor with varying marker size and shade of green. Note that the vertical scale is linear between ±100 MHz and logarithmic otherwise. The lines between markers are guides to the eye. **c** Similar to panel b but with the modeled frequency given by the Josephson harmonics Hamiltonian Eq. (3.11). The top panel shows a phenomenological model truncated at E_{J4}. The bottom model shows the mesoscopic model in which the E_{Jm} are parameterized in terms of the average barrier thickness $\bar{d}$ and standard deviation σ_d (cf. Section 3.1.3). This figure is adapted from Fig. 2 and Fig. 3 in Ref. [2].

10 MHz. The direction of deviations can be both positive (KIT, ENS, Köln) and negative (most IBM transmons). Notably, deviations similar to the ones observed in our data are present also in previously published transmon spectroscopy [191–193] (see Appendix C.2 for details).

As shown in Fig. 3.3c, the agreement with measured spectra can be improved by orders of magnitude by using a *Josephson harmonics model*

$$H_{\text{har}} = 4E_{\text{C}}(n - n_{\text{g}})^2 - \sum_{m \geq 1} E_{Jm} \cos(m\varphi) + H_{\text{res}}. \qquad (3.11)$$

As discussed in Section 3.1.3, the energies E_{Jm} are generally a unique result of each junction's channel-transparency distribution $\rho(T)$. For this reason, we consider here two simplified models to treat the E_{Jm}: (i) a phenomenological model truncated at the 4th order (top panel of Fig. 3.3), i.e. with $E_{J1}, \ldots, E_{J4}$ as free parameters and (ii) the mesoscopic model discussed in the previous section (bottom panel), in which the E_{Jm} are parametrized based on the barrier inhomogeneity. Both models capture the experimental spectroscopy data up to at maximum ±15 MHz deviations.

The phenomenological model allows to extract the first four best-fit E_{Jm} although without providing physical intuition for their resulting values (listed in Appendix C.3). In order to apply the same methodology to all samples, we fix the value of E_{C} for each device based on

finite element simulations and fit the remaining free parameters in the model Eq. (3.11). As a consequence, the model guarantees agreement with the lowest 4 transition frequencies. In particular, this leads to a perfect fit for the IBM qubits, for which only 4 transition frequencies are available in the data. Notably, despite the phenomenological approach and truncating at the 4th order, many samples have physically reasonable E_{Jm} coefficients while some devices need up to $m = 6$ terms (cf. following section).

As outlined in detail in Section 3.1.3, the mesoscopic model allows to calculate the E_{Jm} depending on the average barrier thickness $\bar{d}$ and standard deviation σ_d according to Eq. (3.8). Consequently, only 2 degrees of freedom are added compared to the standard transmon model. Despite this simplicity, the model can describe the KIT, ENS and Köln samples. In contrast, the IBM data cannot be modeled in this way as the E_{Jm} required to explain the transition frequencies remain close to the point-contact limit. The obtained model parameters $\bar{d}$ and σ_d are on a reasonable order of magnitude compared to the expectations from STEM imaging and molecular dynamics simulation (cf. Fig. 3.2).

3.3 Magnitude of Harmonics in Tunnel Junctions

We have seen in the previous section, that including Josephson harmonics in the transmon Hamiltonian improves the agreement with measured spectroscopy data by orders of magnitude across all devices. However, there are several considerations which we have to take into account when interpreting these results. In this section, after discussing the issues concerning the model and methodology, we instead utilize an approach which allows to extract the range for the magnitude of harmonics consistent with the experimental data.

First of all, by fitting a model including Josephson harmonics to the data, we force the additional degrees of freedom in the model to capture all deviations of the experimental data from the standard transmon model shown in Fig. 3.3b. Consequently, this methodology ignores other contributions in the Hamiltonian, which might be missing compared to an accurate description of the real samples. Thanks to the simplicity of the transmon circuit, it is generally possible to include additional terms in the model and test their consequences quantitatively. In detail, we have considered the following additional contributions: stray inductance in the JJ leads, hidden modes coupled to the qubit, the coupling between qubits as present on the IBM multi-qubit device, or an asymmetry in the superconducting energy gaps. By including these additional terms in the transmon Hamiltonian, we have confirmed that they contribute to varying degree but cannot explain the measured deviations (cf. Appendix C.4), especially not consistently across devices.

> "*The point is that, whenever we propose a solution to a problem, we ought to try as hard as we can to overthrow our solution, rather than defend it. Few of us, unfortunately, practice this precept; but other people, fortunately, will supply the criticism for us if we fail to supply it ourselves.*"
>
> — Karl Popper, The Logic of Scientific Discovery, 1959
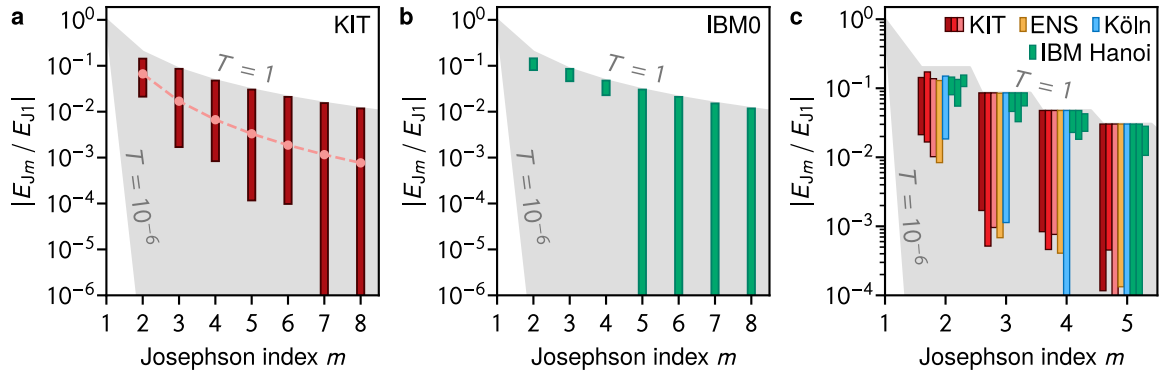
Figure 3.4: Observed magnitude of Josephson harmonics in tunnel junctions. **a** Ranges of harmonics E_{Jm} consistent with the measured spectrum for the KIT sample. The blue bars are obtained by scanning all sets of E_{Jm} up to $m = 10$, which are able to reproduce the measured spectrum. Note that harmonics up to $m = 6$ are required at a level above 10^{-4} relative to E_{J1} while the bars for higher orders extend to below 10^{-6}. The shaded gray area indicates the range of harmonics between the upper limit of the fully open point contact ($T = 1$) and the lower limit of a homogeneous barrier with $T = 10^{-6}$ for all channels (see maintext). The rose markers and dashed line indicates the set of E_{Jm} obtained from a fit to the mesoscopic model (cf. Fig. 3.3c). **b** Same as panel a but for qubit 0 of the IBM *Hanoi* processor. Note that the harmonics up to $m = 4$ are required to be close to the point-contact limit. **c** Comparison of harmonics ranges for several transmon samples as introduced in Fig. 3.3. Note that all devices require a percent-level contribution of the second harmonic. This figure is adapted from Fig. 3 and Fig. S5 in Ref. [2].

The other critical issue with the methodology could be that by simply introducing more degrees of freedom, the Josephson harmonics model can capture experimental data with better agreement. This can be particularly problematic when using the phenomenological model, which includes a number of higher harmonic Josephson energies E_{Jm} each of which adds an additional degree of freedom. A directly related concern is the question of how many E_{Jm} should be included; in particular, is it reasonable to truncate the model at order $m = 4$ as shown in the top panel of Fig. 3.3c. Interestingly, the mesoscopic model implies that many experimental spectra can in fact be matched with two additional degrees of freedom only, based on which all E_{Jm}-coefficients are parameterized.

> " *With four parameters I can fit an elephant, and with five I can make him wiggle his trunk.* "
>
> — JOHN VON NEUMANN (1953) [194]

To address the concerns described above, we can utilize the following procedure to extract information about the magnitude of Josephson harmonics from the measured spectroscopy. On purpose, we employ a harmonics model with more degrees of freedom than available in the data, i.e. for our spectroscopy we include E_{Jm}-terms up to order $m = 10$. As a result, we expect multiple sets of $(E_{J1}, E_{J2}, \ldots)$ to be able to reproduce exactly the measured spectrum of each sample. We find the range of these solutions by scanning all relevant combinations of E_{Jm} (for details see Appendix C.3) between the two limiting cases of the fully open point contact and the low-transparency case (cf. Section 3.1.2). Particularly relevant is the

minimum possible value of each harmonic in order to still be able to describe the measured data, as it informs about the relevance of this order.

The result of this procedure is illustrated in Fig. 3.4 by indicating the ranges of relative harmonics $|E_{Jm}/E_{J1}|$ consistent with the measured spectra as vertical bars from the minimum to maximum possible value. As an example, in the KIT transmon (Fig. 3.4a), the ranges for $m = 7$ and $m = 8$ extend to a level below 10^{-6} which implies that the model could have been truncated at the 6th harmonic without a relevant change in the accuracy. On the other hand, the minimum required relative contribution of harmonics up to $m \leq 6$ is on the level of 10^{-4} or higher. As another example, the same procedure for qubit 0 of the IBM *Hanoi* processor (Fig. 3.4b) requires all contributions up to $m = 4$ at percent levels and is compatible with vanishing higher orders $m \geq 5$.

Remarkably, as shown by the sample overview Fig. 3.4c, the contribution of the second Josephson harmonic is in the few percent range across all samples. We note that this holds even after considering additional corrections such as series inductance or gap asymmetry in the superconducting electrodes (cf. Appendix C.4). The ranges are also consistent with the Josephson harmonics ratios corresponding to the mesoscopic model for the samples which can be described by it (cf. the rose markers and line for the KIT sample in Fig. 3.4a). Note that the barrier for the KIT sample seems to evolve towards lower harmonics contributions, potentially due to aging between cooldowns 1 and 2, and thermal annealing between cooldowns 2 and 3. Based on the minimum required contribution of harmonics, the procedure presented here implies the presence of at least one conduction channel with transparency $T \gtrsim 0.1$ in the AlO_x tunnel barrier [2]. In general, the methodology can serve as a tool to characterize the magnitude of Josephson harmonics and the homogeneity of tunnel barriers.

3.4 Impact on Transmon Charge Dispersion

The key design feature of the transmon is that it promises an exponential suppression of the charge dispersion at the cost of only a linear reduction of the anharmonicity (cf. Section 1.2.2, Fig. 1.1 and Ref. [60]). For this reason, the charge dispersion is a very sensitive additional probe of the model used for the Josephson potential on top of the average transition frequencies discussed so far. Evidently, it is highly relevant to discuss the consequences of Josephson harmonics on the transmon charge dispersion.

A comparison between experiment and model predictions is shown in Fig. 3.5a based on the Köln device, for which measurements of the maximum charge dispersion amplitude δf_{0j} of the first three levels $j = 1, 2, 3$ are available. The data has been taken for a sweep of the transmon transition frequencies by applying an in-plane magnetic field up to $B_\parallel = 0.4\,T$, which suppresses the Josephson energies of the junction (mainly due to the Fraunhofer-pattern suppression when flux penetrates the JJ [110, 195]). Strikingly, the charge dispersion predicted by the standard model (dashed gray line in Fig. 3.5a) underestimates the experimental data by a factor of 2 to 7. In comparison, the prediction
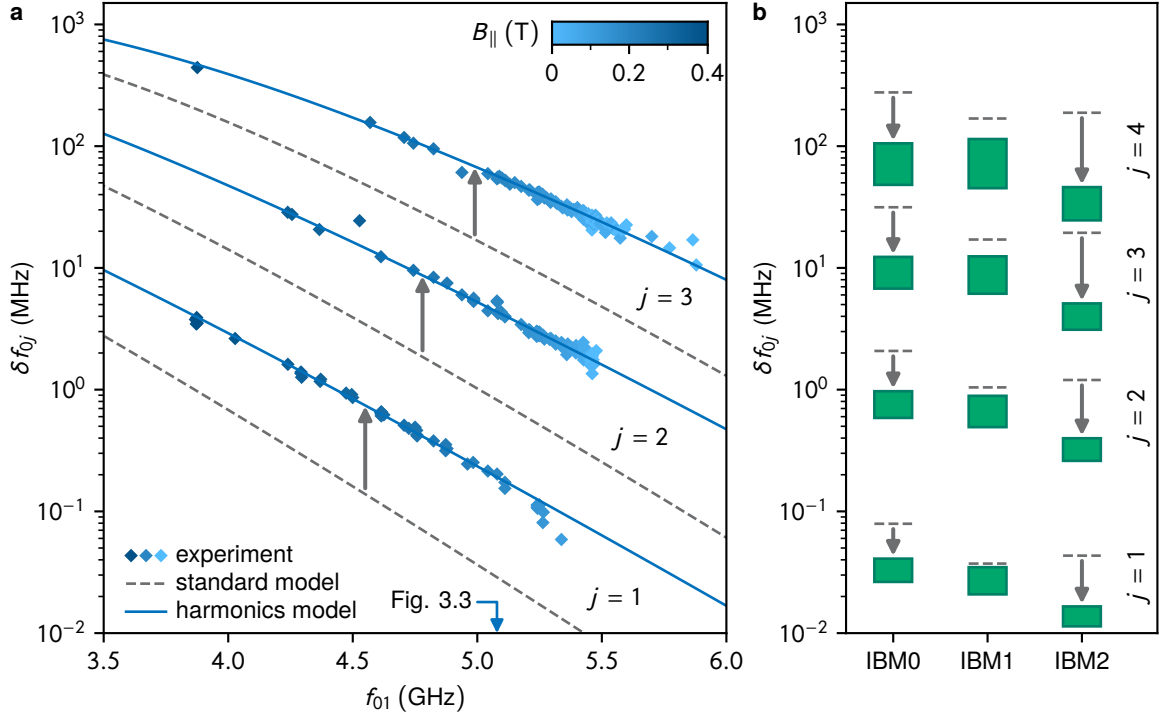
Figure 3.5: Impact of Josephson harmonics on transmon charge dispersion. **a** Underestimation of the charge dispersion δf_{0j} of levels $j = 1, 2, 3$ for the Köln transmon by the standard transmon model. Compared to the measured dispersion (blue markers) vs. first transition frequency f_{01}, the standard model prediction (grey dashed lines) is too low by a factor of 2 to 7, as highlighted by the gray arrows. In contrast, the Josephson harmonics model Eq. (3.11) (solid blue lines) matches the measured data. The transition frequencies are tuned by suppressing the Josephson energy up to 35 % with an in-plane magnetic field $B_\parallel$ indicated by the color scale. Both model predictions are calculated based on the same parameters used for the E_{J4} model shown in Fig. 3.3c including constant ratios E_{Jm}/E_{J1}, while only E_{J1} is varied to tune the frequency. The blue arrow at $f_{01} = 5.079$ GHz indicates the subset of the data used in Fig. 3.3. **b** Evidence for a reduction in charge dispersion by up to one order of magnitude (gray arrows) due to Josephson harmonics for IBM qubits 0, 1 and 2. Similar to panel a, the dashed gray lines indicate the standard model predictions. The green bars show the ranges of charge dispersion for levels $j = 1, 2, 3, 4$ corresponding to the ranges of E_{Jm}/E_{J1} shown in Fig. 3.4c. This figure is adapted from Fig. 4 in Ref. [2].

based on the Josephson harmonics model (solid blue lines) matches the data points. Notably, for both models the same parameters as in the standard model and E_{J4}-model shown in Fig. 3.3 are used. Only the first Josephson energy E_{J1} is varied to tune the transition frequencies, while in particular the relative ratios of Josephson harmonics E_{Jm}/E_{J1} are kept constant. This methodology confirms that the same set of relative harmonics can describe the measured spectroscopy and charge dispersion for different transition frequencies.

On the contrary, Josephson harmonics can also lead to a reduction in charge dispersion compared to the expectation of the standard model, as evidenced in Fig. 3.5b by the first three IBM qubits. Since detailed measurement of the charge dispersion are not available, we compare the prediction of the standard model (dashed gray lines) to the range of possible charge dispersion amplitudes based on the Josephson harmonics model (green bars), corresponding to the ranges of E_{Jm}/E_{J1} shown in Fig. 3.4c. The results show that the

charge dispersion for the qubit transition f_{01} can be a factor of 4 lower than expected from the standard transmon model.

The shortcomings of the standard transmon model in describing the charge dispersion are mainly due to a misjudgement of the ratio E_J/E_C when the model parameters are fixed based on the first two transition frequencies f_{01} and f_{02}. As a consequence of the exponential scaling, even moderate changes of E_J/E_C by percent are visible in an amplified way in the charge dispersion amplitudes. This is most visible for the IBM qubits, in which relatively strong contributions of the third harmonics (cf. Fig. 3.4c) lead to an effectively increased height of the Josephson potential in the harmonics model, which explains the significantly reduced charge dispersion prediction. In contrast, for the university transmons, the harmonics model corresponds to a smaller potential height and, consequently, incrased charge dispersion. Note that the correction in charge dispersion from Josephson harmonics compared to the standard transmon model are only on the order of 10 % when evaluated for the same E_J/E_C [2].

4 Conclusion & Outlook

Here, we summarize the results of the manuscript and outline perspectives for future work. With the two main results of the thesis in mind, we discuss the implications of our findings for grAl nano-junctions and mesoscopic tunnel junctions. In this thesis we have shown that the grAl nano-junction can serve as the tunnel JJ in a single-layer grAl fluxonium qubit with — besides conspicuous fluctuations of the Josephson energy — remarkably standard spectrum and coherence. This paves the way for using gralmonium devices or grAl nano-junction circuits in hybrid and other future applications. We have also observed measurable corrections to the presumed ideal $\sin \varphi$ nonlinearity in mesoscopic tunnel JJs based on transmon spectroscopy. Evaluating the consequences of Josephson harmonics for other devices based on tunnel JJs will be a relevant task for the field of superconducting circuits in general. This chapter is adapted in parts from the conclusion paragraphs of Refs. [1, 2].

Manuscript Summary

This manuscript started by introducing and motivating the appeal of hybrid architectures for quantum information processing based on superconducting circuits and spin qubits (electron spins, molecular magnets, etc.). By discussing the measurements of resonators in magnetic field similar to Ref. [4], we have confirmed that the high-kinetic-inductance superconductor granular alumimum (grAl) is a promising material to implement magnetic field resilient circuits for hybrid applications. In particular, the internal losses of grAl resonators remain resilient to magnetic field up to 1 T applied in-plane to the thin film. For fields perpendicular to the film, the sensitivity depends on the geometry of the resonators and is typically about 3 orders of magnitude stronger. An intriguing feature in the internal loss measurements versus magnetic field is the occurence of a prominent increase in losses at magnetic field values for which spins 1/2 with Landé factor of $g = 2$ are resonant with the mode. The precise origin of this spin 1/2 ensemble remains unclear, to date.

The first main result of the thesis is the implementation of a fluxonium-type superconducting quantum bit in a single layer of grAl: the gralmonium qubit [1]. As a key novelty, the tunnel junction of the gralmonium is given by a lithographically defined grAl volume on the order of $(20 \, \text{nm})^3$: the grAl nano-junction. Despite this unconventional circuit element, most measurements of the gralmonium are remarkably consistent with standard fluxonium expectations. In particular, the spectrum is reminiscent of conventional fluxonium spectra in the literature. Moreover, the energy relaxation and coherence times on the order of

$10\,\mu s$ are comparable to many superconducting devices. By analyzing the spectrum of the gralmonium in detail we have inferred that the current-phase relation (CφR) of the grAl nano-junction is indistinguishable from the purely $\sin\varphi$ Josephson CφR within the accuracy of the measurement. The upper bound for possible remaining contributions from higher Josephson harmonics can be set at $5\,\%$. However, fluctuations of the grAl nano-junction parameters influencing the spectrum of the gralmonium have been observed on timescales ranging from millisecond to days and most drastically after thermal cycling of samples.

The analysis of the grAl nano-junction CφR can be placed in context by answering the following question: how close are conventional Al-AlO$_x$-Al tunnel Josephson junctions to the idealized, purely sinusoidal CφR? In the second part of the manuscript, we have addressed this question based on spectroscopy of superconducting transmon qubits from several laboratories [2]. For the purpose of this analysis, transmons are advantageous because they are widely available in the community and have a simple circuit design such that alternative explanations for deviations in the spectroscopy can be ruled out by performing quantitative analysis. From a model of tunneling through an inhomogeneous AlO$_x$ barrier, we deduced the expectation of harmonic contributions in the percent range. Indeed, the measured spectroscopy data is consistent with the presence of percent-level harmonics across samples. The immediate consequence for transmon qubits is a changed sensitivity to offset-charge by up to an order of magnitude, as it is exponentially sensitive to the shape of the Josephson potential.

In summary, comparing Josephson harmonics in the grAl nano-junction and conventional Al-AlO$_x$-Al tunnel JJs, a surprising conclusion can be drawn: While the nano-junction CφR is compatible with a purely sinusoidal form within the accuracy of the measurement, the CφR of conventional tunnel JJs requires percent-level second harmonic contributions to be consistent with the measured spectroscopy across multiple samples. In this sense, the gralmonium and grAl nano-junction have remarkably standard properties and conventional tunnel JJs turn out to be less ideal than previously considered. Consequently, each of these results paves the way for a variety of future experiments which we discuss in more detail in the following.

Outlook on Granular Aluminum for Hybrid Applications

This work further cements granular aluminum as an interesting material platform for superconducting circuits in magnetic field. Even based on resonator measurements only, the combination of resilience and sensitivity allows to tailor grAl circuits to specific hybrid applications. The increased losses at magnetic fields corresponding to electron-spin resonance show that grAl intrinsically couples to a spin ensemble of unkown origin, which prompts follow-up experiments to understand the source of these spins and the coupling mechanism to grAl. Notably, these experiments can be relevant for superconducting circuits in general as the coupling to spin 1/2 impurities can be observed in various superconductors and on different substrates [115, 116, 133, 134]. Moreover, it could contribute to residual flux noise in superconducting circuits [196, 197] and even be linked

to the recent observation of a two-level system environment coupled to a grAl fluxonium qubit [7].

Expanding on the result of the grAl transmon qubit in Ref. [5], which has been measured in magnetic field up to ~ 100 mT, the gralmonium design fully incorporates the field resilience offered by thin film grAl. While the grAl transmon starts to be limited by the requirement for separate, pure aluminum shunting layers, the gralmonium as a single-layer grAl circuit can be expected to feature the same field-compatibility in the Tesla-range as measured for grAl resonators. Consequently, the gralmonium and similar circuits will be a promising tool for superconducting circuit measurements in relatively strong magnetic fields. One practical caveat for these experiments could be the out-of-plane sensitivity of the qubit spectrum to external flux bias due to the fluxonium loop. Although the gralmonium loop area is already relatively small thanks to a meandered design and the high resistivity grAl film, if required, the sensitivity can be further reduced by implementing a gradiometric loop design similar to Refs. [8, 198].

Perspective for the Gralmonium & GrAl Nano-Junction

With its promising first characterization in terms of spectroscopy and coherence, the gralmonium is a significant milestone for a circuit which is globally field resilient and locally sensitive to the small volume of the grAl nano-junction and its environment. Potentially, the energy relaxation and coherence times can be further improved by optimizing the design and fabrication of the gralmonium. Interestingly, the sensitivity to its tunnel junction parameters, integrated into the fluxonium-type circuit by design, is already visible in terms of fluctuations of the grAl nano-junction parameters influencing the gralmonium spectrum. Future experiments are required to rule out or identify possible candidates at the root of these fluctuations such as structural defects, charge-noise via Aharonov–Casher interference or paramagnetic impurities. Approaches to discriminate between these candidates could involve the application of a local electric field bias using a gate electrode, mechanical stress [199] or magnetic field. Moreover, possible routes to reduce the fluctuations could be cold substrate deposition, which results in smaller and more regular grains [122], or post processing of the film by hydrogen or laser annealing [200].

> *"In science, when you manage to answer one question you typically raise multiple new ones. And that's a success."*
>
> — A School Teacher

Apart from applications for hybrid quantum information hardware the grAl nano-junction itself is an interesting extension of the superconducting circuit toolbox. With its nanoscopic footprint, the nano-junction has an intrinsically small capacitance $C_J \lesssim 1$ fF by avoiding the parallel plate capacitance associated with typical mesoscopic tunnel JJs with dimensions in the $(100\,\mathrm{nm})^2$ range. This enables access to the parameter regime of $E_J/E_C \sim 1$ with $E_C/h \sim 10\text{--}100$ GHz, interesting for high-impedance circuits which rely on large quantum fluctuations of the phase [201, 202] and high-impedance metrological JJ applications [203].

Finally, the gralmonium coherence, comparable to conventional superconducting qubits, distinguishes the grAl nano-junction from constrictions embedded into qubits based on homogeneously disordered superconductors with orders of magnitude higher dissipation [204, 205], likely thanks to the chemical and structural similarity of grAl to Al-AlO$_x$-Al tunnel JJs.

Implications of Josephson Harmonics in Tunnel Junctions

In this work, we have observed Josephson harmonics in tunnel junctions based on transmon spectroscopy, with immediate consequences for the design and measurements of transmon qubits and processors. Most notably, as a consequence of Josephson harmonics, transmon dephasing due to charge noise can be reduced by an order of magnitude without further lowering the circuits anharmonicity. This paves the way for a possible optimization route, in which Josephson harmonics are engineered to optimize the spectrum for reduced charge dispersion and increased anharmonicity. Approaches to turn this idea into reality include shaping the channel transparencies directly or utilizing networks of high transparency JJs to implement arbitrarily tailored CφRs as outlined recently in Ref. [206].

Importantly, the consequences of harmonics in the CφR of tunnel junctions probably go beyond the observation in transmon qubits presented here. Consequently, they trigger a reevaluation of current models for many devices based on tunnel JJs in quantum technology and metrology [186, 207–210]. Specifically, it will be of interest to understand the implications of Josephson harmonics in other superconducting artificial atoms, for gates and computation schemes relying on higher levels [211–214], quantum-non-demolition readout fidelities [9, 96, 97], and frequency crowding mitigation in quantum processors [200]. Moreover, Josephson harmonics will probably have to be considered in topological JJ circuits [202, 215, 216], in pumping schemes for parametric amplification and bosonic codes [217, 218], in JJ metrological devices [219–222], and they can be utilized to realize Josephson diodes [223]. In conclusion, as measurements and models of superconducting circuits progress towards ever-decreasing error margins, Josephson harmonics will need to be embraced both in material science to optimize tunnel barriers and in circuit design as an integral part of the device physics.

Part II

Detailed Information

A Cylindrical Waveguide Sample Holder

Two common sample holder schemes to measure superconducting circuits are 3D waveguides or cavities, and 2D on-chip geometries. 3D cQED architectures have the advantage that the electric field coupling to the circuit can be diluted in order to minimize the energy participation ratio of dielectric losses [156, 224, 225]. Moreover, they do not require an on-chip ground plane as the waveguide itself serves as the ground for the electric field. Ideally, the waveguide volume represents a clean vacuum environment, especially important in the vicinity of the device, while coupling polarized microwave signals to the sample. In contrast, 2D on-chip layouts and environments for superconducting circuits have to be carefully engineered in order to avoid parasitic modes and impedance mismatches. However, in order to lower the cut-off frequency of 3D waveguides to the operating frequencies of superconducting circuits in the $\lesssim 10\,\mathrm{GHz}$ range, the dimensions of the waveguide are typically on the order of few centimeters [226].

For the measurements of the grAl resonators in magnetic field (cf. Section 1.4 and Ref. [4]) and the gralmonium (Chapter 2), we employ a sub-wavelength cylindrical copper waveguide sample holder as illustrated in Fig. A.1 with schematics and finite-element simulations. The main feature of the sample holder is the small transverse size of the copper tube with inner diameter of 3 mm and a wall thickness of only 0.3 mm. As a consequence, we expect a cut-off frequency of the waveguide on the order of $\sim 60\,\mathrm{GHz}$ [226] and the conventional standing-wave pattern coupling in the frequency band of the waveguide cannot be utilized.

Instead, in our sub-wavelength sample holder, the circuit is coupled directly to the evanescent microwave field of a stripped coaxial pin (cf. panels a-c of Fig. A.1). In this regime, the coupling is expected to decay exponentially with respect to the distance between sample and pin (and also with decreasing microwave frequency). Indeed, a finite-element simulation of the coupling to a stripline grAl resonator antenna (Fig. A.1d,e) confirms the expected scaling with distance in the regime of coupling quality factors Q_c between 10^4 and 10^6. On the one hand, this sensitivity to the chip-pin distance can be a source of inconvenience when aiming for a precise coupling strength. On the other hand, it can be utilized to increase or decrease the coupling to fabricated circuits between cooldowns, simply by adjusting the sample holder to the desired distance (see Ref. [3]).

The sample holder is anchored to the mixing chamber stage of a Sionludi dilution cryostat for experiments involving Tesla-range magnetic field or, alternatively, in a Bluefors dilution cryostat for standard microwave characterizations. Thanks to its small diameter, for the field measurements the sample holder can be used in combination with a compact 3D vector magnet anchored at the 4 K-stage of the cryostat as shown in Fig. A.2 (and utilized
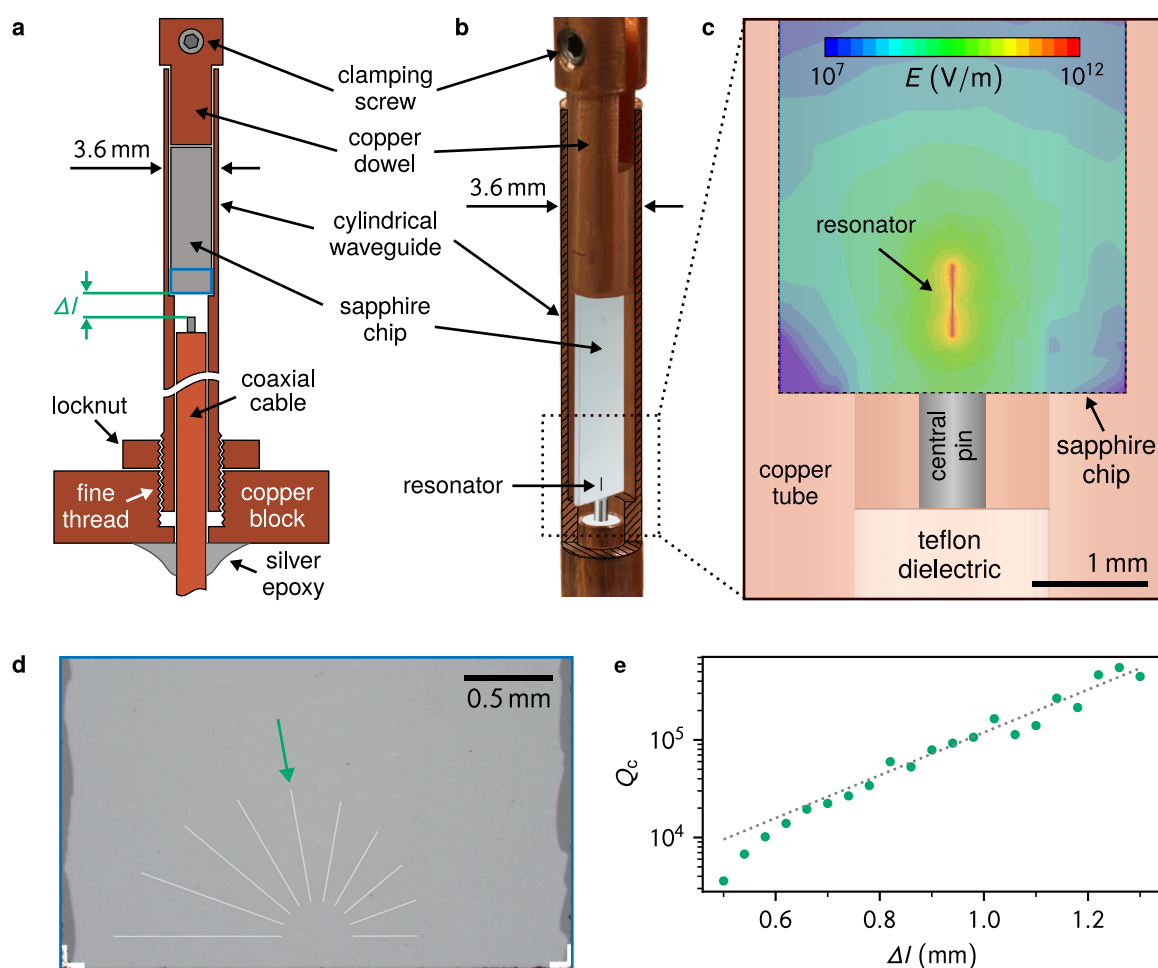
Figure A.1: Schematics and simulations of cylindrical waveguide sample holder. **a,b** Cross-section schematics and artistic image composition of the cylindrical copper waveguide. By tightening the clamping screw of a copper dowel against the copper tube wall, the sample is fixed inside the waveguide. The circuits on the chip are coupled to the evanescent field of the stripped coaxial cable pin, since typical operating frequencies ($\sim$ 4–10 GHz) are well below the cut-off frequency of the waveguide ($\sim$ 60 GHz) [226]. The coupling strength can be adjusted by unscrewing the copper tube relative to the fixed coaxial cable, i.e. by changing the chip-pin distance Δl (cf. green arrows and panel e). **c** Color plot of the electric field distribution based on finite-element simulation. The electric field amplitude indicated by the color scale corresponds to an energy of 1 J in the simulation. **d** Optical image of a sample with 10 stripline resonators with lengths between 400 µm and 950 µm and arranged in a radial geometry to couple to the coaxial pin. The image corresponds to the region of the chip indicated by the blue rectangle in panel a. **e** Coupling quality factor Q_c for the resonator indicated by the green arrow in panel d extracted by finite-element simulation depending on the chip-pin distance Δl (cf. green arrows in panel a). Q_c changes exponentially (dotted gray line) with Δl by one order of magnitude for one pitch of the sample holder fine thread (cf. panel a), which corresponds to 0.5 mm. This figure is adapted from Fig. 7 of Ref. [3] and Fig. S1 of Ref. [1].

in Refs. [3, 4]). This setup has the advantage that heating effects on the mixing chamber stage due to ramping the Ampere-range currents for the magnetic field are avoided by the relatively large cooling power offered by the 4 K-stage. Note that for measurements involving the vector magnet, we do not include additional (e.g. infrared or magnetic) shielding between the cylindrical sample holder and the coils of the vector magnet.
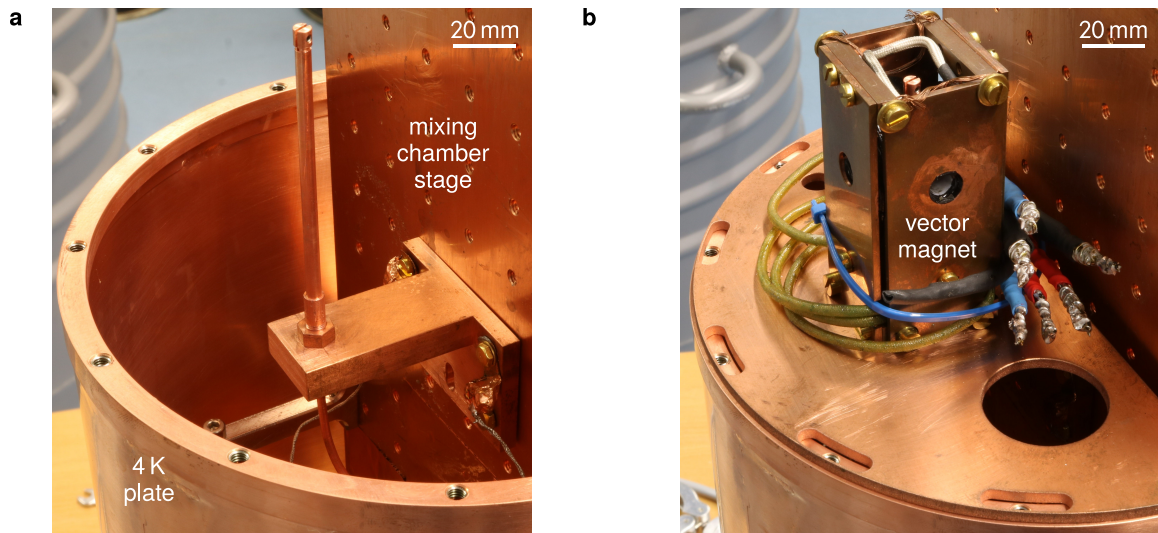
Figure A.2: Pictures of the sample holder and vector magnet. **a** The sample holder anchored to the mixing chamber stage (vertical copper plate) of a Sionludi dilution cryostat. **b** Thanks to its small dimensions, the copper tube can be surrounded by a compact 3D vector magnet anchored at the 4 K-stage of the cryostat.

B Details on the Gralmonium

This chapter is adapted from the supplementary material of Ref. [1].

B.1 Fabrication Recipe

Here we summarize the fabrication recipe of the gralmonium samples discussed in the manuscript (cf. Table B.1). The samples are fabricated on c-plane, double-side polished sapphire substrates using lift-off e-beam lithography. The resist stack consists of 700–800 nm MMA EL-13 and 300 nm PMMA A4. A 10 nm chromium anti-static layer is evaporated before exposing the samples with a 100 keV e-beam writer. After etching the chromium layer, an MIBK-isopropanol mixture (volume ratio 1:3) is used for spray development of the samples. Before the metal deposition in a PreVac evaporation system, the substrate is cleaned with a Kaufmann ion source in an Ar/O_2 descum process similar to Ref. [227] and the vacuum is improved using titanium gettering. The 20 nm thick granular aluminum film is deposited under zero angle, at room temperature and a deposition rate around $\approx 1\,\mathrm{nm/s}$ in a dynamic oxygen atmosphere resulting in a chamber pressure of $10^{-5} - 10^{-4}$ mbar. The resulting sheet resistance for the main text sample is $1.5\,\mathrm{k\Omega/\square}$.

Step	Description	Details
Substrate	c-plane sapphire	thickness 330 μm double-side polished
Cleaning	Ar/O_2 descum	
Bottom resist	MMA EL-13	thickness $\sim$ 700–800 nm
Top resist	PMMA A4	thickness $\sim$ 300 nm
Anti-static	Cr at rate 0.1 nm	thickness $\sim$ 10 nm
Exposure	100 keV e-beam writer	
Chromium etch	10 s	
Development	MIBK-isopropanol 1:3	spray developer
Gettering	Ti at rate 0.2 nm/s for 2 min	shutter closed
E-beam evaporation	Al at rate $\sim$ 1 nm/s	thickness $\sim$ 20 nm O_2 pressure 10^{-5}–10^{-4} mbar
Lift-Off	Acetone, ethanol rinse	

Table B.1: Gralmonium fabrication recipe. Overview of fabrication steps for the single-layer, zero-angle gralmonium recipe as explained in the main text.
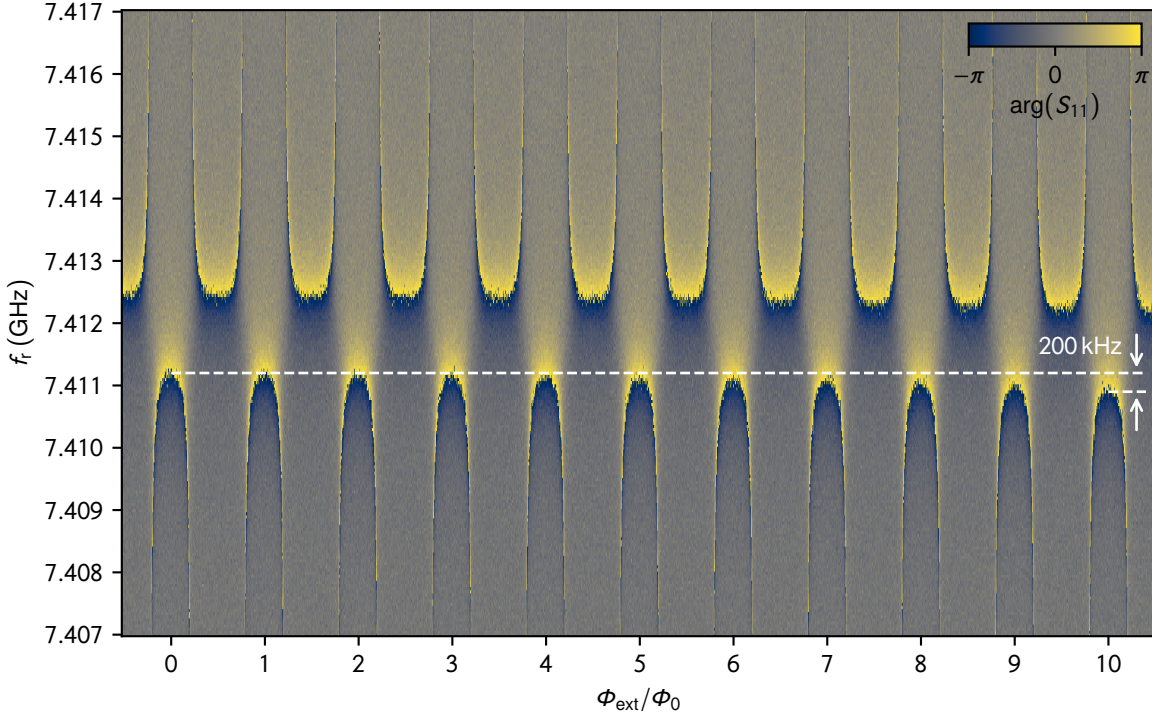
Figure B.1: Periodic avoided level crossings between gralmonium and resonator. Flux sweep of the readout resonator extending up to $\Phi_{\text{ext}}/\Phi_0 = 10$. The avoided level-crossings repeat periodically and are superimposed by a $\approx 200\,\text{kHz}$ frequency shift across the entire sweep (indicated by the white arrows and horizontal lines) due to screening currents in the antenna (cf. Eq. (1.13) in Section 1.4). The resonance frequency is 2.5 MHz higher compared to the main text measurement (Fig. 2.4a), since the data shown here was taken in a previous cooldown.

B.2 Flux Periodicity

As outlined in Section 2.1.2 and shown in Fig. 2.4a, the signature of gralmonium devices coupled to the readout resonator and operating in the target frequency range ($\sim 4\text{–}10\,\text{GHz}$) are periodic qubit-resonator avoided level-crossings vs. external flux. In Fig. B.1 we show an extended flux sweep of the main text device in another cooldown up to $\Phi_{\text{ext}}/\Phi_0 \geq 10$, revealing the strict periodicity of the avoided level-crossings. A frequency shift of 200 kHz is accumulated across the entire flux sweep range, as expected from the out-of-plane magnetic field dependence of the $4\,\mu\text{m}$ wide grAl stripline (cf. Fig. 1.3 in Section 1.4 and Ref. [4]).

Since the E_J/E_C ratio for the grAl nano-junction is highly sensitive to its width (cf. Section 2.2), very different spectra can occur even for devices with nominally identical fabrication, in particular due to lithography variability. In the following we detail how measuring the out-of-plane magnetic field dependence is an efficient method to select devices of interest. In Fig. B.2 we compare three devices with nominally identical design for the gralmonium and nano-junction, fabricated in the same evaporation on the same chip and measured in the same cooldown. While the first device (Fig. B.2a) shows no qubit-resonator avoided level-crossings, the resonator frequency shifts down by 1 MHz in the measured
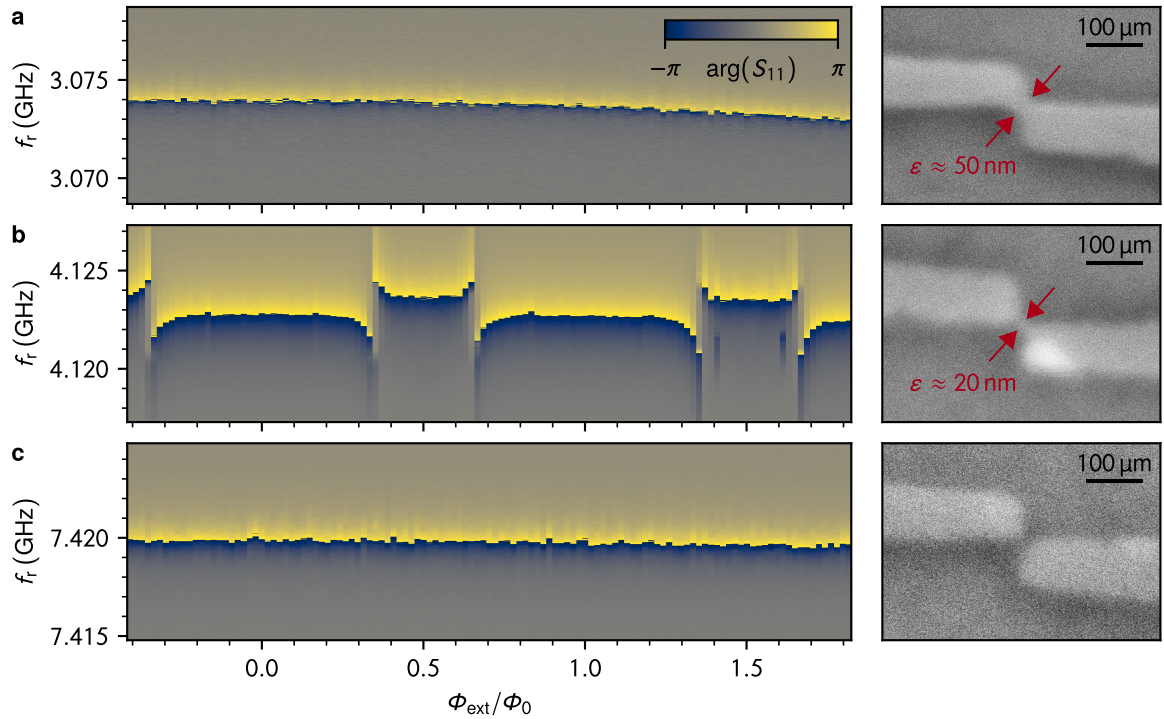
Figure B.2: GrAl nano-junction regimes. The panels in the left column show flux sweeps of the reflection coefficient for three different samples with nominally identical gralmonium and nano-junction design (cf. Fig. 2.2). The right column depicts an SEM image of each grAl nano-junction corresponding to the sample shown in the flux sweep and taken after the cooldown. **a** Flux sweep without avoided level-crossings and slightly decreasing resonator frequency with increasing external flux. These observations can be attributed to the too wide nano-junction ($\varepsilon \approx 50\,\text{nm}$) and resulting screening currents in the loop. **b** Flux sweep with periodic avoided level-crossings indicating a functioning gralmonium attached to the resonator, similar to the measurement shown in the main text Fig. 2.4a. The grAl nano-junction width is in the same regime of $\varepsilon \approx 20\,\text{nm}$ as the main sample (Fig. 2.3d). **c** Constant resonator frequency due to an interrupted nano-junction. Note that the remaining contribution due to screening currents in the resonator is neglibile in this field range (cf. Fig. B.1 in comparison).

field range. The absence of crossings can be explained by a ratio $E_\text{J}/E_\text{C} \gg 1$ for this nano-junction such that quantum fluctuations of the phase are suppressed (cf. Eq. (1.10)). In this regime, the external flux applied to the sample induces circulating currents in the fluxonium loop, leading to the 1 MHz frequency shift — a much larger field dependence than expected from the out-of-plane shift of the bare grAl antenna (see Fig. B.1 in comparison). Indeed, the SEM image of the nano-junction, taken after the cooldown of the device, confirms a relatively large width $\varepsilon \approx 50\,\text{nm}$. In contrast, the flux sweep shown in Fig. B.2b features qubit-resonator avoided level crossings similar to the main text sample (Fig. 2.4a), and the corresponding SEM image indicates a grAl nano-junction width on the order of 20 nm. For an interrupted nano-junction, as shown in Fig. B.2c, no visible resonator frequency shift occurs in the measured flux range, consistent with the expectation for the out-of-plane field dependence (cf. Fig. B.1 and Section 1.4).

Based on the evidence presented in Fig. B.2 and the SEM images of 53 devices (histogrammed in Fig. 2.2c in the main text), we find that 22% of nano-junctions are in
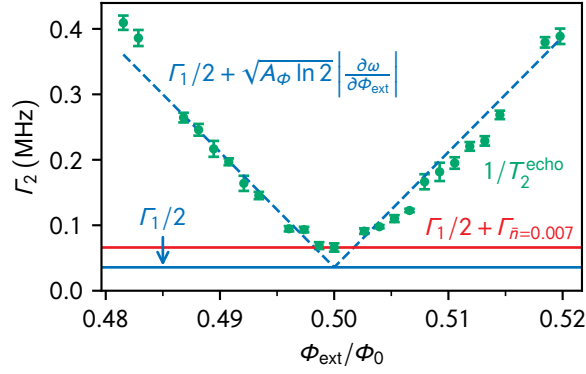
Figure B.3: Gralmonium decoherence budget analysis around half-flux. The green markers represent the echo decoherence rate $\Gamma_2^{\text{echo}} = 1/T_2^{\text{echo}}$ calculated from the Hahn echo data vs. external flux shown in Fig. 2.5c in the main text. The blue horizontal line indicates the contribution from energy relaxation, $\Gamma_1/2$. By fitting the linear increase of Γ_2^{echo}, we extract a flux noise amplitude of $A_\Phi = 30\,\mu\Phi_0$ (dashed blue lines). Among other reasons, the residual decoherence exactly at half-flux can be explained by shot noise corresponding to an average thermal population of $\bar{n} \approx 0.007$ in the readout resonator (red horizontal line).

the target regime for the width corresponding to connected junctions with $\varepsilon \leq 25\,\text{nm}$. Likely, this percentage can be further improved by using thinner resist layers and by using aluminum instead of chromium for the anti-static coating (cf. Appendix B.1) to reduce the edge roughness of the written pattern. Moreover, owing to the single-layer circuit design, etching is an appealing alternative to lift-off fabrication for the gralmonium and nano-junction, with the possibility to use sub 10 nm resolution negative e-beam resists. Beyond improving the reliability of lithography and fabrication, post-processing samples with wet-etching or annealing can bring nano-junctions closer to a desired E_J regime. Finally, even nano-junctions similar to Fig. B.2a may lead to working gralmonium devices for sufficiently large grAl sheet resistivity below the superconductor-to-insulator transition.

B.3 Decoherence Budget at Half-Flux

In the following, we analyze the decoherence of the main gralmonium sample around half-flux bias based on the T_2^{echo} data of Fig. 2.5c in the main text. Fig. B.3 shows the corresponding decoherence rate $\Gamma_2^{\text{echo}} = 1/T_2^{\text{echo}}$ (green markers). The main contributions to the decoherence rate are energy relaxation $\Gamma_1/2$, flux noise $\Gamma_\Phi(\Phi_{\text{ext}})$, photon shot noise due to stray photons in the resonator $\Gamma_{\bar{n}}$, and critical current noise in the nano-junction and superinductor Γ_{I_c}:

$$\Gamma_2^{\text{echo}} = \frac{\Gamma_1}{2} + \Gamma_\Phi(\Phi_{\text{ext}}) + \Gamma_{\bar{n}} + \Gamma_{I_\text{c}} \,. \tag{B.1}$$

From the data in Fig. 2.5c, we conclude that energy relaxation vs. external flux is flat in the measured flux range with an average $T_1 = \Gamma_1^{-1} = 14\,\mu\text{s}$. The associated constant contribution $\Gamma_1/2$ is indicated in Fig. B.3 by the horizontal blue line. Around half-flux bias, a linear increase of Γ_2^{echo} can be observed (dashed blue lines) and the slope corresponds to a $1/f$ flux noise amplitude of $A_\Phi = 30\,\mu\Phi_0$. Note that an additional, flux-dependent Gaussian
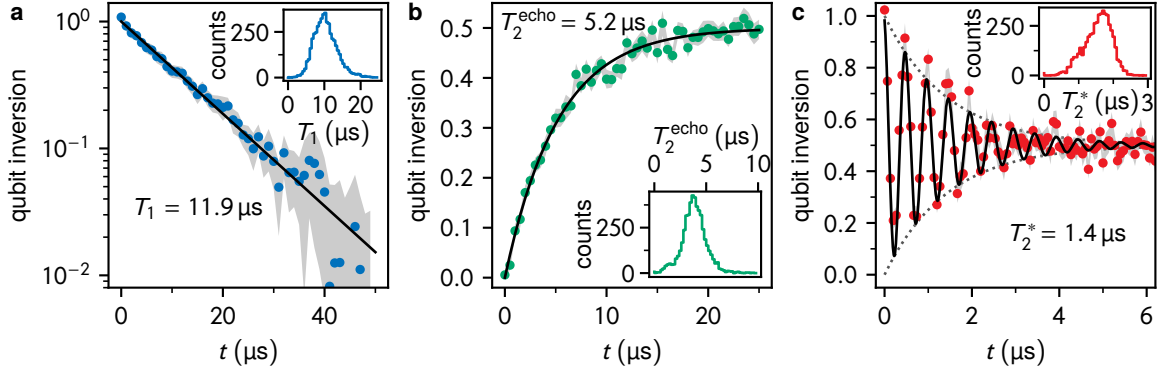
Figure B.4: Gralmonium time domain characterization at zero-flux. a Example of a free decay energy relaxation and **b** spin Hahn echo measurement. The black lines are exponential fits corresponding to $T_1 = 11.9\,\mu s$ and $T_2^{echo} = 5.2\,\mu s$, respectively. The average T_1 is comparable to half-flux, while T_2^{echo} is a factor of 2 lower (cf. Fig. 2.5). **c** Example of a Ramsey fringes measurement with nominal detuning of 2 MHz. In contrast to half-flux bias (cf. Fig. 2.6), we do not observe a beating of the fringes at zero-flux, and the fit (black line) corresponds to a single sinusoidal with exponential envelope (dotted gray lines).

component in the echo decay curves cannot be excluded due to the limited resolution and SNR of the measurements. For this reason, we use an exponential decay to fit the entire data set vs. flux consistently.

Even exactly at half-flux bias, $\Phi_{ext}/\Phi_0 = 0.5$, where the spectrum is first-order insensitive to external flux ($\partial\omega/\partial\Phi_{ext} = 0$), the value of Γ_2^{echo} is a factor of 2 larger than the possible T_1-limit $\Gamma_1/2$. Reasons for the residual dephasing could be either higher-order flux noise contributions or photon shot noise. Given the dephasing rate due to photon shot noise in the low-photon limit, [228, 229]

$$\Gamma_{\bar{n}} = \frac{\bar{n}\kappa\chi^2}{\kappa^2 + \chi^2}\,, \tag{B.2}$$

and the independently measured values of χ and κ (cf. Fig. B.6 in Appendix B.5), an average population of $\bar{n} \approx 0.007$ in the resonator would explain the residual dephasing rate. Note that the estimated value is consistent with typical values observed in the literature (see e.g. [229]). Finally, the echo sequence can efficiently filter the critical current noise, which likely explains the factor of 3 increased T_2^{echo} compared to the Ramsey decay time T_2^* at half-flux (cf. Fig. 2.6). This is due to the echo sequence filtering noise on timescales between 10 μs (given by the filter function cut-off) and ms (the timescale already captured by the two frequency sinusoidal fit for the Ramsey measurement).

B.4 Zero-Flux Coherence

Fig. B.4 shows standard energy relaxation and coherence measurements of the $|g\rangle \rightarrow |e\rangle$ transition performed at zero-flux bias similar to Fig. 2.5 at half-flux bias in the main text. The transition is not plasmon-like in the gralmonium device, as illustrated by the
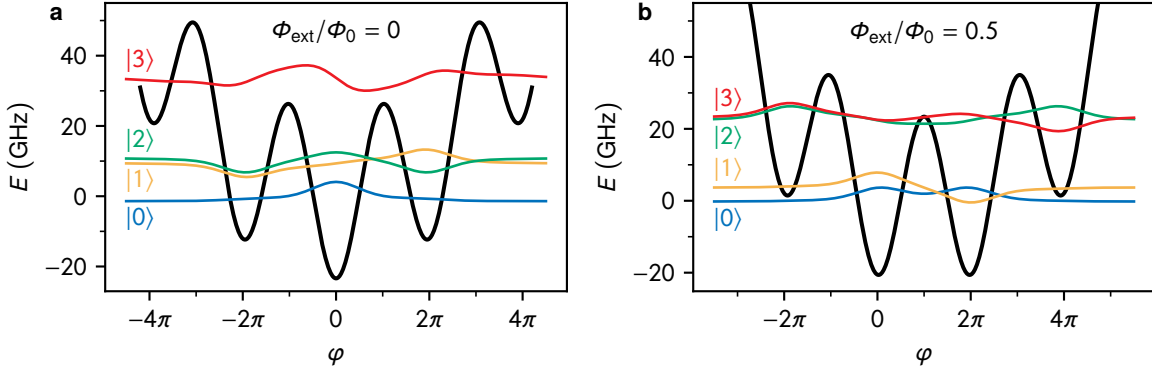
Figure B.5: Gralmonium potential energy landscape and wavefunctions. The black line represents the energy potential and the colored lines correspond to the real part of the first four wavefunctions offset by their eigenenergies. Both are calculated for the gralmonium parameters given in Table 2.1 in the main text. **a** At zero-flux bias, $\Phi_{\text{ext}} = 0$, all wavefunctions are significantly delocalized over three potential wells. As a consequence, the $|g\rangle \to |e\rangle$ transition is not plasmon-like as typically the case for fluxoniums with larger E_{L} (corresponding to less inductance in the loop). **b** At half-flux bias $\Phi_{\text{ext}}/\Phi_0 = 0.5$, the first transition frequency is determined predominantly by tunneling through the double-well barrier, similar to Fig. 1.1e in the introduction.

energy potential and wavefunctions in Fig. B.5a. Moreover, in contrast to measurements at half-flux, the Ramsey fringes (Fig. B.4c) can be fit with a single sinusoidal.

B.5 Quantum Jumps Analysis

Here we discuss the single-shot dispersive readout of the gralmonium enabled by the near quantum-limited DJJAA parametric amplifier [6] in the readout chain (cf. Fig. 2.3e). Fig. B.6a shows a histogram of the readout resonator reflection coefficient S_{11} based on 50 repetitions of 10 ms long readout tones, each sliced into 784 ns long contiguous sections. The histogram is measured at a readout frequency of $f_{\text{r}} = 7.4086\,\text{GHz}$ and readout power of $\bar{n} \approx 10$ circulating photons in the resonator. Based on the steady-state populations of the ground state $|g\rangle$ and first excited state $|e\rangle$, we find an effective qubit temperature of $T_{\text{q}} \approx 37\,\text{mK}$. As shown in Fig. B.6b, by measuring the IQ histograms for various readout frequencies, we determine the dressed resonator responses for the qubit being in $|g\rangle$ and $|e\rangle$, which are separated by the dispersive shift $\chi/2\pi = -1.72\,\text{MHz}$ (cf. Section 1.2.3). Note that readout with maximum phase separation of $180°$ is available due to the regime of $|\chi| > \kappa$. As a consequence, the average reflection coefficient can reach a value of $|S_{11}| = 0$ in two-tone spectroscopy measurements (see e.g. Fig. 2.4b in the main text).

While Fig. B.6 is based on histograms of single-shot readout measurements, we analyze the same data as a function of time in Fig. B.7. The analysis is based on the same contiguous reflection coefficient data as histogrammed in Fig. B.6a. In order to encode the qubit state information in the in-phase quadrature I, we rotate the IQ plane to align the states with the I axis. Consequently, the means $\mu_{\text{g,e}} \approx \pm 3.0\,\sqrt{\text{photon}}$ and standard deviations $\sigma_{\text{g,e}} \approx 1.0\,\sqrt{\text{photon}}$ for the qubit states can be extracted from a double gaussian fit to the
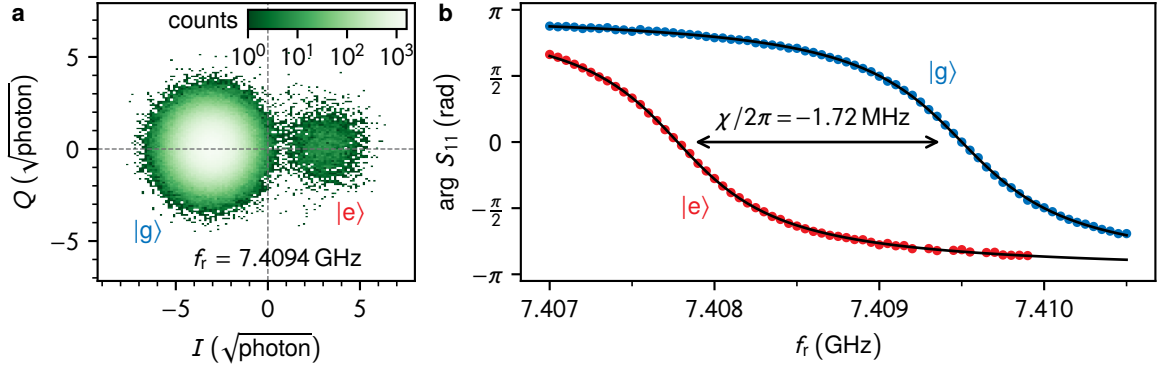
Figure B.6: Dispersive readout of the gralmonium. **a** Histogram of contiguous reflection coefficient measurements in the complex plane at half-flux bias $\Phi_{\text{ext}}/\Phi_0 = 0.5$ and a readout frequency of $f_r = 7.4086$ GHz. The points are integrated for 784 ns and measured at a readout power of $\bar{n} \approx 10$ circulating photons in the readout resonator. The ground state $|g\rangle$ and first excited state $|e\rangle$ are visible and their populations correspond to an effective qubit temperature of 37 mK. **b** Resonator phase responses for the qubit in the ground state $|g\rangle$ (blue) and excited state $|e\rangle$ (red). The values are extracted based on IQ histograms taken vs. readout frequency f_r similar to the one shown in panel a but with a $\pi/2$ qubit pulse applied before the readout pulse, in order to balance the visibility of the two states. From fits to the phase responses (black lines), we find a dispersive shift of $\chi/2\pi = -1.72$ MHz between the dressed resonator states and a resonator linewidth of $\kappa/2\pi = 1.00$ MHz.
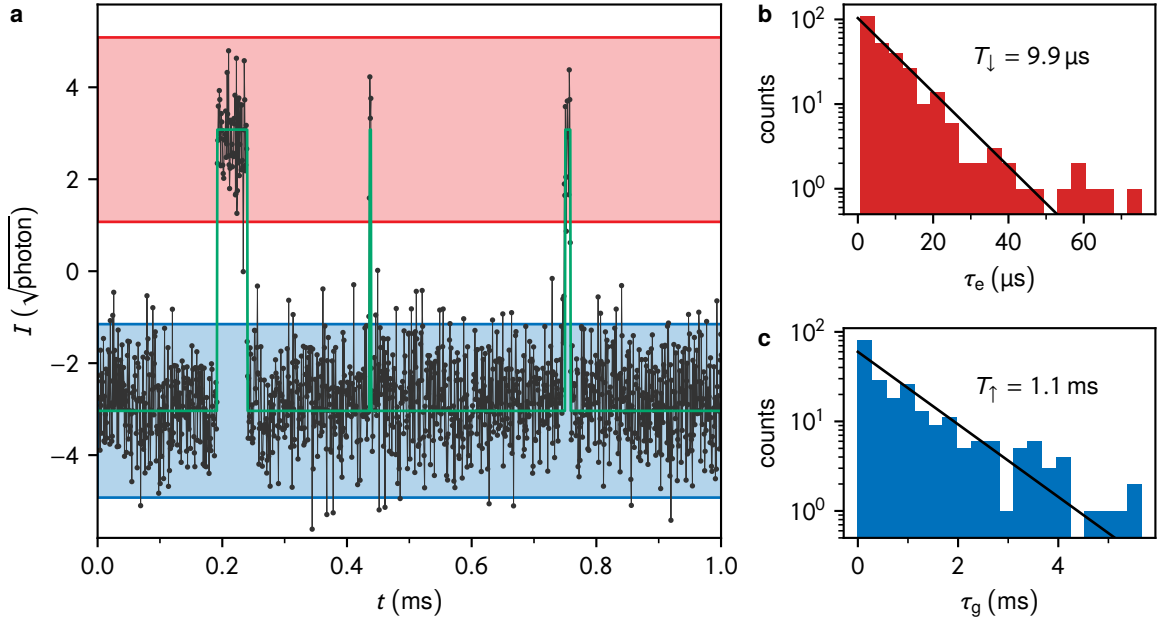
Figure B.7: Gralmonium quantum jumps analysis. **a** Example time trace of contiguous readout resonator reflection coefficient measurements (connected black markers). The data corresponds to the points histogrammed in Fig. B.6a and we plot the in-phase quadrature I, which encodes the qubit state information. The trace is measured at a readout power of $\bar{n} \approx 10$ circulating photons and demodulated in windows of 784 ns. A latching filter is used to assign the qubit state (green line) based on the $\pm 2\sigma$ bands (shaded in blue and red for $|g\rangle$ and $|e\rangle$, respectively) around the mean values of the qubit states. Panels **b** and **c** show histograms of the dwell times τ_e and τ_g spent by the qubit in the excited and ground state, respectively. From maximum-likelihood exponential fits we extract the average qubit relaxation time $T_\downarrow = 9.9\,\mu s$ and excitation time $T_\uparrow = 1.1$ ms.
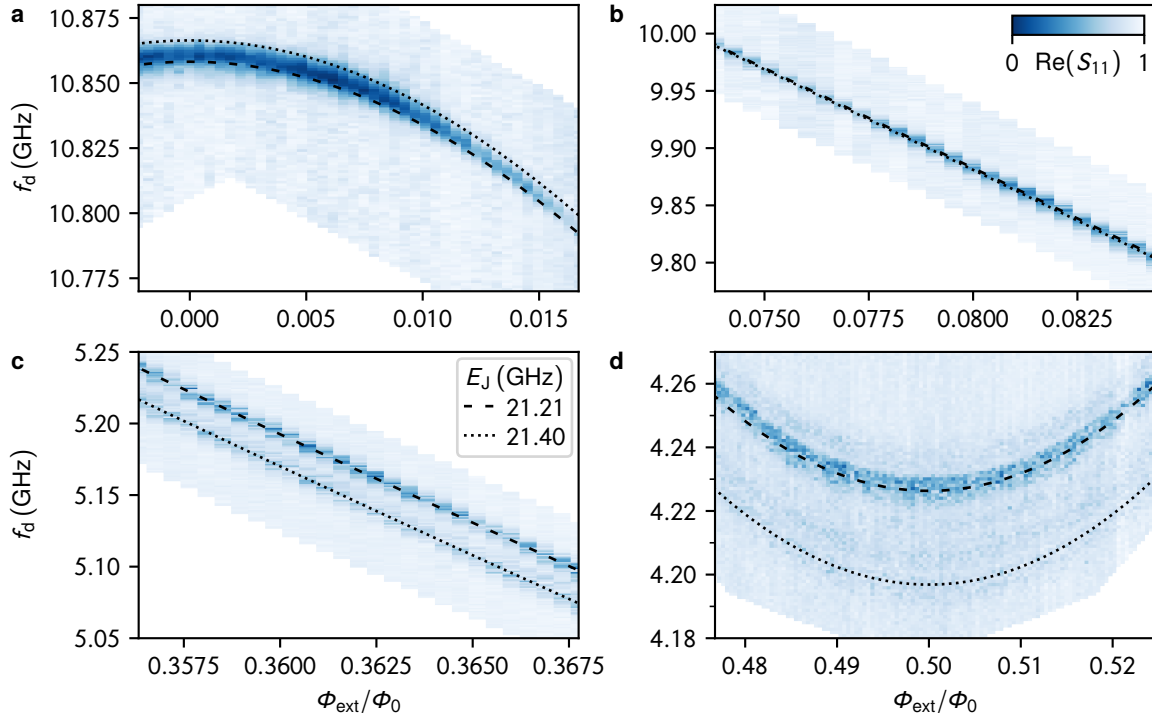
Figure B.8: Evidence of Josephson energy toggling in gralmonium spectrum. The spectroscopy shown in this figure is measured on the main gralmonium sample (cf. Fig. 2.4) but in a preceding cooldown (#3 in Fig. B.9) without using a parametric amplifier. Each vertical trace contains 100 points which, in total, are averaged over 50 s. The color scale corresponds to the in-phase component of the single-port reflection coefficient S_{11}, with the minimum and maximum values rescaled to the $0 - 1$ interval. Notably, across the entire flux range, two dominant qubit frequencies are visible and their spectrum vs. external flux can be fitted (dashed and dotted black line) with identical circuit parameters except for the nano-junction Josephson energy E_J differing by 190 MHz. The splitting between the two spectra is 7.4 MHz close to zero-flux (panel **a**). Notably, as expected from the two-E_J model, the lines merge and cross at $\Phi_{ext}/\Phi_0 \approx 0.08$ (panel **b**) and they are separated by more than 10 MHz towards half-flux (panel **c**). At half-flux (panel **d**), the largest splitting (30 MHz) occurs and additional lines become visible.

marginal distribution along the I quadrature. We use a two-point latching filter to assign the qubit state $|g\rangle$ or $|e\rangle$ to each contiguous point; a change in qubit state is declared when the in-phase value I enters the $\mu \pm 2\sigma$ band (shaded regions in Fig. B.7a) centered on the other qubit state. Fig. B.7b,c show histograms of the dwell times in each qubit state. Based on exponential fits to the data, we calculate an energy relaxation during readout of $T_1 = (T_{\downarrow}^{-1} + T_{\uparrow}^{-1})^{-1} = 9.8\,\mu s$. Notably, this value is consistent with the range extracted from free decay energy relaxation measurements (Fig. 2.5a).

B.6 Evidence of E$_J$-Toggling in Spectroscopy

The gralmonium half-flux frequency changes even when the sample is kept at cryogenic temperatures, as discussed in the main text Section 2.3.3 and Fig. 2.6. If the trace averaging time is on the order of the respective toggling timescale, the frequency fluctuations are

also visible in continuous wave spectroscopy vs. external flux. For example, in the half-flux spectroscopy shown in the main text (Fig. 2.4b, bottom right inset), jumps in the qubit frequency occurring every few traces evidence a toggling on minutes timescale.

The panels of Fig. B.8 show spectroscopy data taken for the main gralmonium sample in a previous cooldown without a parametric amplifier. As a consequence, the averaging time per trace is about one order of magnitude longer and the toggling on minutes timescale is imprinted on the spectroscopy data as distinct lines corresponding to the different qubit transition frequencies. In Fig. B.8 the different qubit frequencies are visible within the same trace, in contrast to the jumps occurring between traces in Fig. 2.4b. Notably, transverse coupling to parasitic two-level systems residing at fixed frequency is ruled out as the origin of these fluctuations based on the observation of two qubit frequencies across the entire flux range of the spectroscopy. Instead, the two qubit spectra can be described by two fits to the fluxonium Hamiltonian Eq. (2.2), only differing in the value of the nano-junction Josephson energy E_J. In particular, both the merging of the two spectra at $\Phi_{\text{ext}}/\Phi_0 \approx 0.08$ (Fig. B.8b) and their frequency inversion between zero-flux (panel a) and half-flux bias (panel d) are predicted by the two-E_J model.

B.7 Additional Gralmonium Spectra

In this section, we discuss gralmonium spectra vs. external flux beyond the data shown in Fig. 2.4b in the main text. The set of spectra in Fig. B.9 is based on the main sample measured in 6 successive cooldowns. A comparison of the panels (plotted with identical vertical scale) highlights significant changes in the spectra, especially regarding the half-flux frequency. Based on the fits (black lines) to Hamiltonian Eq. (2.2), the nano-junction Josephson energy E_J can be identified as the parameter with the strongest changes between measurements, as indicated in Fig. 2.6d in the main text. Although the total gralmonium capacitance $C_\Sigma = C_q + C_J$ also changes (apparently correlated in direction and strength with E_J), its minimal value is bounded by the interdigitated capacitance $C_q \approx 0.8\,\text{fF}$ (corresponding to a maximum charging energy of $E_C^\Sigma \leq E_C^q \approx 24\,\text{GHz}$). The source of this apparent correlation is not currently identified and more work is needed in order to elucidate the underlying mechanism.

In total, we measured the spectra of 20 gralmonium devices across 11 wafers and find that all data is consistent with the standard fluxonium Hamiltonian Eq. (2.2). The spectra and fit parameters of three devices with the same circuit design as the main sample (cf. Fig. 2.3) are shown in Fig. B.10. Notably, the spread of the Josephson energy across devices, 7–40 GHz, is of the same order as the variations of individual nano-junctions in successive cooldowns, 8–27 GHz (cf. Fig. B.9).
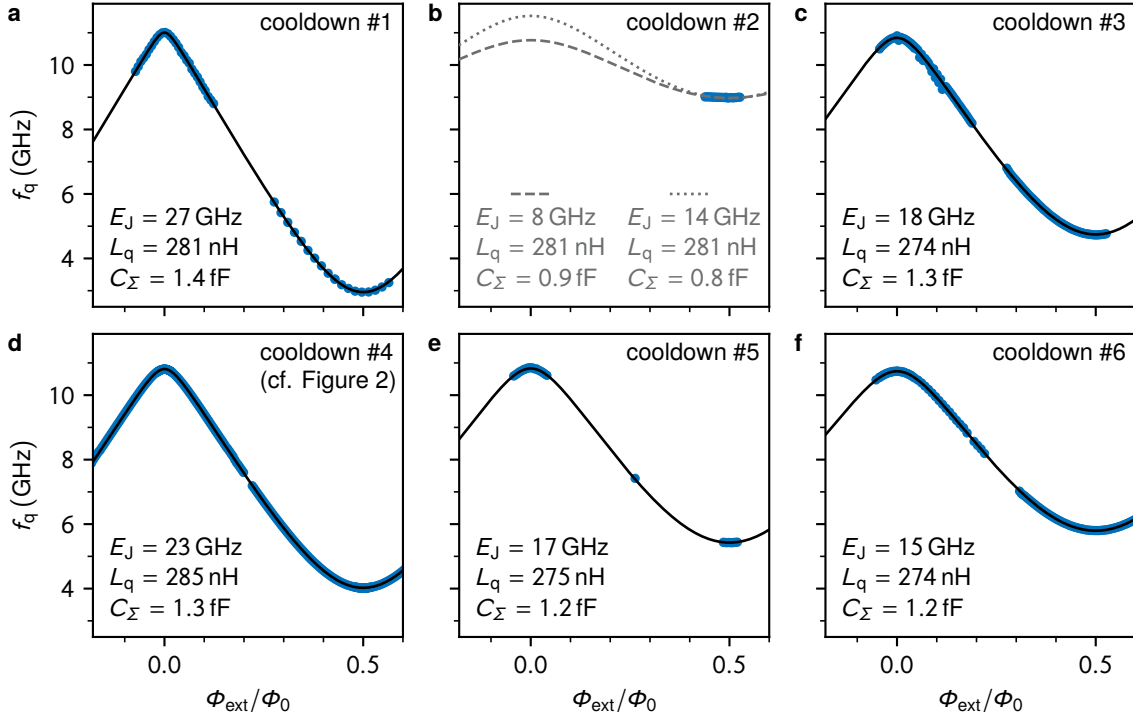
Figure B.9: Gralmonium spectra in successive cooldowns. The panels show the spectra and fit parameters of the main sample in consecutive cooldowns. The blue markers are the $|g\rangle \rightarrow |e\rangle$ transition frequencies extracted from two-tone spectroscopy and the black lines show fits of Eq. (2.2) to the data. The spectrum changes significantly between cooldowns, which is particularly notable around half-flux bias. The changes in half-flux frequency and corresponding E_J are indicated in Fig. 2.6d on the "cooldown" timescale. Comparing the fit parameters evidences relatively large changes in E_J, moderate changes in C_Σ, and constant values of the inductance L_q within few percent. We note that an unambiguous fit for the second cooldown (panel **b**) is difficult because data was only taken around half-flux bias. For this reason, we show two plausible parameter sets by fixing L_q to the value of the previous cooldown and C_Σ around the lower bound $C_q \gtrsim 0.8$ fF expected from the finger capacitance and observed in other samples (cf. Fig. B.10a).
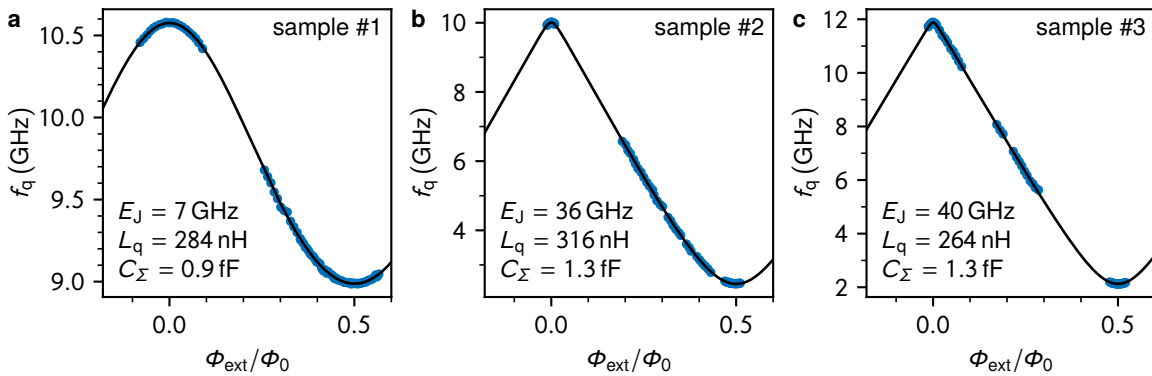
Figure B.10: Spectra of additional gralmonium samples. Similar to Fig. B.9, the blue markers are the $|g\rangle \rightarrow |e\rangle$ transition frequencies extracted from two-tone spectroscopy, the black lines show numerical fits of Eq. (2.2) to the data and the fit paramters are indicated in the panels. **a** In this sample, the Josephson energy of the grAl nano-junction is small enough to lift the entire spectrum of the first transition to the 10 GHz range. **b,c** The parameters of these samples are similar to the gralmonium discussed in the main text (cf. Fig. 2.4b and Table 2.1).

C Details on Josephson Harmonics

This chapter is adapted from the supplementary material of Ref. [2].

C.1 Transmon Samples Overview

Here we introduce the different transmon samples measured for the Josephson harmonics analysis. An overview of the devices is shown in Table C.1 and, in the following, we give a short summary of the properties of each sample. The measured qubit transition and readout resonator frequencies for all samples are listed in Table C.2. More in-depth information, in particular on the KIT and Köln devices, is discussed in the supplementary material of Ref. [2].

KIT

The KIT sample consists of a 3D transmon with a single JJ shunted by an in-plane capacitor with rectangular pads, which is capacitively coupled to an on-chip, lumped-element readout resonator. The resonator is measured in single-port reflection in a 3D waveguide sample holder, similar to Refs. [5, 6]. From finite-element simulations, we extract the charging energy $E_C/h = (242 \pm 1)$ MHz and a series inductance in the leads to the JJ of $L_s \approx 380$ pH. Taking into account an additional contribution from kinetic inductance of $L_{kin} \approx 60\text{--}120$ pH, we expect the total series inductance for the KIT transmon to be at maximum $L_{s,tot} \approx 500$ pH. The sample is fabricated on c-plane, double-side polished sapphire substrate with a bi-layer resist stack of 700 nm MMA EL-13 and 300 nm PMMA A4, and a 10 nm gold conduction layer for e-beam writing. The substrate is cleaned with an Ar/O_2 descum process and the vacuum is improved using titanium gettering, before the metal deposition in a Plassys evaporation system. The aluminum layers are evaporated with target film thicknesses of 30 nm and 40 nm at angles of 0° and 20°, respectively. Between the evaporations, the JJ AlO_x barriers are grown under static oxidation at an oxygen pressure of 10 mbar for 2.5 min. The approximate junction area is $(100\,\text{nm})^2$.

Notably, the KIT sample has been measured in 3 separate cooldowns, which enables an analysis of the spectroscopy with fixed charging energy E_C (given by the geometry of the capacitor pads). In contrast, the Josephson energy and harmonics can evolve between cooldowns, in particular due to aging between cooldown 1 and 2 and accidental thermal annealing at 100 °C between cooldown 2 and 3. In the second cooldown, a DJJAA parametric amplifier [6] has been added to the experimental setup, allowing to extract

the dispersive shifts between the dressed resonator responses for different qubit states. The average energy relaxation and Ramsey coherence times are $T_1 = 8.7\,\mu s$ and $T_2^* = 12\,\mu s$, respectively, measured in the 3rd cooldown of the sample.

Köln

The Köln device, studied in the research group led by Y. Ando and C. Dickel, is a SQUID transmon with rectangular capacitor pads, capacitively coupled to a two-port copper cavity. While the cavity is measured in reflection, additional qubit drive tones or time-domain pulses at the qubit frequency are applied to the second port. The device was fabricated with the same capacitor geometry and in the same batch as the device documented in [110]. The fabrication consists of a single e-beam lithography step using a MMA/PMMA resist stack on sapphire substrate. A weak oxygen plasma was applied to remove resist residues after development. The aluminum layers were evaporated in a Plassys MEB 550S system with target film thicknesses of 10 nm and 18 nm at angles of $\pm 20°$. Between the evaporations, the JJ AlO_x barriers were grown by static oxidation at an oxygen pressure of 1 mbar for 6 min. From AFM imaging, we estimate the areas of the two JJs, $(160\,nm)^2$ and $(260\,nm)^2$. The energy relaxation time of the first excited state is on the order of $T_1 = 10\,\mu s$, the Ramsey coherence time on the order of $T_2^* = 3\,\mu s$, and T_2^{echo} is typically similar to T_1.

The Köln device offers two distinctive features compared to the other transmon samples. Firstly, the transmon can be frequency-tuned by applying magnetic field with a 3-axis vector magnet (cf. Ref. [110]). In this work we focus on the dependence on in-plane magnetic field, which suppresses the effective transmon Josephson energy (-ies), predominantly due to Fraunhofer pattern interference [110, 195]. We estimate the additional suppression of the superconducting gap to contribute at maximum 10 % to the E_{Jm} suppression. Note that the data vs. in-plane magnetic field is mainly taken at the bottom sweetspot of the SQUID (by adjusting the out-of-plane field component).

The second feature is that detailed charge dispersion measurements are available thanks to the possibility to apply a gate-voltage V_g to one of the cavity pins through a bias-tee, which enables control of the offset charge n_g (cf. Section 1.2.2). As a consequence, both the average frequencies f_{0j} and charge dispersion amplitudes δf_{0j} of the transmon transitions can be measured versus in-plane magnetic field. For the magnetic field setting $B = 0.2\,T$ used in Fig. 3.3 in the main text, the measured qubit transition and readout resonator frequencies are listed in Table C.2. The full spectroscopy and charge dispersion data for varying in-plane magnetic fields (shown in Fig. 3.5 in the main text) is available in the repository [230] of Ref. [2].

ENS

The ENS transmon sample, designed and studied in the research group led by Z. Leghtas, is identical to the one documented in Refs. [184, 231]. It is a 3D transmon containing a single JJ shunted by an in-plane plate capacitor with rectangular pads. The transmon is
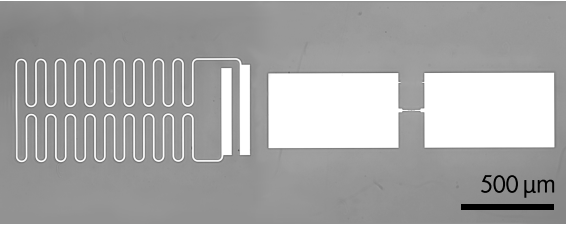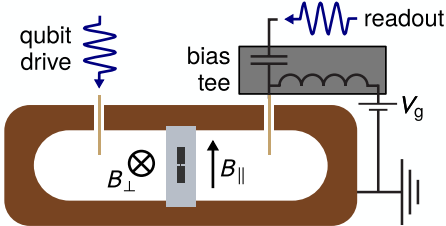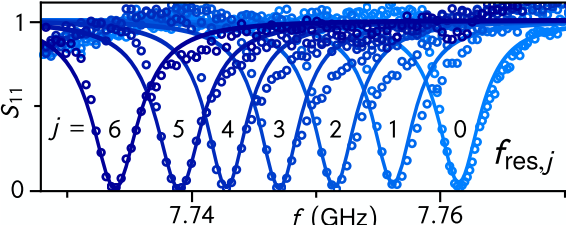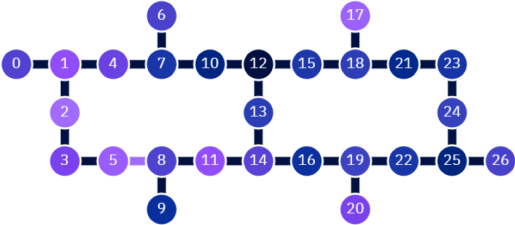
Sample	Schematic	Features
KIT		• readout via 3D waveguide • measured in 3 cooldowns • detailed finite-element simulations
Köln		• frequency-tunable (SQUID & in-plane field) • detailed charge dispersion data
ENS		• measured up to the 6th transition • deep transmon regime of $E_{J1}/E_C \gtrsim 100$
IBM		• commercial multi-qubit processor • statistics on 20 measured qubits

Table C.1: Overview of transmon devices for Josephson harmonics analysis. For each device we show a representative image and list the distinct features of the sample. For KIT, we depict an optical microscope image of a sample similar to the measured one (adapted from Fig. S18 in Ref. [2]). The transmon is coupled to an on-chip lumped-element readout resonator (aluminum in white, sapphire substrate in gray) and measured in a 3D waveguide. For Köln, we show a sketch of the 3D transmon in the two-port readout cavity (adapted from Fig. S23 in Ref. [2]). The charge offset of the transmon can be tuned by applying a voltage V_g to one of the cavity pins and the transmon frequency can be tuned both by applying an in-plane field $B_{\parallel}$ or an out-of-plane field $B_{\perp}$. For ENS, we illustrate the dressed readout resonator responses for 6 different qubit states (adapted from Fig. 3 in Ref. [184]). For IBM, we show the connectivity between the transmons on the IBM *Hanoi* device. The color of each qubit represents the qubit frequency from $f_{01} = 4.719$ GHz (dark blue, Q12) to $f_{01} = 5.256$ GHz (light purple, Q2).

capacitively coupled to a copper cavity, which is read out in transmission. The sample was fabricated in a single e-beam lithography and double-shadow evaporation step on sapphire substrate using a MMA/PMMA resist stack. After an in-situ Ar/O_2 descum cleaning process, the two aluminum layers were evaporated in a Plassys evaporation system with target thicknesses of 35 nm and 100 nm at angles of ±35°. The JJ oxide barrier was grown

Sample		KIT			ENS	Köln		IBM	
		CD1	CD2	CD3		0 T	0.2 T	Q0	Q13
f_{0j}/j (GHz)	1	6.0391	5.8884	4.7219	5.3548	7.1095	5.079	5.0354	4.9632
	2	5.934	5.7777	4.5966	5.2678	6.977	4.912	4.8598	4.791
	3	5.819	5.6596	4.4590	5.1763	–	4.722	4.6698	4.599
	4	5.6945	5.5305	4.3066	5.0792	–	–	4.535	4.4251
	5	5.5588	–	–	4.9758	–	–	–	–
	6	–	–	–	4.8648	–	–	–	–
$f_{\mathrm{res},j}$ (GHz)	0	7.4613	7.4615	7.4564	7.76131	7.5658	–	7.167	7.222
	1	7.4587	7.4589	7.45561	7.75608	7.5838	–	7.1636	7.219
	2	–	–	7.45495	7.75135	–	–	–	–
	3	–	–	7.45415	7.747	–	–	–	–
	4	–	–	–	7.74276	–	–	–	–
	5	–	–	–	7.73902	–	–	–	–
	6	–	–	–	7.73385	–	–	–	–

Table C.2: Transmon spectroscopy data for Josephson harmonics analysis. The top half of the table shows the measured qubit frequencies in terms of multi-photon transitions f_{0j}/j between the ground state and each state j. The bottom half lists the dressed readout resonator frequencies $f_{\mathrm{res},j}$ for the transmon in state j. Two selected field settings $B = 0$ T and $B = 0.2$ T are shown for the Köln device. For the IBM *Hanoi* processor, we list the data for qubits Q0 and Q13. The full data for the Köln transmon and more IBM qubits is available in the repository [230] of Ref. [2].

under static oxidation between the evaporations at a pressure of 20 mbar with a 4:1 $Ar:O_2$ mixture for 7 min. The area of the JJ is 260 nm × 200 nm. The average energy relaxation and Ramsey coherence time of the qubit are $T_1 = 15\,\mu s$ and $T_2^* = 11\,\mu s$, respectively.

IBM

For conformity, we report here the description identical to Ref. [2]: The IBM data was measured on the *Hanoi*, Falcon r5.11 processor for 20 out of the 27 qubits. The transition frequencies of the IBM transmons were obtained by multi-mode spectroscopy (at a single probe frequency) enabled by Qiskit Pulse [232, 233] to measure f_{0j}/j for $j = 1, 2, 3, 4$. Since the $j = 4$ transition frequency was often near the bandwidth limit imposed by Qiskit (± 500 MHz from the $j = 1$ transition), additional sideband modulation was applied at the pulse level to probe those frequencies. For the IBM *Hanoi* qubits 0 and 13, the measured spectroscopy data is listed in Table C.2. The full spectroscopy data for all qubits is available in the repository [230] of Ref. [2].

C.2 Transmon Spectroscopy in the Literature

Since the initial publication [60], transmons have been measured and modeled in a variety of papers in the literature. Notably, most published data only includes the low-energy manifold of the spectroscopy, i.e. typically the lowest two transition frequencies. In this case, agreement with the standard transmon model is guaranteed since the degrees of freedom in the data can be matched perfectly by the free parameters in the model. The same is true when considering the first transition frequency and additional charge dispersion measurements. As an example, Ref. [234] reports measurements of the first two transition frequencies f_{01} and f_{02} for one qubit and measurements of f_{01} and the charge dispersion for another qubit. Consequently, the mismatch to the standard transmon model cannot be analyzed based on the given data.

Interestingly, in the majority of papers in which multiple and sufficiently accurate frequencies are reported, deviations from the standard model are observable, similar to our measurements. In particular, the transmon reported in Ref. [191] shows deviations up to 10 MHz for the 4th transition frequency when modeled without higher Josephson harmonics. Moreover, the device measured in Ref. [192, 193] deviates by up to 400 MHz from the standard model for the 6th transition. An example for spectroscopy which can be described without Josephson harmonics up to $\sim$ MHz deviations at the 5th level is given by the transmon in Ref. [235].

Finally, it should be pointed out that it would not be surprising to find a transmon which is well described by the standard model with purely sinusoidal CφR. Given our mesoscopic model for tunneling through an inhomogeneous AlO$_x$ barrier, such a case would correspond to a JJ with a highly uniform, low-transparency barrier. However, based on the evidence in the literature and our measured data reported in the main text, an agreement with the standard transmon model seems to be the exception for tunnel JJs currently employed in superconducting qubits.

C.3 Fitting methodology

As discussed in the main text in Section 3.3 the methodology to fit the transmon Hamiltonian to the experimental data and obtain the corresponding model parameters is central to interpreting results. In the following, we discuss in more detail the numerical techniques employed in the analysis. First, the approach to diagonalize the standard and Josephson harmonics Hamiltonian is outlined. Next, we explain how model parameters are determined by solving the inverse eigenvalue problem (IEP) given the measured spectroscopy. After discussing briefly the choice of weights in the objective function for fitting the parameters, we detail the procedure to extract the ranges of harmonics consistent with the data. In-depth information on the numerical methods are available in the "Methods" section and supplementary material of Ref. [2]. Note that developing the detailed methodology described in the following was a joint work of D. Willsch, M. Willsch and G. Catelani from FZ Jülich, and the author of this manuscript, within the larger collaboration of Ref. [2].

Hamiltonian Diagonalization

The matrices of the standard transmon model H_{std}, Eq. (3.9), and Josephson harmonics model H_{har}, Eq. (3.11), are constructed in the charge basis $\{|n\rangle\}$, in which $4E_{\text{C}}(n - n_{\text{g}})^2 = \sum_n 4E_{\text{C}}(n - n_{\text{g}})^2 |n\rangle\langle n|$ is diagonal and $-E_{\text{J}m}\cos(m\varphi) = -\sum_n E_{\text{J}m}/2 (|n\rangle\langle n + m| + |n + m\rangle\langle n|)$ has constant entries $-E_{\text{J}m}/2$ on the m-th subdiagonal. We first diagonalize the bare transmon matrix (excluding H_{res}), which yields the transmon eigenenergies E_j and eigenstates $|j\rangle$. Next, the joint transmon-resonator Hamiltonian $H_{\text{std/har}} = \sum_j E_j |j\rangle\langle j| + \Omega a^\dagger a + \sum_{j,j'} G |j\rangle\langle j|n|j'\rangle\langle j'| (a + a^\dagger)$ is diagonalized, in which $a = \sum_k \sqrt{k+1} |k\rangle\langle k+1|$. By assigning a photon number label k and transmon state label j to each resulting eigenenergy $E_{\bar{l}}$ and eigenstate $|\bar{l}\rangle$ based on the largest overlap $\max_{k,j} |\langle kj|\bar{l}\rangle|$, we find the dressed energies $E_{\overline{kj}}$ and states $|\overline{kj}\rangle$.

This procedure is carried out for both offset charge values $n_{\text{g}} = 0$ and $n_{\text{g}} = 1/2$ and results in the transmon transition frequencies $hf_{0j}^{\text{model}}(n_{\text{g}}) = E_{\overline{0j}}(n_{\text{g}}) - E_{\overline{00}}(n_{\text{g}})$ and the resonator frequencies $hf_{\text{res},j}^{\text{model}}(n_{\text{g}}) = E_{\overline{1j}}(n_{\text{g}}) - E_{\overline{0j}}(n_{\text{g}})$. The predicted model frequencies are then given by the averages $f_{0j}^{\text{model}} = [f_{0j}^{\text{model}}(0) + f_{0j}^{\text{model}}(1/2)]/2$ and $f_{\text{res},j}^{\text{model}} = [f_{\text{res},j}^{\text{model}}(0) + f_{\text{res},j}^{\text{model}}(1/2)]/2$, and the charge dispersion amplitude is given by $\delta f_{0j}^{\text{model}} = |f_{0j}^{\text{model}}(0) - f_{0j}^{\text{model}}(1/2)|$. For the diagonalization, we consistently use $n = -N, \ldots, N$ with $N = 14$ (i.e. in total $2N + 1 = 29$) charge states, $j = 0, \ldots, M - 1$ with $M = 12$ transmon states, and $k = 0, \ldots, K - 1$ with $K = 9$ resonator states. The cut-offs N, M and K have been chosen such that adding more states does not change the model predictions significantly.

Obtaining Model Parameters by Solving the IEP

The problem of obtaining the parameters $\mathbf{x}^{\text{std}}$ of the standard transmon model and $\mathbf{x}^{\text{har}}$ of the Josephson harmonics model, such that the linear combinations of eigenvalues $\mathbf{f} = (f_{01}^{\text{model}}, f_{02}^{\text{model}}, \ldots, f_{0N_f}^{\text{model}}, f_{\text{res},0}^{\text{model}}, f_{\text{res},1}^{\text{model}})$ agree with the measured data, belongs to the class of *Hamiltonian parameterized inverse eigenvalue problems* (HamPIEPs). In our case, we solve the HamPIEP using the globally convergent Newton method [236] with cubic line search and backtracking [237] and the Broyden-Fletcher-Goldfarb-Shanno (BFGS) algorithm [238] as implemented in TensorFlow Probability [239]. The Jacobian $\partial\mathbf{f}/\partial\mathbf{x}$ is obtained by performing automatic differentiation through the diagonalization with TensorFlow.

For the $E_{\text{J}4}$ model shown in Fig. 3.3c, the IEP is solved unambiguously for the parameters $\mathbf{x} = (E_{\text{J}1}, E_{\text{J}2}, E_{\text{J}3}, E_{\text{J}4}, \Omega, G)$ given the lowest 4 transmon transition frequencies and by fixing the charging energy values $E_{\text{C}}^{\text{KIT}}/h = 242\,\text{MHz}$, $E_{\text{C}}^{\text{ENS}}/h = 180\,\text{MHz}$, and $E_{\text{C}}^{\text{IBM}}/h = 300\,\text{MHz}$. This approach ensures that all samples can be treated identically and the models are consistent with knowledge of the transmon capacitance, for example based on finite-element simulations (cf. Appendix C.1). For the mesoscopic model (see Section 3.1.3), the parameters $\mathbf{x} = (\bar{d}, \sigma, E_{\text{C}}, E_{\text{J}}, \Omega, G)$ are determined by minimizing the objective function $\sum_{j=1}^{N_f} |f_{0j}^{\text{model}} - f_{0j}^{\text{experiment}}|/j + \sum_{j=0}^{1} |f_{\text{res},j}^{\text{model}} - f_{\text{res},j}^{\text{exp.}}|$ using the BFGS algorithm. The initial

Sample	Model	E_C/h	E_J/h	E_{J2}/E_J	E_{J3}/E_J	E_{J4}/E_J	$\bar{d}$	σ_d	Ω/h	G/h
KIT CD1	E_J	0.197	24.852	-	-	-	-	-	7.454	0.078
	E_{J2}	0.242	21.801	-0.019	-	-	-	-	7.454	0.086
	E_{J4}	0.242	21.997	-0.026	0.004	-0.001	-	-	7.454	0.086
	$\bar{d}, \sigma_d$	0.293	20.186	-0.067	0.017	-0.007	1.06	0.45	7.454	0.095
KIT CD2	E_J	0.206	22.704	-	-	-	-	-	7.454	0.086
	E_{J2}	0.242	20.530	-0.016	-	-	-	-	7.454	0.093
	E_{J4}	0.242	20.383	-0.010	-0.003	0.001	-	-	7.454	0.093
	$\bar{d}, \sigma_d$	0.284	19.361	-0.057	0.014	-0.005	1.62	0.50	7.454	0.101
KIT CD3	E_J	0.223	13.803	-	-	-	-	-	7.454	0.080
	E_{J2}	0.242	13.164	-0.009	-	-	-	-	7.454	0.083
	E_{J4}	0.242	13.225	-0.013	0.002	-0.001	-	-	7.454	0.083
	$\bar{d}, \sigma_d$	0.254	12.977	-0.024	0.005	-0.002	1.62	0.38	7.454	0.085
ENS	E_J	0.167	23.191	-	-	-	-	-	7.739	0.179
	E_{J2}	0.181	22.053	-0.008	-	-	-	-	7.739	0.187
	E_{J4}	0.186	21.811	-0.014	0.001	-0.000	-	-	7.739	0.189
	$\bar{d}, \sigma_d$	0.195	21.505	-0.028	0.006	-0.002	1.63	0.39	7.739	0.194
Köln	E_J	0.285	16.785	-	-	-	-	-	7.545	0.077
	E_{J4}	0.330	15.577	-0.023	0.004	-0.001	-	-	7.545	0.083
	$\bar{d}, \sigma_d$	0.331	15.627	-0.027	0.006	-0.002	1.93	0.43	7.545	0.083
IBM Q0	E_J	0.302	11.925	-	-	-	-	-	7.160	0.133
	E_{J4}	0.300	14.672	-0.141	0.083	-0.027	-	-	7.160	0.133

Table C.3: Parameters of standard transmon and Josephson harmonics models. The models are referred to as E_J for the standard transmon model Eq. (3.9), E_{J2} and E_{J4} for phenomenological Josephson harmonics models Eq. (3.11) truncated at the 2nd and 4th harmonic, respectively, and $\bar{d}, \sigma_d$ for the mesoscopic model (see Section 3.1.3). While the E_{Jm}/E_J are fit parameters in the phenomenological models, they are calculated based on the mean $\bar{d}$ and standard deviation σ_d of the barrier thickness in the mesoscopic model. The barrier dimensions are given in nanometers, the energy ratios are unitless and all other parameters are given in gigahertz. For the Köln sample, we indicate the E_J corresponding to zero magnetic field. All parameters have been obtained by solving the HamPIEP (cf. Appendix C.3).

values for the minimization are given by $\bar{d} = 1.64\,\text{nm}$ (taken from the molecular dynamics result in Appendix C.6), $\sigma = \bar{d}/4$, and (E_C, E_J, Ω, G) from the standard transmon model. For the Köln data, 288 data points (as shown in the frequency sweep Fig. 3.5a) have to be described with the same model parameters **x** by only varying the first Josephson energy. To fulfill this constraint, we use cubic interpolation as a function of f_{01}^{model} and include only a few central points for the available frequencies in the solution of the IEP. The model parameters of the samples for the standard transmon model, phenomenological models truncated at E_{J2} and E_{J4}, and the mesoscopic model are listed in Table C.3. For the parameters of additional models and samples, see the supplementary material of Ref. [2] or the corresponding repository [230].

Choice of Weights in the Objective Function

For models with a number of parameters #$\mathbf{x}$ smaller than the number of measured transition frequencies #$\mathbf{f}$, the HamPIEP cannot be solved unambiguously. Instead, as mentioned above for the mesoscopic model, the solution is found by minimizing an objective function given by the weighted sum of absolute differences between measured and modeled transition frequencies,

$$\sum_{j=1}^{N_{\mathrm{tr}}} w_{0j} \left| f_{0j}^{\mathrm{model}} - f_{0j}^{\mathrm{exp.}} \right| + \sum_{j=0}^{N_{\mathrm{res}}} w_{\mathrm{res},j} \left| f_{\mathrm{res},j}^{\mathrm{model}} - f_{\mathrm{res},j}^{\mathrm{exp.}} \right| , \tag{C.1}$$

in which w_{0j} and $w_{\mathrm{res},j}$ are weights for the transmon and resonator frequencies, respectively. Importantly, the choice of the weights influences which frequencies are prioritized to be matched by the fit but it does not change if a model can or cannot describe the full set of measured transitions accurately [2].

For models which can describe the data reasonably, a straightforward choice of the weights is $w_{0j} = 1/j$ for the qubit and $w_{\mathrm{res},j} = 1$ for the first two resonator frequencies. The first choice is motivated by the multi-photon transitions $f_{0j}^{\mathrm{exp.}}/j$ being measured with similar uncertainty $\lesssim 1\,\mathrm{MHz}$. For the resonator, the weights ensure that the dispersive shift χ_{01} between qubit ground and first excited state is matched by the fit.

In contrast, for models which deviate systematically from the data like the standard transmon model (cf. Fig. 3.3b), the choice $w_{0j} = 1/j$ leads to the fit matching all frequencies on average (due to the curvature of the deviations). Instead, for such models we take the choice to put priority on the first two transmon transitions $w_{01} = w_{02} = 1$ for several reasons. First, the approach ensures consistency with the conventional approach of fitting *only* the first two transitions with the standard model parameters $E_{\mathrm{J}}, E_{\mathrm{C}}$. Moreover, the fundamental transition is typically available with the best experimental precision by measuring Ramsey fringes. Finally, the systematic uncertainty is increasing for the higher levels due to charge dispersion (cf. Section 1.2.2). Different cases for the choice of weights are discussed in detail in the supplementary Section II B of Ref. [2].

Extracting Ranges of Josephson Harmonics

Here we detail how the ranges of $E_{\mathrm{J}m}$ consistent with measured spectroscopy for a sample, as shown in Fig. 3.4, are obtained. Solving the HamPIEP for a dataset including N_f measured transition frequencies f_{0j}, $j = 1, \ldots, N_f$, and two resonator frequencies $f_{\mathrm{res},0}$ and $f_{\mathrm{res},1}$ uniquely determines the parameters $\mathbf{x} = (E_{\mathrm{J}1}, \ldots, E_{\mathrm{J}N_f}, \Omega, G)$. In order to extract ranges of the first N_f Josephson energies, we include varying values of four additional ratios $\mathbf{y} = (E_{\mathrm{J}N_f+1}/E_{\mathrm{J}1}, \ldots, E_{\mathrm{J}N_f+4}/E_{\mathrm{J}1})$. In particular, we scan each of these four $E_{\mathrm{J}m}/E_{\mathrm{J}1}$ over 16 geometrically spaced values between the point contact limit $3(-1)^{m+1}/(4m^2 - 1)$ and $(-1)^{m+1} \min\{10^{-7}, |E_{\mathrm{J}m+1}/E_{\mathrm{J}1}|\}$, for which the first entry is always skipped to ensure $|E_{\mathrm{J}m}/E_{\mathrm{J}1}| > |E_{\mathrm{J}m+1}/E_{\mathrm{J}1}|$. Additionally we test $\mathbf{y} = (0, 0, 0, 0)$ to check if the model can be truncated at $E_{\mathrm{J}N_f}$.

Given each additional parameter combination $\mathbf{y}$, the HamPIEP can be solved for the spectroscopy data to obtain the unique solution $\mathbf{x}$. We note that some of the solutions for the E_{Jm} extracted with the scanning procedure might correspond to unphysical solutions because (i) some of the leading ratios E_{Jm}/E_J for $m \leq N_f$ might be larger than the fully open point contact limit, (ii) the magnitudes $|E_{Jm}|$ might not be strictly decreasing for increasing order m, or (iii) the signs might not be alternating. These unphysical outcomes can also occur when the Josephson harmonics model Eq. (3.11) is truncated at too low orders. The maximum and minimum possible ratios $|E_{Jm}/E_J|$ extracted based on the described procedure define the vertical bars shown in Fig. 3.4.

C.4 Additional Hamiltonian Contributions

In the following sections, we summarize briefly the influence of additional contributions in the standard transmon Hamiltonian instead of including higher Josephson harmonics. Corresponding plots illustrating the magnitude of deviations from the standard model expected from these considerations are shown in Fig. C.1. An in-depth treatment and discussion of each alternative contribution is available in supplementary Section I D of Ref. [2]. Note that the analysis described in the following was a joint work of D. Willsch, M. Willsch and G. Catelani from FZ Jülich, and the author of this manuscript, within the larger collaboration of Ref. [2].

Series Inductance

One possible addition to the standard transmon model arises from the wires connecting the JJ to the capacitor pads. Due to their elongated geometry they come with a potentially relevant geometrical and kinetic inductance. As an example, for the KIT sample we estimate these contributions to sum up to an inductance of $L_{s,tot} \lesssim 500\,\text{pH}$ in series to the JJ (cf. Appendix C.1). This value corresponds to an inductive energy scale $E_L = (\Phi_0/2\pi)^2/L_q$ of $E_L/h \gtrsim 300\,\text{GHz}$ such that $E_J/E_L \ll 1$. The series inductance can be included in the transmon hamiltonian by adding the inductive energy term,

$$H = 4E_C(n - n_g)^2 - E_J \cos\varphi_J + \frac{E_L}{2}\varphi_L^2. \tag{C.2}$$

The effect of the series inductance is that the phase drop in parallel to the capacitor is now distributed across the inductance, φ_L, and the junction, φ_J.

The relation between φ_J and φ_L is given by a transcendental equation [2] but, due to its symmetry properties, the 2π-periodicity of the Hamiltonian is conserved despite the presence of the φ^2 term. As a consequence, the Hamiltonian can be written in terms of a Fourier series similar to the Josephson harmonics series Eq. (3.11). Interestingly, the coefficients of the series have similar properties to harmonics, i.e. an alternating sign and decreasing magnitude with higher order. As an example, for the KIT sample with

$E_J/E_L \approx 0.07$ we find $-1.75\,\%$ and $0.061\,\%$ contributions of the $\cos 2\varphi$ and $\cos 3\varphi$ term, respectively, relative to the E_J of the JJ.

Fig. C.1a shows the remaining deviations from the measured spectroscopy of the KIT sample when including various sizes of series inductance in the Hamiltonian Eq. (C.2). Most importantly, even for the conservatively estimated upper bound for the device, the series inductance cannot explain the measured deviations. In order to bring the transition frequencies close to the measured values, the series inductance would have to be at least a factor of 2 larger than expected. In summary, while series inductance can lead to similar kinds of corrections to the standard model as higher Josephson harmonics, it cannot explain the measured deviations. Note that by considering series inductance in the Josephson harmonics model, the ranges of harmonics consistent with the measured data (cf. Fig. 3.4) would be shifted to lower values.

Hidden Modes

While we include the coupling to the readout resonator mode in the transmon models, additional hidden modes can, in principle, impact the transmon spectrum due to hybridization. These modes would be considered "dark" modes to the transmon as their coupling strength G_{dark} should be considerably smaller than the intended readout-qubit coupling which is designed strong on purpose. We test the effect of an additional dark mode at frequency Ω_{dark} by adding the corresponding terms in the standard transmon model,

$$H = H_{\mathrm{std}} + \Omega_{\mathrm{dark}} b^\dagger b + G_{\mathrm{dark}} n(b + b^\dagger),$$ (C.3)

in which $b^\dagger$ (b) are the hidden mode's creation (annihilation) operators. We consider a coupling of $G_{\mathrm{dark}}/h = 9\,\mathrm{MHz}$, a factor of 10 smaller than the coupling estimated for the standard model of the KIT sample (cf. Table C.3).

As expected and as shown in Fig. C.1b, the addition of the dark mode only has significant influence on the higher transmon transition frequencies if Ω_{dark} is placed in proximity to other transitions in the spectrum, for example f_{01} of the transmon. Even then, due to the curvature of the measured deviations from the standard model, including a dark mode cannot align the model predictions of the full spectroscopy dataset. Consequently, hidden modes are an unlikely explanation for the measured deviations from the standard transmon model. Multiple modes would have to be placed at particular frequencies and coupling strengths to match the model to the experimental data — a situation which is implausible both for 3D waveguide or cavity architectures and 2D chip designs.

Multi-Qubit Coupling

For the IBM *Hanoi* multi-qubit device, an additional contribution to deviations from the standard transmon model can arise from the qubit-qubit coupling on the the chip. The transmons are coupled by short coplanar waveguide resonators with resonant frequencies
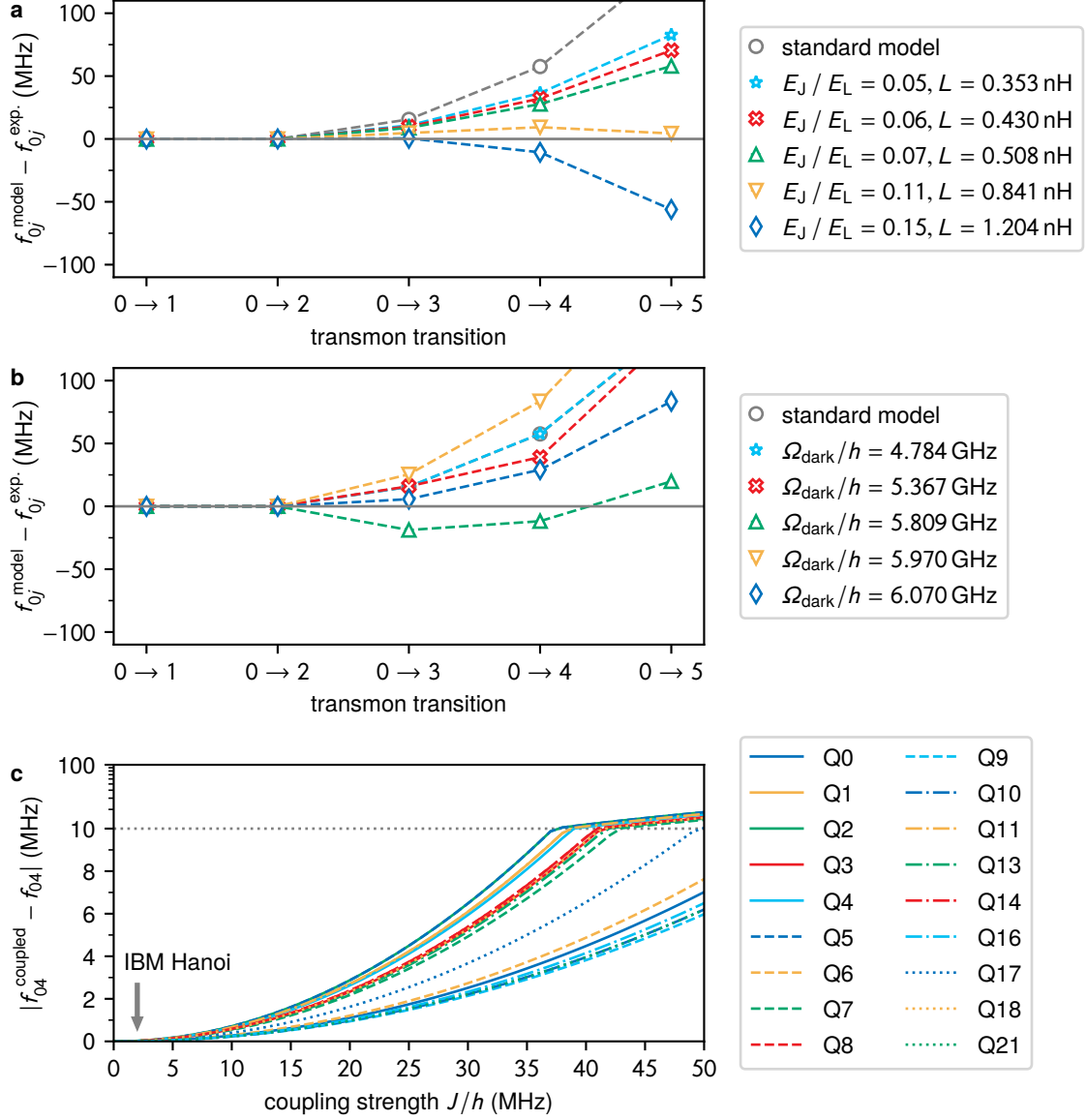
Figure C.1: Influence of additional contributions to the transmon Hamiltonian. **a** Difference between frequencies f_{0j}^{model} predicted by the Hamiltonian Eq. (C.2) including series inductance and the frequencies $f_{0j}^{\mathrm{exp.}}$ measured for the KIT sample for transmon transitions $|0\rangle \rightarrow |j\rangle$. The colors correspond to various values of the inductance, as indicated in the legend; dashed lines are guides to the eye. Gray circles denote the standard transmon model, corresponding to the limit $L = 0$. We estimate a total series inductance of 0.5 nH for the sample, for which deviations up to 50 MHz remain (green triangles). **b** Plot similar to panel a but using the Hamiltonian Eq. (C.3) including a dark mode at frequency Ω_{dark} as indicated by the legend. We fix the coupling to the qubit at $G_{\mathrm{dark}}/h = 9$ MHz; gray circles denote the standard transmon model without the dark mode. The additional mode cannot remove the measured deviations. **c** Absolute difference of the frequencies $f_{04}^{\mathrm{coupled}}$ obtained from diagonalization of the capacitively coupled multi-transmon system Eq. (C.4) and the frequencies f_{04} obtained from the diagonalization of the single-transmon-resonator system depending on coupling strength J. The colors indicate the 20 measured qubits (see legend). The gray arrow indicates the design value of 2 MHz for the IBM *Hanoi* device, at which the change of all frequencies is lower than 1 MHz. The same observation holds for the lower transitions f_{0j} with $j = 1, 2, 3$. This figure is adapted from Figs. S10, S12, S13 in Ref. [2].

much larger than the transmon transition frequencies. For this reason, the coupling can be treated as capacitive transmon-transmon coupling given by a Hamiltonian of the form

$$H = H_{\text{std},i} + \sum_{\langle i,j \rangle} J\, n_i n_j\,, \tag{C.4}$$

in which $H_{\text{std},i}$ is the standard Hamiltonian of transmon i including its readout resonator and J the capacitive coupling strength between all connected transmon pairs $\langle i,j \rangle$. The connectivity of the IBM *Hanoi* device is shown in Table C.1.

We diagonalize the Hamiltonian for the joint system of up to three neighboring transmons and their readout resonators. Fig. C.1c shows the absolute difference $|f_{0j}^{\text{coupled}} - f_{0j}|$ between the coupled and the uncoupled systems as a function of the coupling strength J for all qubits measured up to level $|4\rangle$ and coupled to at least one such qubit. By varying the coupling on a scale of 0 to 50 MHz [240] we find that for values of $J/h \approx 2\,\text{MHz}$, relevant for the IBM *Hanoi* device, the effect on the spectrum is marginal. In summary, the transmon-transmon coupling on the IBM *Hanoi* chip cannot explain the measured deviations from the standard transmon Hamiltonian shown in Fig. 3.3b.

Asymmetry in Superconducting Gaps of Junction Electrodes

Typically, the film thickness of the top electrode in Al-AlO$_x$-Al tunnel JJs is chosen larger than the thickness of the bottom electrode to ensure the overlap area of the junction is properly contacted with the lead (see schematic in Fig. 3.2a). As a consequence, the superconducting gaps of the two electrodes can differ slightly $\Delta_1 \neq \Delta_2$ due to the gap's dependence on film thickness. What is the influence of this asymmetry on the JJ current-phase relation?

It turns out that the higher harmonic contributions are, in fact, suppressed with increasing asymmetry in the gaps [2] compared to the case of a single (symmetric) gap discussed in the main text Section 3.1.2. In particular, for a realistic assumption on the asymmetry $\Delta_1/\Delta_2 = 0.9$, the second harmonic coefficient is reduced by 0.07 % and for an extreme regime of $\Delta_1/\Delta_2 = 0.5$, the suppression reaches 2.9 %. Moreover, the suppression is the strongest in the low-transparency limit of the current-phase relation. In conclusion, an asymmetry in the superconducting gaps of the JJ leads, would not help to explain deviations from the standard transmon model but instead marginally suppress the presence of Josephson harmonics.

C.5 Engineering Josephson Harmonics

As discussed in the main text (see Fig. 3.5b), the IBM transmons evidence that significant contributions from higher harmonics $E_{\text{J2}}, E_{\text{J3}}, E_{\text{J4}}$ (cf. Fig. 3.4b,c) can reduce the charge dispersion δf while keeping the anharmonicity $|\alpha| = 2\pi|f_{12} - f_{01}|$ constant. In contrast, in the standard transmon model, lowering the charge dispersion by increasing $E_{\text{J}}/E_{\text{C}}$
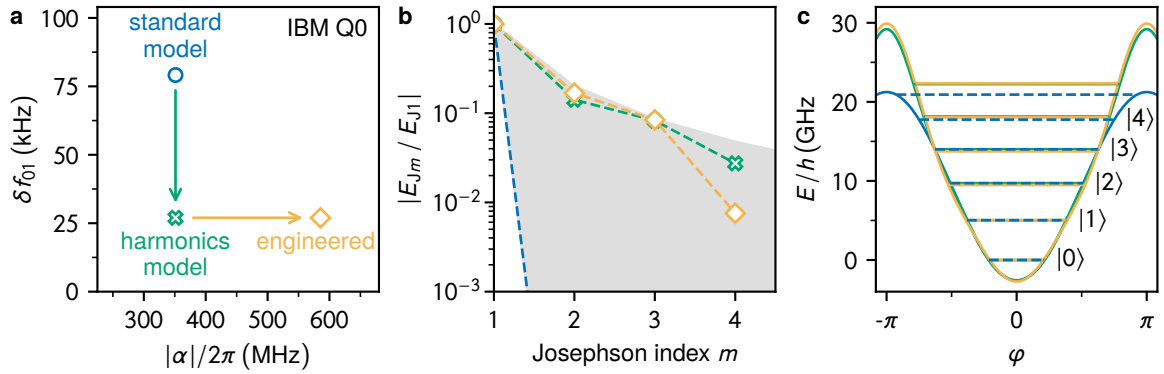
Figure C.2: Engineering Josephson harmonics for transmons. **a** Placement of standard model (blue circle), the E_{J4} harmonics model (green cross), and an engineered E_{J4} model with increased anharmonicity (yellow diamond) in a 2D plot of charge dispersion δf_{01} and absolute anharmonicity $|\alpha|$ for IBM Q0. For the engineered model, the parameters are chosen such that the qubit frequency f_{01}, the resonator frequency $f_{\text{res},0}$, and the charge dispersion δf_{01} stay constant. **b** Josephson harmonics energy ratios $|E_{Jm}/E_{J1}|$ corresponding to the models shown in panel a. **c** Potential energies corresponding to the models shown in panel a. Panels b and c use the same coloring as panel a. This figure is adapted from Fig. S8 in Ref. [2].

would reduce the anharmonicity (cf. Section 1.2.2). Building upon this evidence, can the anharmonicity also be increased by further engineering the E_{Jm} contributions?

In Fig. C.2, we show that, indeed, sets of E_{Jm} coefficients exist, which result in a reduced charge dispersion (gren arrow in Fig. C.2a) and increased anharmonicity (yellow arrow) compared to the standard transmon expectation. The Josephson harmonics energy ratios corresponding to the models are plotted in Fig. C.2b. The main reason for the increased anharmonicity is a reduction of E_{J4}, while E_{J2} and E_{J3} remain almost unchanged. Intuitively, E_{J3} must stay large to maintain the height of the potential for the reduced charge dispersion. On top of that, the reduced E_{J4} slightly widens the potential around level $|2\rangle$, which draws the level towards the bottom of the potential well and thus increases the anharmonicity, as illustrated in Fig. C.2c.

We note that in practice it is not straightforward to tune the values of coefficients (E_{J2}, E_{J3}, E_{J4}) to arbitrary values. Achieving this level of control, likely requires a combination of various strategies, such as shaping the channels' transparencies, adding inductive elements in series, flux bias, etc. (cf. also Ref. [206]). As a consequence, it is currently an open question whether it is possible or not to engineer a set of Josephson harmonics E_{Jm}, similar to the values discussed here, in a real device.

C.6 Evidence for AlO$_x$ Barrier Inhomogeneity

The mesoscopic model discussed in the main text is based on the observation that a realistic AlO$_x$ tunnel barrier, fabricated with standard shadow evaporation techniques, is inhomogeneous. In particular, the model predicts the magnitude of Josephson harmonics based on assumptions on the thickness variations of the barrier. The atomic-scale structure of an AlO$_x$ barrier is illustrated in Fig. 3.2b,c with a STEM micrograph and two images
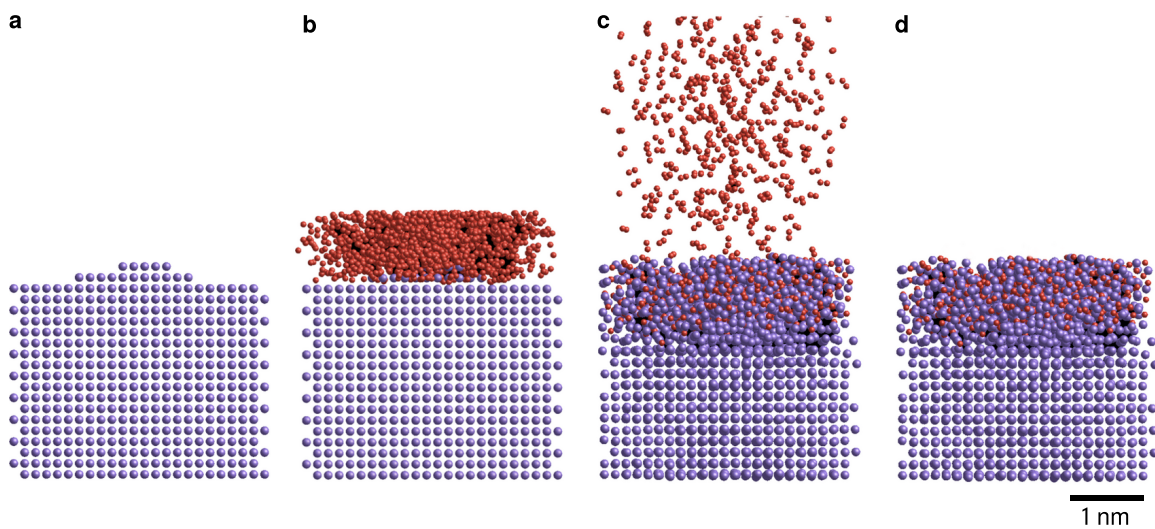
Figure C.3: Stages of molecular dynamics model for AlO$_x$ barrier growth. **a** Initial construction of an Al(100) model with double island defect from Al atoms (violet) in a face-centered cubic crystal structure. **b** Oxygen atoms (red) are randomly added to the model with a minimum and maximum Al-O-atom distance of 1 Å and 10 Å, respectively. **c** The system is propagated for 1500 steps of Verlet molecular dynamics at 300 K with a time step length of 2 fs. **d** The remaining free oxygen is removed from the system, resulting in aluminum structures wrapped in a layer of AlO$_x$ that can be used for the analysis in surface-like or junction-like configurations. The simulations have been performed at ITIM, Cluj, Romania, and the figure is adapted from Fig. S25 in Ref. [2].

resulting from molecular dynamics simulation of the barrier growth. In the following sections we further substantiate the material provided in the main text by outlining the procedure for the molecular dynamics simulation and showing additional STEM images.

C.6.1 Molecular Dynamics Simulation

The molecular dynamics (MD) simulations have been conceived and performed at ITIM, Cluj, Romania. Detailed technical information on the simulations are available in the supplementary material of Ref. [2]. In the following, we summarize the main approach for the simulations and discuss in detail the results regarding the barrier inhomogeneity, relevant for the mesoscopic model.

The orientation of crystalline aluminum grains in junction electrodes grown by standard shadow evaporation techniques is random. For this reason, in the MD simulations, we consider two distinct cases for the geometric structure of the surfaces: Al(100) and Al(111), corresponding to opposite extremes which we average over. A similar approach using Al(100) and Al(111) to investigate junction properties was recently proposed in Ref. [178]. Several models for the Al crystal are generated both with ideal (flat) configuration and with various types of defects, such as steps or islands. As an example, Fig. C.3a shows a model with a double island configuration. Next, the Al crystals are allowed to interact with gaseous oxygen atoms placed on top (Fig. C.3b). The initial ratio between oxygen and aluminum is approximately 1:2, i.e. the initial oxygen represents a third of the total number

of atoms in the system (12x12x20=2880 Al atoms and 1500 O atoms). For each model the system is propagated at 300 K for 3 ps, with a time step of 2 fs, as illustrated in Fig. C.3b-d. During propagation, the aluminum layer incorporates oxygen atoms (Fig. C.3c). Since we are only interested in the resulting solid structure, the oxygen atoms that remain unbound are removed after the propagation, as shown in Fig. C.3d.

After the MD relaxation, the differences between the Al(100) and Al(111) systems can be analyzed. First, we observe that Al(100) accepts, on average, up to 2 % more oxygen, with the percentage referring to the total number of atoms. Moreover, we find that surfaces with defects generally accept more oxygen. For the purpose of simulating tunnel junctions, the thickness of the AlO$_x$ barrier is of particular interest. It can be calculated as the difference between the coordinates of the first and the last atom that forms the AlO$_x$ layer. Interestingly, with an average thickness of 16.4 Å the barrier formed on Al(111) is 2 Å thicker than the one formed on Al(100), when averaging over the different defect models. This result is surprising considering that Al(111) generally accepts fewer oxygen atoms than the aluminum in symmetry (100). Comparing the Al-O bond lengths, we obtain only a slightly larger length for Al(111), i.e. (1.96 ± 0.16) Å instead of (1.95 ± 0.17) Å for Al(100). Therefore, the difference in the length of the Al-O bonds formed on the two types of bulk does not explain the difference in the oxide thickness of up to 2 Å.

However, the analysis of the structure and composition of the systems shows that different chemical bonds are formed between aluminum and oxygen in the AlO$_x$ layer, depending on the surface orientation. In Al(111), even though it incorporates less oxygen compared to Al(100), a higher percentage of oxide and sub-oxide is formed, resulting in a thicker barrier. This fact, correlated with the bond lengths and the penetration depth of oxygen, indicates that the thickness of the AlO$_x$ layer depends on the type and quality of the surface. The rougher the surface, the more oxygen it absorbs and, consequently, the larger the barrier thickness. Since a typical tunnel junction barrier is obtained by oxidizing a poly-crystalline film with grains much smaller than the junction and with random orientations, we expect the barrier to be inhomogeneous: depending on the crystalline orientation and oxide thickness at their respective positions, the conduction channels will have different transparencies.

C.6.2 Scanning Transmission Electron Microscopy

In Fig. C.4, we show additional STEM images of Al-AlO$_x$-Al barriers fabricated by e-beam deposition of aluminum and thermal oxidation. The images have been taken in the research group led by P. Schüffelgen and D. Grützmacher at FZ Jülich. The inhomogeneities illustrated by the micrographs are qualitatively similar to the simulated molecular dynamics results.
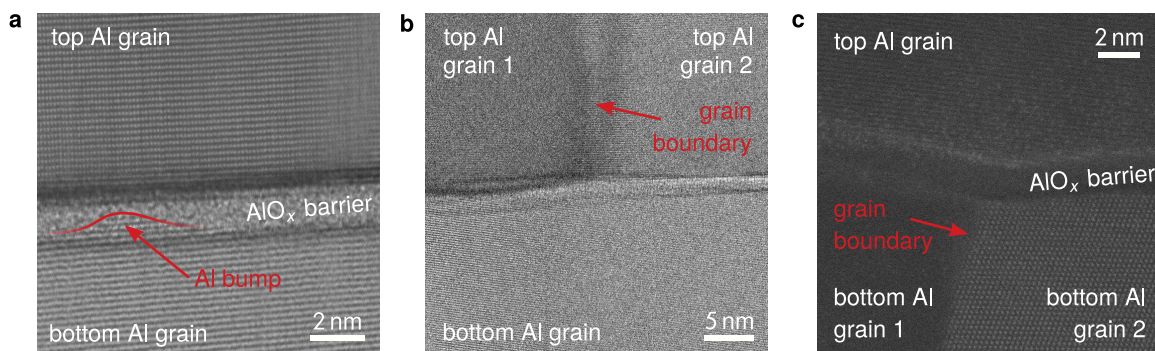
Figure C.4: Additional STEM images of AlO$_x$ JJ barriers. **a** Bright field (BF) STEM image of a barrier grown under static oxidation at 1 mbar for 30 min. The image is acquired with both zone axes misaligned, confirming the crystallinity of both the upper and lower electrode simultaneously. The rotational misalignment of the crystals explains the linear patterns compared to the dotted pattern in Fig. 3.2b in the main text. In this image, the Al grain of the bottom electrode is not homogeneously oxidized; crystalline Al reaches into the barrier region (cf. linear pattern indicated by the red arrow and line), reducing the barrier thickness locally. **b** A zoomed-out BF-STEM image of a different part of the barrier in panel a showing a grain boundary in the top Al electrode, indicated by the red arrow. **c** High-angle annular dark field (HAADF) STEM image of a different region of the barrier shown in Fig. 3.2b in the main text. The image shows a grain boundary of the bottom Al electrode, indicated by the red arrow. The STEM images have been taken in the research group led by P. Schüffelgen and D. Grützmacher at FZ Jülich, and the figure is adapted from Fig. S27 in Ref. [2].

Bibliography

[1] D. Rieger, S. Günzler, M. Spiecker, P. Paluch, P. Winkel, L. Hahn, J. K. Hohmann, A. Bacher, W. Wernsdorfer, and I. M. Pop, "Granular aluminium nanojunction fluxonium qubit", Nat. Mater. **22**, 194–199 (2023).

[2] D. Willsch, D. Rieger, P. Winkel, M. Willsch, C. Dickel, J. Krause, Y. Ando, R. Lescanne, Z. Leghtas, N. T. Bronn, P. Deb, O. Lanes, Z. K. Minev, B. Dennig, S. Geisert, S. Günzler, S. Ihssen, P. Paluch, T. Reisinger, R. Hanna, J. H. Bae, P. Schüffelgen, D. Grützmacher, L. Buimaga-Iarinca, C. Morari, W. Wernsdorfer, D. P. DiVincenzo, K. Michielsen, G. Catelani, and I. M. Pop, "Observation of Josephson Harmonics in Tunnel Junctions", arXiv, `10.48550/arXiv.2302.09192` (2023).

[3] D. Rieger, S. Günzler, M. Spiecker, A. Nambisan, W. Wernsdorfer, and I. M. Pop, "Fano Interference in Microwave Resonator Measurements", Phys. Rev. Appl. **20**, 014059 (2023).

[4] K. Borisov, D. Rieger, P. Winkel, F. Henriques, F. Valenti, A. Ionita, M. Wessbecher, M. Spiecker, D. Gusenkova, I. M. Pop, and W. Wernsdorfer, "Superconducting granular aluminum resonators resilient to magnetic fields up to 1 Tesla", Appl. Phys. Lett. **117**, 120502 (2020).

[5] P. Winkel, K. Borisov, L. Grünhaupt, D. Rieger, M. Spiecker, F. Valenti, A. V. Ustinov, W. Wernsdorfer, and I. M. Pop, "Implementation of a Transmon Qubit Using Superconducting Granular Aluminum", Phys. Rev. X **10**, 031032 (2020).

[6] P. Winkel, I. Takmakov, D. Rieger, L. Planat, W. Hasch-Guichard, L. Grünhaupt, N. Maleeva, F. Foroughi, F. Henriques, K. Borisov, J. Ferrero, A. V. Ustinov, W. Wernsdorfer, N. Roch, and I. M. Pop, "Nondegenerate Parametric Amplifiers Based on Dispersion-Engineered Josephson-Junction Arrays", Phys. Rev. Appl. **13**, 024015 (2020).

[7] M. Spiecker, P. Paluch, N. Gosling, N. Drucker, S. Matityahu, D. Gusenkova, S. Günzler, D. Rieger, I. Takmakov, F. Valenti, P. Winkel, R. Gebauer, O. Sander, G. Catelani, A. Shnirman, A. V. Ustinov, W. Wernsdorfer, Y. Cohen, and I. M. Pop, "Two-level system hyperpolarization using a quantum Szilard engine", Nat. Phys. **19**, 1–6 (2023).

[8] D. Gusenkova, F. Valenti, M. Spiecker, S. Günzler, P. Paluch, D. Rieger, L.-M. Pioraş-Ţimbolmaş, L. P. Zârbo, N. Casali, I. Colantoni, A. Cruciani, S. Pirro, L. Cardani, A. Petrescu, W. Wernsdorfer, P. Winkel, and I. M. Pop, "Operating in a deep underground facility improves the locking of gradiometric fluxonium qubits at the sweet spots", Appl. Phys. Lett. **120**, 054001 (2022).

[9] D. Gusenkova, M. Spiecker, R. Gebauer, M. Willsch, D. Willsch, F. Valenti, N. Karcher, L. Grünhaupt, I. Takmakov, P. Winkel, D. Rieger, A. V. Ustinov, N. Roch, W. Wernsdorfer, K. Michielsen, O. Sander, and I. M. Pop, "Quantum Nondemolition Dispersive Readout of a Superconducting Artificial Atom Using Large Photon Numbers", Phys. Rev. Appl. **15**, 064030 (2021).

[10] I. Takmakov, P. Winkel, F. Foroughi, L. Planat, D. Gusenkova, M. Spiecker, D. Rieger, L. Grünhaupt, A. V. Ustinov, W. Wernsdorfer, I. M. Pop, and N. Roch, "Minimizing the Discrimination Time for Quantum States of an Artificial Atom", Phys. Rev. Appl. **15**, 064029 (2021).

[11] R. P. Feynman, "Simulating physics with computers", Int. J. Theor. Phys. **21**, 467–488 (1982).

[12] J. Preskill, "Quantum computing: pro and con", Proc. R. Soc. Lond. A. **454**, 469–486 (1998).

[13] C. P. Williams, *Explorations in Quantum Computing* (Springer, London, England, UK, 2011).

[14] Y. Cao, J. Romero, J. P. Olson, M. Degroote, P. D. Johnson, M. Kieferová, I. D. Kivlichan, T. Menke, B. Peropadre, N. P. D. Sawaya, S. Sim, L. Veis, and A. Aspuru-Guzik, "Quantum Chemistry in the Age of Quantum Computing", Chem. Rev. **119**, 10856–10915 (2019).

[15] R. Orús, S. Mugel, and E. Lizaso, "Quantum computing for finance: Overview and prospects", Rev. Phys. **4**, 100028 (2019).

[16] S. McArdle, S. Endo, A. Aspuru-Guzik, S. C. Benjamin, and X. Yuan, "Quantum computational chemistry", Rev. Mod. Phys. **92**, 015003 (2020).

[17] A. Papageorgiou and J. F. Traub, "Measures of quantum computing speedup", Phys. Rev. A **88**, 022316 (2013).

[18] J. Preskill, "Quantum Computing in the NISQ era and beyond", Quantum **2**, 79 (2018).

[19] F. Arute, K. Arya, R. Babbush, D. Bacon, J. C. Bardin, R. Barends, R. Biswas, S. Boixo, F. G. S. L. Brandao, D. A. Buell, ..., K. J. Sung, M. D. Trevithick, A. Vainsencher, B. Villalonga, T. White, Z. J. Yao, P. Yeh, A. Zalcman, H. Neven, and J. M. Martinis, "Quantum supremacy using a programmable superconducting processor", Nature **574**, 505–510 (2019).

[20] K. Bharti, A. Cervera-Lierta, T. H. Kyaw, T. Haug, S. Alperin-Lea, A. Anand, M. Degroote, H. Heimonen, J. S. Kottmann, T. Menke, W.-K. Mok, S. Sim, L.-C. Kwek, and A. Aspuru-Guzik, "Noisy intermediate-scale quantum algorithms", Rev. Mod. Phys. **94**, 015004 (2022).

[21] Y. Kim, A. Eddins, S. Anand, K. X. Wei, E. van den Berg, S. Rosenblatt, H. Nayfeh, Y. Wu, M. Zaletel, K. Temme, and A. Kandala, "Evidence for the utility of quantum computing before fault tolerance", Nature **618**, 500–505 (2023).

[22] P. W. Shor, "Algorithms for quantum computation: discrete logarithms and factoring", in Proceedings 35th Annual Symposium on Foundations of Computer Science (1994), pp. 124–134.

[23] P. W. Shor, "Polynomial-time algorithms for prime factorization and discrete logarithms on a quantum computer", SIAM Journal on Computing **26**, 1484–1509 (1997).

[24] L. K. Grover, "A fast quantum mechanical algorithm for database search", in STOC '96: Proceedings of the twenty-eighth annual ACM symposium on Theory of Computing (July 1996), pp. 212–219.

[25] E. Pednault, J. A. Gunnels, G. Nannicini, L. Horesh, and R. Wisnieff, "Leveraging Secondary Storage to Simulate Deep 54-qubit Sycamore Circuits", arXiv, `10.48550/arXiv.1910.09534` (2019).

[26] E. M. Stoudenmire and X. Waintal, "Grover's Algorithm Offers No Quantum Advantage", arXiv, `10.48550/arXiv.2303.11317` (2023).

[27] S. Aaronson, *Of course Grover's algorithm offers a quantum advantage!*, (2023) `https://scottaaronson.blog/?p=7143` (visited on 10/13/2023).

[28] D. P. DiVincenzo, "The Physical Implementation of Quantum Computation", Fortschr. Phys. **48**, 771–783 (2000).

[29] J. Benhelm, G. Kirchmair, C. F. Roos, and R. Blatt, "Towards fault-tolerant quantum computing with trapped ions", Nat. Phys. **4**, 463–466 (2008).

[30] R. Blatt and C. F. Roos, "Quantum simulations with trapped ions", Nat. Phys. **8**, 277–284 (2012).

[31] E. Knill, R. Laflamme, and G. J. Milburn, "A scheme for efficient quantum computation with linear optics", Nature **409**, 46–52 (2001).

[32] P. Kok, W. J. Munro, K. Nemoto, T. C. Ralph, J. P. Dowling, and G. J. Milburn, "Linear optical quantum computing with photonic qubits", Rev. Mod. Phys. **79**, 135–174 (2007).

[33] J. R. Petta, A. C. Johnson, J. M. Taylor, E. A. Laird, A. Yacoby, M. D. Lukin, C. M. Marcus, M. P. Hanson, and A. C. Gossard, "Coherent Manipulation of Coupled Electron Spins in Semiconductor Quantum Dots", Science **309**, 2180–2184 (2005).

[34] L. M. K. Vandersypen and M. A. Eriksson, "Quantum computing with semiconductor spins", Phys. Today **72**, 38–45 (2019).

[35] G. Aromí, D. Aguilà, P. Gamez, F. Luis, and O. Roubeau, "Design of magnetic coordination complexes for quantum computing", Chem. Soc. Rev. **41**, 537–546 (2012).

[36] A. Gaita-Ariño, F. Luis, S. Hill, and E. Coronado, "Molecular spins for quantum computation", Nat. Chem. **11**, 301–309 (2019).

[37] S. Carretta, D. Zueco, A. Chiesa, Á. Gómez-León, and F. Luis, "A perspective on scaling up quantum computation with molecular spins", Appl. Phys. Lett. **118**, `10.1063/5.0053378` (2021).

[38] R. Barends, J. Kelly, A. Megrant, A. Veitia, D. Sank, E. Jeffrey, T. C. White, J. Mutus, A. G. Fowler, B. Campbell, Y. Chen, Z. Chen, B. Chiaro, A. Dunsworth, C. Neill, P. O'Malley, P. Roushan, A. Vainsencher, J. Wenner, A. N. Korotkov, A. N. Cleland, and J. M. Martinis, "Superconducting quantum circuits at the surface code threshold for fault tolerance", Nature **508**, 500–503 (2014).

[39] C. K. Andersen, A. Remm, S. Lazar, S. Krinner, N. Lacroix, G. J. Norris, M. Gabureac, C. Eichler, and A. Wallraff, "Repeated quantum error detection in a surface code", Nat. Phys. **16**, 875–880 (2020).

[40] J. F. Marques, B. M. Varbanov, M. S. Moreira, H. Ali, N. Muthusubramanian, C. Zachariadis, F. Battistel, M. Beekman, N. Haider, W. Vlothuizen, A. Bruno, B. M. Terhal, and L. DiCarlo, "Logical-qubit operations in an error-detecting surface code", Nat. Phys. **18**, 80–86 (2022).

[41] S. Krinner, N. Lacroix, A. Remm, A. Di Paolo, E. Genois, C. Leroux, C. Hellings, S. Lazar, F. Swiadek, J. Herrmann, G. J. Norris, C. K. Andersen, M. Müller, A. Blais, C. Eichler, and A. Wallraff, "Realizing repeated quantum error correction in a distance-three surface code", Nature **605**, 669–674 (2022).

[42] V. V. Sivak, A. Eickbusch, B. Royer, S. Singh, I. Tsioutsios, S. Ganjam, A. Miano, B. L. Brock, A. Z. Ding, L. Frunzio, S. M. Girvin, R. J. Schoelkopf, and M. H. Devoret, "Real-time quantum error correction beyond break-even", Nature **616**, 50–55 (2023).

[43] I. Siddiqi, "Engineering high-coherence superconducting qubits", Nat. Rev. Mater. **6**, 875–891 (2021).

[44] K. D. Petersson, L. W. McFaul, M. D. Schroer, M. Jung, J. M. Taylor, A. A. Houck, and J. R. Petta, "Circuit quantum electrodynamics with a spin qubit", Nature **490**, 380–383 (2012).

[45] O. Arcizet, V. Jacques, A. Siria, P. Poncharal, P. Vincent, and S. Seidelin, "A single nitrogen-vacancy defect coupled to a nanomechanical oscillator", Nat. Phys. **7**, 879–883 (2011).

[46] M. Bild, M. Fadel, Y. Yang, U. von Lüpke, P. Martin, A. Bruno, and Y. Chu, "Schrödinger cat states of a 16-microgram mechanical oscillator", Science **380**, 274–278 (2023).

[47] A. Bienfait, J. J. Pla, Y. Kubo, M. Stern, X. Zhou, C. C. Lo, C. D. Weis, T. Schenkel, M. L. W. Thewalt, D. Vion, D. Esteve, B. Julsgaard, K. Mølmer, J. J. L. Morton, and P. Bertet, "Reaching the quantum limit of sensitivity in electron spin resonance", Nat. Nanotechnol. **11**, 253–257 (2016).

[48] I. Gimeno, W. Kersten, M. C. Pallarés, P. Hermosilla, M. J. Martínez-Pérez, M. D. Jenkins, A. Angerer, C. Sánchez-Azqueta, D. Zueco, J. Majer, A. Lostao, and F. Luis, "Enhanced Molecular Spin-Photon Coupling at Superconducting Nanoconstrictions", ACS Nano **14**, 8707–8715 (2020).

[49] E. Albertinale, L. Balembois, E. Billaud, V. Ranjan, D. Flanigan, T. Schenkel, D. Estève, D. Vion, P. Bertet, and E. Flurin, "Detecting spins by their fluorescence with a microwave photon counter", Nature **600**, 434–438 (2021).

[50] Z. Wang, L. Balembois, M. Rančić, E. Billaud, M. Le Dantec, A. Ferrier, P. Goldner, S. Bertaina, T. Chanelière, D. Esteve, D. Vion, P. Bertet, and E. Flurin, "Single-electron spin resonance detection by microwave photon counting", Nature **619**, 276–281 (2023).

[51] M. Devoret, "Quantum fluctuations in electrical circuits, Les houches session lxiii", in *Quantum fluctuations*, Vol. 63 (Elsevier, 1997).

[52] U. Vool and M. Devoret, "Introduction to quantum electromagnetic circuits", Int. J. Circuit Theory Appl. **45**, 897–934 (2017).

[53] B. D. Josephson, "Possible new effects in superconductive tunnelling", Physics Letters **1**, 251–253 (1962).

[54] B. D. Josephson, "Coupled Superconductors", Rev. Mod. Phys. **36**, 216–220 (1964).

[55] B. D. Josephson, "Supercurrents through barriers", Adv. Phys. **14**, 419–451 (1965).

[56] A. A. Golubov, M. Y. Kupriyanov, and E. Il'ichev, "The current-phase relation in Josephson junctions", Rev. Mod. Phys. **76**, 411–469 (2004).

[57] A. Shnirman, G. Schön, and Z. Hermon, "Quantum Manipulations of Small Josephson Junctions", Phys. Rev. Lett. **79**, 2371–2374 (1997).

[58] V. Bouchiat, D. Vion, P. Joyez, D. Esteve, and M. H. Devoret, "Quantum coherence with a single Cooper pair", Phys. Scr. **1998**, 165 (1998).

[59] Y. Nakamura, Y. A. Pashkin, and J. S. Tsai, "Coherent control of macroscopic quantum states in a single-Cooper-pair box", Nature **398**, 786–788 (1999).

[60] J. Koch, T. M. Yu, J. Gambetta, A. A. Houck, D. I. Schuster, J. Majer, A. Blais, M. H. Devoret, S. M. Girvin, and R. J. Schoelkopf, "Charge-insensitive qubit design derived from the Cooper pair box", Phys. Rev. A **76**, 042319 (2007).

[61] D. Vion, A. Aassime, A. Cottet, P. Joyez, H. Pothier, C. Urbina, D. Esteve, and M. H. Devoret, "Manipulating the Quantum State of an Electrical Circuit", Science **296**, 886–889 (2002).

[62] M. Metcalfe, E. Boaknin, V. Manucharyan, R. Vijay, I. Siddiqi, C. Rigetti, L. Frunzio, R. J. Schoelkopf, and M. H. Devoret, "Measuring the decoherence of a quantronium qubit with the cavity bifurcation amplifier", Phys. Rev. B **76**, 174516 (2007).

[63] Y. Wu, W.-S. Bao, S. Cao, F. Chen, M.-C. Chen, X. Chen, T.-H. Chung, H. Deng, Y. Du, D. Fan, . . ., K. Zhang, Y. Zhang, H. Zhao, Y. Zhao, L. Zhou, Q. Zhu, C.-Y. Lu, C.-Z. Peng, X. Zhu, and J.-W. Pan, "Strong Quantum Computational Advantage Using a Superconducting Quantum Processor", Phys. Rev. Lett. **127**, 180501 (2021).

[64] A. D. King, J. Raymond, T. Lanting, R. Harris, A. Zucca, F. Altomare, A. J. Berkley, K. Boothby, S. Ejtemaee, C. Enderud, E. Hoskinson, S. Huang, E. Ladizinsky, A. J. R. MacDonald, G. Marsden, R. Molavi, T. Oh, G. Poulin-Lamarre, M. Reis, C. Rich, Y. Sato, N. Tsai, M. Volkmann, J. D. Whittaker, J. Yao, A. W. Sandvik, and M. H. Amin, "Quantum critical dynamics in a 5,000-qubit programmable spin glass", Nature **617**, 61–66 (2023).

[65] A. P. M. Place, L. V. H. Rodgers, P. Mundada, B. M. Smitham, M. Fitzpatrick, Z. Leng, A. Premkumar, J. Bryon, A. Vrajitoarea, S. Sussman, G. Cheng, T. Madhavan, H. K. Babla, X. H. Le, Y. Gang, B. Jäck, A. Gyenis, N. Yao, R. J. Cava, N. P. de Leon, and A. A. Houck, "New material platform for superconducting transmon qubits with coherence times exceeding 0.3 milliseconds", Nat. Commun. **12**, 1–6 (2021).

[66] C. Wang, X. Li, H. Xu, Z. Li, J. Wang, Z. Yang, Z. Mi, X. Liang, T. Su, C. Yang, G. Wang, W. Wang, Y. Li, M. Chen, C. Li, K. Linghu, J. Han, Y. Zhang, Y. Feng, Y. Song, T. Ma, J. Zhang, R. Wang, P. Zhao, W. Liu, G. Xue, Y. Jin, and H. Yu, "Towards practical quantum computers: transmon qubit with a lifetime approaching 0.5 milliseconds", npj Quantum Inf. **8**, 1–6 (2022).

[67] V. E. Manucharyan, J. Koch, L. I. Glazman, and M. H. Devoret, "Fluxonium: Single Cooper-Pair Circuit Free of Charge Offsets", Science **326**, 113–116 (2009).

[68] G. Rastelli, I. M. Pop, and F. W. J. Hekking, "Quantum phase slips in Josephson junction rings", Phys. Rev. B **87**, 174513 (2013).

[69] K. N. Nesterov, I. V. Pechenezhskiy, C. Wang, V. E. Manucharyan, and M. G. Vavilov, "Microwave-activated controlled-Z gate for fixed-frequency fluxonium qubits", Phys. Rev. A **98**, 030301 (2018).

[70] F. Bao, H. Deng, D. Ding, R. Gao, X. Gao, C. Huang, X. Jiang, H.-S. Ku, Z. Li, X. Ma, X. Ni, J. Qin, Z. Song, H. Sun, C. Tang, T. Wang, F. Wu, T. Xia, W. Yu, F. Zhang, G. Zhang, X. Zhang, J. Zhou, X. Zhu, Y. Shi, J. Chen, H.-H. Zhao, and C. Deng, "Fluxonium: An Alternative Qubit Platform for High-Fidelity Operations", Phys. Rev. Lett. **129**, 010502 (2022).

[71] I. Chiorescu, P. Bertet, K. Semba, Y. Nakamura, C. J. P. M. Harmans, and J. E. Mooij, "Coherent dynamics of a flux qubit coupled to a harmonic oscillator", Nature **431**, 159–162 (2004).

[72] F. Yoshihara, K. Harrabi, A. O. Niskanen, Y. Nakamura, and J. S. Tsai, "Decoherence of Flux Qubits due to $1/f$ Flux Noise", Phys. Rev. Lett. **97**, 167001 (2006).

[73] F. Yan, S. Gustavsson, A. Kamal, J. Birenbaum, A. P. Sears, D. Hover, T. J. Gudmundsen, D. Rosenberg, G. Samach, S. Weber, J. L. Yoder, T. P. Orlando, J. Clarke, A. J. Kerman, and W. D. Oliver, "The flux qubit revisited to enhance coherence and reproducibility", Nat. Commun. **7**, 1–9 (2016).

[74] A. Somoroff, Q. Ficheux, R. A. Mencia, H. Xiong, R. Kuzmin, and V. E. Manucharyan, "Millisecond Coherence in a Superconducting Qubit", Phys. Rev. Lett. **130**, 267001 (2023).

[75] T. M. Hazard, A. Gyenis, A. Di Paolo, A. T. Asfaw, S. A. Lyon, A. Blais, and A. A. Houck, "Nanowire Superinductance Fluxonium Qubit", Phys. Rev. Lett. **122**, 010504 (2019).

[76] R. Gao, H.-S. Ku, H. Deng, W. Yu, T. Xia, F. Wu, Z. Song, M. Wang, X. Miao, C. Zhang, Y. Lin, Y. Shi, H.-H. Zhao, and C. Deng, "Ultrahigh Kinetic Inductance Superconducting Materials from Spinodal Decomposition", Adv. Mater. **34**, 2201268 (2022).

[77] H. Sun, F. Wu, H.-S. Ku, X. Ma, J. Qin, Z. Song, T. Wang, G. Zhang, J. Zhou, Y. Shi, H.-H. Zhao, and C. Deng, "Characterization of Loss Mechanisms in a Fluxonium Qubit", Phys. Rev. Appl. **20**, 034016 (2023).

[78] L. Grünhaupt, M. Spiecker, D. Gusenkova, N. Maleeva, S. T. Skacel, I. Takmakov, F. Valenti, P. Winkel, H. Rotzinger, W. Wernsdorfer, A. V. Ustinov, and I. M. Pop, "Granular aluminium as a superconducting material for high-impedance quantum circuits", Nat. Mater. **18**, 816–819 (2019).

[79] N. A. Masluk, I. M. Pop, A. Kamal, Z. K. Minev, and M. H. Devoret, "Microwave Characterization of Josephson Junction Arrays: Implementing a Low Loss Superinductance", Phys. Rev. Lett. **109**, 137002 (2012).

[80] M. Peruzzo, A. Trioni, F. Hassani, M. Zemlicka, and J. M. Fink, "Surpassing the Resistance Quantum with a Geometric Superinductor", Phys. Rev. Appl. **14**, 044055 (2020).

[81] M. Peruzzo, F. Hassani, G. Szep, A. Trioni, E. Redchenko, M. Žemlička, and J. M. Fink, "Geometric Superinductance Qubits: Controlling Phase Delocalization across a Single Josephson Junction", PRX Quantum **2**, 040341 (2021).

[82] L. B. Nguyen, G. Koolstra, Y. Kim, A. Morvan, T. Chistolini, S. Singh, K. N. Nesterov, C. Jünger, L. Chen, Z. Pedramrazi, B. K. Mitchell, J. M. Kreikebaum, S. Puri, D. I. Santiago, and I. Siddiqi, "Blueprint for a High-Performance Fluxonium Quantum Processor", PRX Quantum **3**, 037001 (2022).

[83] S. Haroche and J.-M. Raimond, *Exploring the Quantum: Atoms, Cavities, and Photons (Oxford Graduate Texts)* (OXFORD UNIV PR, Oxford, England, UK, Oct. 2006).

[84] A. Wallraff, D. I. Schuster, A. Blais, L. Frunzio, R. S. Huang, J. Majer, S. Kumar, S. M. Girvin, and R. J. Schoelkopf, "Strong coupling of a single photon to a superconducting qubit using circuit quantum electrodynamics", Nature **431**, 162–167 (2004).

[85] A. Blais, R.-S. Huang, A. Wallraff, S. M. Girvin, and R. J. Schoelkopf, "Cavity quantum electrodynamics for superconducting electrical circuits: An architecture for quantum computation", Phys. Rev. A **69**, 062320 (2004).

[86] E. Jeffrey, D. Sank, J. Y. Mutus, T. C. White, J. Kelly, R. Barends, Y. Chen, Z. Chen, B. Chiaro, A. Dunsworth, A. Megrant, P. J. J. O'Malley, C. Neill, P. Roushan, A. Vainsencher, J. Wenner, A. N. Cleland, and J. M. Martinis, "Fast Accurate State Measurement with Superconducting Qubits", Phys. Rev. Lett. **112**, 190504 (2014).

[87] P. Krantz, A. Bengtsson, M. Simoen, S. Gustavsson, V. Shumeiko, W. D. Oliver, C. M. Wilson, P. Delsing, and J. Bylander, "Single-shot read-out of a superconducting qubit using a Josephson parametric oscillator", Nat. Commun. **7**, 1–8 (2016).

[88] T. Walter, P. Kurpiers, S. Gasparinetti, P. Magnard, A. Potočnik, Y. Salathé, M. Pechal, M. Mondal, M. Oppliger, C. Eichler, and A. Wallraff, "Rapid High-Fidelity Single-Shot Dispersive Readout of Superconducting Qubits", Phys. Rev. Appl. **7**, 054020 (2017).

[89] R. Gebauer, N. Karcher, D. Gusenkova, M. Spiecker, L. Grünhaupt, I. Takmakov, P. Winkel, L. Planat, N. Roch, W. Wernsdorfer, A. V. Ustinov, M. Weber, M. Weides, I. M. Pop, and O. Sander, "State preparation of a fluxonium qubit with feedback from a custom FPGA-based platform", AIP Conf. Proc. **2241**, `10.1063/5.0011721` (2020).

[90] L. Chen, H.-X. Li, Y. Lu, C. W. Warren, C. J. Križan, S. Kosen, M. Rommel, S. Ahmed, A. Osman, J. Biznárová, A. Fadavi Roudsari, B. Lienhard, M. Caputo, K. Grigoras, L. Grönberg, J. Govenius, A. F. Kockum, P. Delsing, J. Bylander, and G. Tancredi, "Transmon qubit readout fidelity at the threshold for quantum error correction without a quantum-limited amplifier", npj Quantum Inf. **9**, 1–7 (2023).

[91] M. Boissonneault, J. M. Gambetta, and A. Blais, "Dispersive regime of circuit QED: Photon-dependent qubit dephasing and relaxation rates", Phys. Rev. A **79**, 013819 (2009).

[92] D. Sank, Z. Chen, M. Khezri, J. Kelly, R. Barends, B. Campbell, Y. Chen, B. Chiaro, A. Dunsworth, A. Fowler, E. Jeffrey, E. Lucero, A. Megrant, J. Mutus, M. Neeley, C. Neill, P. J. J. O'Malley, C. Quintana, P. Roushan, A. Vainsencher, T. White, J. Wenner, A. N. Korotkov, and J. M. Martinis, "Measurement-Induced State Transitions in a Superconducting Qubit: Beyond the Rotating Wave Approximation", Phys. Rev. Lett. **117**, 190503 (2016).

[93] Z. K. Minev, S. O. Mundhada, S. Shankar, P. Reinhold, R. Gutiérrez-Jáuregui, R. J. Schoelkopf, M. Mirrahimi, H. J. Carmichael, and M. H. Devoret, "To catch and reverse a quantum jump mid-flight", Nature **570**, 200–204 (2019).

[94] M. Khezri, A. Opremcak, Z. Chen, A. Bengtsson, T. White, O. Naaman, R. Acharya, K. Anderson, M. Ansmann, F. Arute, . . . , Z. J. Yao, P. Yeh, J. Yoo, G. Young, N. Zhu, N. Zobrist, D. Sank, A. Korotkov, Y. Chen, and V. Smelyanskiy, "Measurement-Induced State Transitions in a Superconducting Qubit: Within the Rotating Wave Approximation", arXiv, `10.48550/arXiv.2212.05097` (2022).

[95] A. Petrescu, M. Malekakhlagh, and H. E. Türeci, "Lifetime renormalization of driven weakly anharmonic superconducting qubits. II. The readout problem", Phys. Rev. B **101**, 134510 (2020).

[96] R. Shillito, A. Petrescu, J. Cohen, J. Beall, M. Hauru, M. Ganahl, A. G. M. Lewis, G. Vidal, and A. Blais, "Dynamics of Transmon Ionization", Phys. Rev. Appl. **18**, 034031 (2022).

[97] J. Cohen, A. Petrescu, R. Shillito, and A. Blais, "Reminiscence of Classical Chaos in Driven Transmons", PRX Quantum **4**, 020312 (2023).

[98] J. T. Muhonen, J. P. Dehollain, A. Laucht, F. E. Hudson, R. Kalra, T. Sekiguchi, K. M. Itoh, D. N. Jamieson, J. C. McCallum, A. S. Dzurak, and A. Morello, "Storing quantum information for 30 seconds in a nanoelectronic device", Nat. Nanotechnol. **9**, 986–991 (2014).

[99] M. Zhong, M. P. Hedges, R. L. Ahlefeldt, J. G. Bartholomew, S. E. Beavan, S. M. Wittig, J. J. Longdell, and M. J. Sellars, "Optically addressable nuclear spins in a solid with a six-hour coherence time", Nature **517**, 177–180 (2015).

[100] R. Vincent, S. Klyatskaya, M. Ruben, W. Wernsdorfer, and F. Balestro, "Electronic read-out of a single nuclear spin using a molecular spin transistor", Nature **488**, 357–360 (2012).

[101] L. Bogani, C. Danieli, E. Biavardi, N. Bendiab, A.-L. Barra, E. Dalcanale, W. Wernsdorfer, and A. Cornia, "Single-Molecule-Magnet Carbon-Nanotube Hybrids", Angew. Chem. Int. Ed. **48**, 746–750 (2009).

[102] P. Willke, W. Paul, F. D. Natterer, K. Yang, Y. Bae, T. Choi, J. Fernández-Rossier, A. J. Heinrich, and C. P. Lutz, "Probing quantum coherence in single-atom electron spin resonance", Sci. Adv. **4**, `10.1126/sciadv.aaq1543` (2018).

[103] Y. Kubo, F. R. Ong, P. Bertet, D. Vion, V. Jacques, D. Zheng, A. Dréau, J.-F. Roch, A. Auffeves, F. Jelezko, J. Wrachtrup, M. F. Barthe, P. Bergonzo, and D. Esteve, "Strong Coupling of a Spin Ensemble to a Superconducting Resonator", Phys. Rev. Lett. **105**, 140502 (2010).

[104] Y. Kubo, C. Grezes, A. Dewes, T. Umeda, J. Isoya, H. Sumiya, N. Morishita, H. Abe, S. Onoda, T. Ohshima, V. Jacques, A. Dréau, J.-F. Roch, I. Diniz, A. Auffeves, D. Vion, D. Esteve, and P. Bertet, "Hybrid Quantum Circuit with a Superconducting Qubit Coupled to a Spin Ensemble", Phys. Rev. Lett. **107**, 220501 (2011).

[105] S. Weichselbaumer, P. Natzkin, C. W. Zollitsch, M. Weiler, R. Gross, and H. Huebl, "Quantitative Modeling of Superconducting Planar Resonators for Electron Spin Resonance", Phys. Rev. Appl. **12**, 024021 (2019).

[106] S. Probst, A. Bienfait, P. Campagne-Ibarcq, J. J. Pla, B. Albanese, J. F. Da Silva Barbosa, T. Schenkel, D. Vion, D. Esteve, K. Mølmer, J. J. L. Morton, R. Heeres, and P. Bertet, "Inductive-detection electron-spin resonance spectroscopy with 65 spins/Hz sensitivity", Appl. Phys. Lett. **111**, `10.1063/1.5002540` (2017).

[107] N. Didier, J. Bourassa, and A. Blais, "Fast Quantum Nondemolition Readout by Parametric Modulation of Longitudinal Qubit-Oscillator Interaction", Phys. Rev. Lett. **115**, 203601 (2015).

[108] S. Richer and D. DiVincenzo, "Circuit design implementing longitudinal coupling: A scalable scheme for superconducting qubits", Phys. Rev. B **93**, 134501 (2016).

[109] A. Schneider, T. Wolz, M. Pfirrmann, M. Spiecker, H. Rotzinger, A. V. Ustinov, and M. Weides, "Transmon qubit in a magnetic field: Evolution of coherence and transition frequency", Phys. Rev. Res. **1**, 023003 (2019).

[110] J. Krause, C. Dickel, E. Vaal, M. Vielmetter, J. Feng, R. Bounds, G. Catelani, J. M. Fink, and Y. Ando, "Magnetic Field Resilience of Three-Dimensional Transmons with Thin-Film Al/AlO$_x$/Al Josephson Junctions Approaching 1 T", Phys. Rev. Appl. **17**, 034032 (2022).

[111] G. J. Grabovskij, L. J. Swenson, O. Buisson, C. Hoffmann, A. Monfardini, and J.-C. Villégier, "In situ measurement of the permittivity of helium using microwave NbN resonators", Appl. Phys. Lett. **93**, `10.1063/1.2996263` (2008).

[112] J. Luomahaara, V. Vesterinen, L. Grönberg, and J. Hassel, "Kinetic inductance magnetometer", Nat. Commun. **5**, 1–7 (2014).

[113] C. W. Zollitsch, J. O'Sullivan, O. Kennedy, G. Dold, and J. J. L. Morton, "Tuning high-Q superconducting resonators by magnetic field reorientation", AIP Adv. **9**, 10.1063/1.5129032 (2019).

[114] D. Niepce, J. Burnett, and J. Bylander, "High Kinetic Inductance NbN Nanowire Superinductors", Phys. Rev. Appl. **11**, 044014 (2019).

[115] N. Samkharadze, A. Bruno, P. Scarlino, G. Zheng, D. P. DiVincenzo, L. DiCarlo, and L. M. K. Vandersypen, "High-Kinetic-Inductance Superconducting Nanowire Resonators for Circuit QED in a Magnetic Field", Phys. Rev. Appl. **5**, 044004 (2016).

[116] J. G. Kroll, F. Borsoi, K. L. van der Enden, W. Uilhoorn, D. de Jong, M. Quintero-Pérez, D. J. van Woerkom, A. Bruno, S. R. Plissard, D. Car, E. P. A. M. Bakkers, M. C. Cassidy, and L. P. Kouwenhoven, "Magnetic-Field-Resilient Superconducting Coplanar-Waveguide Resonators for Hybrid Circuit Quantum Electrodynamics Experiments", Phys. Rev. Appl. **11**, 064053 (2019).

[117] M. R. Vissers, J. Gao, D. S. Wisbey, D. A. Hite, C. C. Tsuei, A. D. Corcoles, M. Steffen, and D. P. Pappas, "Low loss superconducting titanium nitride coplanar waveguide resonators", Appl. Phys. Lett. **97**, 10.1063/1.3517252 (2010).

[118] H. G. Leduc, B. Bumble, P. K. Day, B. H. Eom, J. Gao, S. Golwala, B. A. Mazin, S. McHugh, A. Merrill, D. C. Moore, O. Noroozian, A. D. Turner, and J. Zmuidzinas, "Titanium nitride films for ultrasensitive microresonator detectors", Appl. Phys. Lett. **97**, 102509 (2010).

[119] A. Shearrow, G. Koolstra, S. J. Whiteley, N. Earnest, P. S. Barry, F. J. Heremans, D. D. Awschalom, E. Shirokoff, and D. I. Schuster, "Atomic layer deposition of titanium nitride for quantum circuits", Appl. Phys. Lett. **113**, 10.1063/1.5053461 (2018).

[120] O. Dupré, A. Benoît, M. Calvo, A. Catalano, J. Goupy, C. Hoarau, T. Klein, K. Le Calvez, B. Sacépé, A. Monfardini, and F. Levy-Bertrand, "Tunable sub-gap radiation detection with superconducting resonators", Supercond. Sci. Technol. **30**, 045007 (2017).

[121] R. W. Cohen and B. Abeles, "Superconductivity in Granular Aluminum Films", Phys. Rev. **168**, 444–450 (1968).

[122] G. Deutscher, H. Fenichel, M. Gershenson, E. Grünbaum, and Z. Ovadyahu, "Transition to zero dimensionality in granular aluminum superconducting films", J. Low Temp. Phys. **10**, 231–243 (1973).

[123] F. Levy-Bertrand, T. Klein, T. Grenet, O. Dupré, A. Benoît, A. Bideaud, O. Bourrion, M. Calvo, A. Catalano, A. Gomez, J. Goupy, L. Grünhaupt, U. v. Luepke, N. Maleeva, F. Valenti, I. M. Pop, and A. Monfardini, "Electrodynamics of granular aluminum from superconductor to insulator: Observation of collective superconducting modes", Phys. Rev. B **99**, 094506 (2019).

[124] H. Rotzinger, S. T. Skacel, M. Pfirrmann, J. N. Voss, J. Münzberg, S. Probst, P. Bushev, M. P. Weides, A. V. Ustinov, and J. E. Mooij, "Aluminium-oxide wires for superconducting high kinetic inductance circuits", Supercond. Sci. Technol. **30**, 025002 (2016).

[125] L. Grünhaupt, N. Maleeva, S. T. Skacel, M. Calvo, F. Levy-Bertrand, A. V. Ustinov, H. Rotzinger, A. Monfardini, G. Catelani, and I. M. Pop, "Loss Mechanisms and Quasiparticle Dynamics in Superconducting Microwave Resonators Made of Thin-Film Granular Aluminum", Phys. Rev. Lett. **121**, 117001 (2018).

[126] W. Zhang, K. Kalashnikov, W.-S. Lu, P. Kamenov, T. DiNapoli, and M. E. Gershenson, "Microresonators Fabricated from High-Kinetic-Inductance Aluminum Films", Phys. Rev. Appl. **11**, 011003 (2019).

[127] P. Kamenov, W.-S. Lu, K. Kalashnikov, T. DiNapoli, M. T. Bell, and M. E. Gershenson, "Granular Aluminum Meandered Superinductors for Quantum Circuits", Phys. Rev. Appl. **13**, 054051 (2020).

[128] G. Deutscher and S. A. Dodds, "Critical-field anisotropy and fluctuation conductivity in granular aluminum films", Phys. Rev. B **16**, 3936–3942 (1977).

[129] T. Chui, P. Lindenfeld, W. L. McLean, and K. Mui, "Coupling and isolation: Critical field and transition temperature of superconducting granular aluminum", Phys. Rev. B **24**, 6728–6731 (1981).

[130] F. Valenti, F. Henriques, G. Catelani, N. Maleeva, L. Grünhaupt, U. von Lüpke, S. T. Skacel, P. Winkel, A. Bilmes, A. V. Ustinov, J. Goupy, M. Calvo, A. Benoît, F. Levy-Bertrand, A. Monfardini, and I. M. Pop, "Interplay Between Kinetic Inductance, Nonlinearity, and Quasiparticle Dynamics in Granular Aluminum Microwave Kinetic Inductance Detectors", Phys. Rev. Appl. **11**, 054087 (2019).

[131] D. C. Mattis and J. Bardeen, "Theory of the Anomalous Skin Effect in Normal and Superconducting Metals", Phys. Rev. **111**, 412–417 (1958).

[132] A. J. Annunziata, D. F. Santavicca, L. Frunzio, G. Catelani, M. J. Rooks, A. Frydman, and D. E. Prober, "Tunable superconducting nanoinductors", Nanotechnology **21**, 445202 (2010).

[133] S. E. de Graaf, A. A. Adamyan, T. Lindström, D. Erts, S. E. Kubatkin, A. Y. Tzalenchuk, and A. V. Danilov, "Direct Identification of Dilute Surface Spins on Al_2O_3: Origin of Flux Noise in Quantum Circuits", Phys. Rev. Lett. **118**, 057703 (2017).

[134] J. H. Ungerer, D. Sarmah, A. Kononov, J. Ridderbos, R. Haller, L. Y. Cheung, and C. Schönenberger, "Performance of high impedance resonators in dirty dielectric environments", arXiv, `10.48550/arXiv.2302.06303` (2023).

[135] H. Wang, C. Shi, J. Hu, S. Han, C. C. Yu, and R. Q. Wu, "Candidate Source of Flux Noise in SQUIDs: Adsorbed Oxygen Molecules", Phys. Rev. Lett. **115**, 077002 (2015).

[136] P. Kumar, S. Sendelbach, M. A. Beck, J. W. Freeland, Z. Wang, H. Wang, C. C. Yu, R. Q. Wu, D. P. Pappas, and R. McDermott, "Origin and Reduction of $1/f$ Magnetic Flux Noise in Superconducting Devices", Phys. Rev. Appl. **6**, 041001 (2016).

[137] S. E. de Graaf, L. Faoro, L. B. Ioffe, S. Mahashabde, J. J. Burnett, T. Lindström, S. E. Kubatkin, A. V. Danilov, and A. Y. Tzalenchuk, "Two-level systems in superconducting quantum devices due to trapped quasiparticles", Sci. Adv. **6**, `10.1126/sciadv.abc5055` (2020).

[138] F. Yang, T. Gozlinski, T. Storbeck, L. Grünhaupt, I. M. Pop, and W. Wulfhekel, "Microscopic charging and in-gap states in superconducting granular aluminum", Phys. Rev. B **102**, 104502 (2020).

[139] B. Ho Eom, P. K. Day, H. G. LeDuc, and J. Zmuidzinas, "A wideband, low-noise superconducting amplifier with high dynamic range", Nat. Phys. **8**, 623–627 (2012).

[140] F. Friedrich, P. Winkel, K. Borisov, H. Seeger, C. Sürgers, I. M. Pop, and W. Wernsdorfer, "Onset of phase diffusion in high kinetic inductance granular aluminum micro-SQUIDs", Supercond. Sci. Technol. **32**, 125008 (2019).

[141] J. L. Chen, "Magnetic response of the superconducting thin film", Physica B **284-288**, 907–908 (2000).

[142] T. H. Boyer, "The force on a magnetic dipole", Am. J. Phys. **56**, 688–692 (1988).

[143] D. E. Kiselov, M. A. Skvortsov, and M. V. Feigel'man, "Gapful electrons in a vortex core in granular superconductors", arXiv, `10.21468/SciPostPhys.15.1.008` (2022).

[144] N. Maleeva, L. Grünhaupt, T. Klein, F. Levy-Bertrand, O. Dupre, M. Calvo, F. Valenti, P. Winkel, F. Friedrich, W. Wernsdorfer, A. V. Ustinov, H. Rotzinger, A. Monfardini, M. V. Fistul, and I. M. Pop, "Circuit quantum electrodynamics of granular aluminum resonators", Nat. Commun. **9**, 1–7 (2018).

[145] P. Winkel, "Superconducting quantum circuits for hybrid architectures", dissertation (Karlsruhe Institute of Technology, 2020).

[146] I. Takmakov, "Minimizing the discrimination time for quantum states of an artificial atom", dissertation (Karlsruhe Institute of Technology, 2022).

[147] D. J. Parker, M. Savytskyi, W. Vine, A. Laucht, T. Duty, A. Morello, A. L. Grimsmo, and J. J. Pla, "Degenerate Parametric Amplification via Three-Wave Mixing Using Kinetic Inductance", Phys. Rev. Appl. **17**, 034064 (2022).

[148] M. Xu, R. Cheng, Y. Wu, G. Liu, and H. X. Tang, "Magnetic Field-Resilient Quantum-Limited Parametric Amplifier", PRX Quantum **4**, 010322 (2023).

[149] W.-C. Chien, Y.-H. Chang, C. X. Lu, Y.-Y. Ting, C.-S. Wu, S.-D. Lin, and W. Kuo, "Large parametric amplification in kinetic inductance dominant resonators based on 3 nm-thick epitaxial superconductors", Mater. Quantum Technol. **3**, 025005 (2023).

[150] M. V. P. Altoé, A. Banerjee, C. Berk, A. Hajr, A. Schwartzberg, C. Song, M. Alghadeer, S. Aloni, M. J. Elowson, J. M. Kreikebaum, E. K. Wong, S. M. Griffin, S. Rao, A. Weber-Bargioni, A. M. Minor, D. I. Santiago, S. Cabrini, I. Siddiqi, and D. F. Ogletree, "Localization and Mitigation of Loss in Niobium Superconducting Circuits", PRX Quantum **3**, 020312 (2022).

[151] A. Kou, W. C. Smith, U. Vool, I. M. Pop, K. M. Sliwa, M. Hatridge, L. Frunzio, and M. H. Devoret, "Simultaneous Monitoring of Fluxonium Qubits in a Waveguide", Phys. Rev. Appl. **9**, 064022 (2018).

[152] J. N. Voss, Y. Schön, M. Wildermuth, D. Dorer, J. H. Cole, H. Rotzinger, and A. V. Ustinov, "Eliminating Quantum Phase Slips in Superconducting Nanowires", ACS Nano **15**, 4108–4114 (2021).

[153] R. Barends, J. Kelly, A. Megrant, D. Sank, E. Jeffrey, Y. Chen, Y. Yin, B. Chiaro, J. Mutus, C. Neill, P. O'Malley, P. Roushan, J. Wenner, T. C. White, A. N. Cleland, and J. M. Martinis, "Coherent Josephson Qubit Suitable for Scalable Quantum Integrated Circuits", Phys. Rev. Lett. **111**, 080502 (2013).

[154] T. W. Larsen, K. D. Petersson, F. Kuemmeth, T. S. Jespersen, P. Krogstrup, J. Nygård, and C. M. Marcus, "Semiconductor-Nanowire-Based Superconducting Qubit", Phys. Rev. Lett. **115**, 127001 (2015).

[155] V. Brosco, G. Serpico, V. Vinokur, N. Poccia, and U. Vool, "Superconducting qubit based on twisted cuprate van der Waals heterostructures", arXiv, `10.48550/arXiv.2308.00839` (2023).

[156] W. C. Smith, A. Kou, U. Vool, I. M. Pop, L. Frunzio, R. J. Schoelkopf, and M. H. Devoret, "Quantization of inductively shunted superconducting circuits", Phys. Rev. B **94**, 144507 (2016).

[157] M. Baker, "1,500 scientists lift the lid on reproducibility - Nature", Nature **533**, 452–454 (2016).

[158] C. Wang, C. Axline, Y. Y. Gao, T. Brecht, Y. Chu, L. Frunzio, M. H. Devoret, and R. J. Schoelkopf, "Surface participation and dielectric loss in superconducting qubits", Appl. Phys. Lett. **107**, 162601 (2015).

[159] I. M. Pop, B. Douçot, L. Ioffe, I. Protopopov, F. Lecocq, I. Matei, O. Buisson, and W. Guichard, "Experimental demonstration of Aharonov-Casher interference in a Josephson junction circuit", Phys. Rev. B **85**, 094503 (2012).

[160] K. K. Likharev, "Superconducting weak links", Rev. Mod. Phys. **51**, 101–159 (1979).

[161] A. F. Andreev, "Thermal conductivity of the intermediate state of superconductors", Sov. Phys. JETP **19**, 1228–1231 (1964).

[162] I. O. Kulik, "Macroscopic Quantization and the Proximity Effect in S-N-S Junctions", Sov. Phys. JETP **30**, 944–950 (1970).

[163] G. de Lange, B. van Heck, A. Bruno, D. J. van Woerkom, A. Geresdi, S. R. Plissard, E. P. A. M. Bakkers, A. R. Akhmerov, and L. DiCarlo, "Realization of Microwave Quantum Circuits Using Hybrid Superconducting-Semiconducting Nanowire Josephson Elements", Phys. Rev. Lett. **115**, 127002 (2015).

[164] G. Butseraen, A. Ranadive, N. Aparicio, K. Rafsanjani Amin, A. Juyal, M. Esposito, K. Watanabe, T. Taniguchi, N. Roch, F. Lefloch, and J. Renard, "A gate-tunable graphene Josephson parametric amplifier", Nat. Nanotechnol. **17**, 1153–1158 (2022).

[165] M. Hays, V. Fatemi, D. Bouman, J. Cerrillo, S. Diamond, K. Serniak, T. Connolly, P. Krogstrup, J. Nygård, A. L. Yeyati, A. Geresdi, and M. H. Devoret, "Coherent manipulation of an Andreev spin qubit", Science **373**, 430–433 (2021).

[166] M. Pita-Vidal, A. Bargerbos, R. Žitko, L. J. Splitthoff, L. Grünhaupt, J. J. Wesdorp, Y. Liu, L. P. Kouwenhoven, R. Aguado, B. van Heck, A. Kou, and C. K. Andersen, "Direct manipulation of a superconducting spin qubit strongly coupled to a transmon qubit", Nat. Phys. **19**, 1110–1115 (2023).

[167] W. Haberkorn, H. Knauer, and J. Richter, "A theoretical study of the current-phase relation in Josephson contacts", Phys. Status Solidi A **47**, K161–K164 (1978).

[168] K. Böttcher and T. Kopp, "Multichannel dc Josephson effect in ballistic point contacts", Phys. Rev. B **55**, 11670–11687 (1997).

[169] C. Kittel, *Introduction to Solid State Physics*, Table 1 in Chap. 6 (Wiley John + Sons, Nov. 2004).

[170] L. Glazman and G. Catelani, "Bogoliubov quasiparticles in superconducting qubits", SciPost Phys. Lect. Notes, 031 (2021).

[171] K. M. Schep and G. E. W. Bauer, "Transport through dirty interfaces", Phys. Rev. B **56**, 15860–15872 (1997).

[172] K. K. Likharev and A. B. Zorin, "Theory of the Bloch-wave oscillations in small Josephson junctions", J. Low Temp. Phys. **59**, 347–382 (1985).

[173] A. A. Kirmani, M. Dzero, and A. Levchenko, "Quasiclassical circuit theory of contiguous disordered multiband superconductors", Phys. Rev. Res. **1**, 033208 (2019).

[174] P. W. Brouwer and C. W. J. Beenakker, "Anomalous temperature dependence of the supercurrent through a chaotic Josephson junction", Chaos, Solitons Fractals **8**, 1249–1260 (1997).

[175] I. O. Kulik and A. Omel'yanchuk, "Contribution to the microscopic theory of the Josephson effect in superconducting bridges", JETP Lett. **21**, 216–219 (1975).

[176] S. Fritz, L. Radtke, R. Schneider, M. Weides, and D. Gerthsen, "Optimization of Al/AlOx/Al-layer systems for Josephson junctions from a microstructure point of view", J. Appl. Phys. **125**, 165301 (2019).

[177] M. J. Cyster, J. S. Smith, J. A. Vaitkus, N. Vogt, S. P. Russo, and J. H. Cole, "Effect of atomic structure on the electrical response of aluminum oxide tunnel junctions", Phys. Rev. Res. **2**, 013110 (2020).

[178] M. J. Cyster, J. S. Smith, N. Vogt, G. Opletal, S. P. Russo, and J. H. Cole, "Simulating the fabrication of aluminium oxide tunnel junctions", npj Quantum Inf. **7**, 1–12 (2021).

[179] T. Aref, A. Averin, S. van Dijken, A. Ferring, M. Koberidze, V. F. Maisi, H. Q. Nguyend, R. M. Nieminen, J. P. Pekola, and L. D. Yao, "Characterization of aluminum oxide tunnel barriers by combining transport measurements and transmission electron microscopy imaging", J. Appl. Phys. **116**, `10.1063/1.4893473` (2014).

[180] L. J. Zeng, S. Nik, T. Greibe, P. Krantz, C. M. Wilson, P. Delsing, and E. Olsson, "Direct observation of the thickness distribution of ultra thin AlOx barriers in Al/AlOx/Al Josephson junctions", J. Phys. D: Appl. Phys. **48**, 395308 (2015).

[181] L. D. Landau and E. M. Lifshitz, *Quantum Mechanics* (Pergamon, Oxford, England, UK, 1977).

[182] A. Wallraff, A. Lukashenko, C. Coqui, A. Kemp, T. Duty, and A. V. Ustinov, "Switching current measurements of large area Josephson tunnel junctions", Rev. Sci. Instrum. **74**, 3740–3748 (2003).

[183] M. L. Della Rocca, M. Chauvin, B. Huard, H. Pothier, D. Esteve, and C. Urbina, "Measurement of the Current-Phase Relation of Superconducting Atomic Contacts", Phys. Rev. Lett. **99**, 127005 (2007).

[184] R. Lescanne, L. Verney, Q. Ficheux, M. H. Devoret, B. Huard, M. Mirrahimi, and Z. Leghtas, "Escape of a Driven Quantum Josephson Circuit into Unconfined States", Phys. Rev. Appl. **11**, 014030 (2019).

[185] A. Blais, J. Gambetta, A. Wallraff, D. I. Schuster, S. M. Girvin, M. H. Devoret, and R. J. Schoelkopf, "Quantum-information processing with circuit quantum electrodynamics", Phys. Rev. A **75**, 032329 (2007).

[186] A. Blais, A. L. Grimsmo, S. M. Girvin, and A. Wallraff, "Circuit quantum electrodynamics", Rev. Mod. Phys. **93**, 025005 (2021).

[187] S. Friedland, "Inverse eigenvalue problems", Linear Algebra Appl. **17**, 15–51 (1977).

[188] S. Friedland, J. Nocedal, and M. L. Overton, "The formulation and analysis of numerical methods for inverse eigenvalue problems", SIAM J. Numer. Anal. **24**, 634–667 (1987).

[189] M. T. Chu, "Inverse eigenvalue problems", SIAM Rev. **40**, 1–39 (1998).

[190] M. Chu and G. Golub, *Inverse Eigenvalue Problems: Theory, Algorithms, and Applications* (Oxford University Press, June 2005).

[191] M. J. Peterer, S. J. Bader, X. Jin, F. Yan, A. Kamal, T. J. Gudmundsen, P. J. Leek, T. P. Orlando, W. D. Oliver, and S. Gustavsson, "Coherence and Decay of Higher Energy Levels of a Superconducting Transmon Qubit", Phys. Rev. Lett. **114**, 010501 (2015).

[192] E. Xie, F. Deppe, M. Renger, D. Repp, P. Eder, M. Fischer, J. Goetz, S. Pogorzalek, K. G. Fedorov, A. Marx, and R. Gross, "Compact 3D quantum memory", Appl. Phys. Lett. **112**, 10.1063/1.5029514 (2018).

[193] E. Xie, "Scalable 3d quantum memory", PhD thesis (Technische Universität München, 2019).

[194] F. Dyson, "A meeting with Enrico Fermi - Nature", Nature **427**, 297 (2004).

[195] M. Tinkham, *Introduction to Superconductivity* (Dover Publications Inc., Mineola, NY, USA, June 2004).

[196] J. Braumüller, L. Ding, A. P. Vepsäläinen, Y. Sung, M. Kjaergaard, T. Menke, R. Winik, D. Kim, B. M. Niedzielski, A. Melville, J. L. Yoder, C. F. Hirjibehedin, T. P. Orlando, S. Gustavsson, and W. D. Oliver, "Characterizing and Optimizing Qubit Coherence Based on SQUID Geometry", Phys. Rev. Appl. **13**, 054079 (2020).

[197] R. Gao, F. Wu, H. Sun, J. Chen, H. Deng, X. Ma, X. Miao, Z. Song, X. Wan, F. Wang, T. Xia, M. Ying, C. Zhang, Y. Shi, H.-H. Zhao, and C. Deng, "Unraveling the role of disorderness in superconducting materials on qubit coherence", arXiv, 10.48550/arXiv.2310.06621 (2023).

[198] M. Pita-Vidal, A. Bargerbos, C.-K. Yang, D. J. van Woerkom, W. Pfaff, N. Haider, P. Krogstrup, L. P. Kouwenhoven, G. de Lange, and A. Kou, "Gate-Tunable Field-Compatible Fluxonium", Phys. Rev. Appl. **14**, 064038 (2020).

[199] J. Lisenfeld, A. Bilmes, A. Megrant, R. Barends, J. Kelly, P. Klimov, G. Weiss, J. M. Martinis, and A. V. Ustinov, "Electric field spectroscopy of material defects in transmon qubits", npj Quantum Inf. **5**, 1–6 (2019).

[200] J. B. Hertzberg, E. J. Zhang, S. Rosenblatt, E. Magesan, J. A. Smolin, J.-B. Yau, V. P. Adiga, M. Sandberg, M. Brink, J. M. Chow, and J. S. Orcutt, "Laser-annealing Josephson junctions for yielding scaled-up superconducting quantum processors", npj Quantum Inf. **7**, 1–8 (2021).

[201] P. Groszkowski, A. Di Paolo, A. L. Grimsmo, A. Blais, D. I. Schuster, A. A. Houck, and J. Koch, "Coherence properties of the 0-π qubit", New J. Phys. **20**, 043053 (2018).

[202] A. Gyenis, P. S. Mundada, A. Di Paolo, T. M. Hazard, X. You, D. I. Schuster, J. Koch, A. Blais, and A. A. Houck, "Experimental Realization of a Protected Superconducting Circuit Derived from the 0−π Qubit", PRX Quantum **2**, 010339 (2021).

[203] G. Rastelli and I. M. Pop, "Steps towards current metrology", Nat. Phys. **19**, 771–772 (2023).

[204] O. V. Astafiev, L. B. Ioffe, S. Kafanov, Y. A. Pashkin, K. Y. Arutyunov, D. Shahar, O. Cohen, and J. S. Tsai, "Coherent quantum phase slip", Nature **484**, 355–358 (2012).

[205] J. T. Peltonen, Z. H. Peng, Y. P. Korneeva, B. M. Voronov, A. A. Korneev, A. V. Semenov, G. N. Gol'tsman, J. S. Tsai, and O. V. Astafiev, "Coherent dynamics and decoherence in a superconducting weak link", Phys. Rev. B **94**, 180508 (2016).

[206] A. M. Bozkurt, J. Brookman, V. Fatemi, and A. R. Akhmerov, "Double-Fourier engineering of Josephson energy-phase relationships applied to diodes", arXiv, `10.48550/arXiv.2307.04830` (2023).

[207] S. E. Nigg, H. Paik, B. Vlastakis, G. Kirchmair, S. Shankar, L. Frunzio, M. H. Devoret, R. J. Schoelkopf, and S. M. Girvin, "Black-Box Superconducting Circuit Quantization", Phys. Rev. Lett. **108**, 240502 (2012).

[208] M. H. Ansari, "Superconducting qubits beyond the dispersive regime", Phys. Rev. B **100**, 024509 (2019).

[209] R.-P. Riwar and D. P. DiVincenzo, "Circuit quantization with time-dependent magnetic fields for realistic geometries", npj Quantum Inf. **8**, 1–12 (2022).

[210] A. Miano, V. R. Joshi, G. Liu, W. Dai, P. D. Parakh, L. Frunzio, and M. H. Devoret, "Hamiltonian Extrema of an Arbitrary Flux-Biased Josephson Circuit", PRX Quantum **4**, 030324 (2023).

[211] L. DiCarlo, J. M. Chow, J. M. Gambetta, L. S. Bishop, B. R. Johnson, D. I. Schuster, J. Majer, A. Blais, L. Frunzio, S. M. Girvin, and R. J. Schoelkopf, "Demonstration of two-qubit algorithms with a superconducting quantum processor", Nature **460**, 240–244 (2009).

[212] V. Negîrneac, H. Ali, N. Muthusubramanian, F. Battistel, R. Sagastizabal, M. S. Moreira, J. F. Marques, W. J. Vlothuizen, M. Beekman, C. Zachariadis, N. Haider, A. Bruno, and L. DiCarlo, "High-Fidelity Controlled-*Z* Gate with Maximal Intermediate Leakage Operating at the Speed Limit in a Superconducting Quantum Processor", Phys. Rev. Lett. **126**, 220502 (2021).

[213] M. A. Rol, F. Battistel, F. K. Malinowski, C. C. Bultink, B. M. Tarasinski, R. Vollmer, N. Haider, N. Muthusubramanian, A. Bruno, B. M. Terhal, and L. DiCarlo, "Fast, High-Fidelity Conditional-Phase Gate Exploiting Leakage Interference in Weakly Anharmonic Superconducting Qubits", Phys. Rev. Lett. **123**, 120502 (2019).

[214] T. Roy, Z. Li, E. Kapit, and D. Schuster, "Two-Qutrit Quantum Algorithms on a Programmable Superconducting Processor", Phys. Rev. Appl. **19**, 064024 (2023).

[215] M. Rymarz, S. Bosco, A. Ciani, and D. P. DiVincenzo, "Hardware-Encoding Grid States in a Nonreciprocal Superconducting Circuit", Phys. Rev. X **11**, 011032 (2021).

[216] W. C. Smith, M. Villiers, A. Marquet, J. Palomo, M. R. Delbecq, T. Kontos, P. Campagne-Ibarcq, B. Douçot, and Z. Leghtas, "Magnifying Quantum Phase Fluctuations with Cooper-Pair Pairing", Phys. Rev. X **12**, 021002 (2022).

[217] P. Campagne-Ibarcq, A. Eickbusch, S. Touzard, E. Zalys-Geller, N. E. Frattini, V. V. Sivak, P. Reinhold, S. Puri, S. Shankar, R. J. Schoelkopf, L. Frunzio, M. Mirrahimi, and M. H. Devoret, "Quantum error correction of a qubit encoded in grid states of an oscillator", Nature **584**, 368–372 (2020).

[218] R. Lescanne, M. Villiers, T. Peronnin, A. Sarlette, M. Delbecq, B. Huard, T. Kontos, M. Mirrahimi, and Z. Leghtas, "Exponential suppression of bit-flips in a qubit encoded in an oscillator", Nat. Phys. **16**, 509–513 (2020).

[219] K. Gramm, L. Lundgren, and O. Beckman, "SQUID Magnetometer for Mangetization Measurements", Phys. Scr. **13**, 93 (1976).

[220] S. Shapiro, "Josephson Currents in Superconducting Tunneling: The Effect of Microwaves and Other Observations", Phys. Rev. Lett. **11**, 80–82 (1963).

[221] N. Crescini, S. Cailleaux, W. Guichard, C. Naud, O. Buisson, K. W. Murch, and N. Roch, "Evidence of dual Shapiro steps in a Josephson junction array", Nat. Phys. **19**, 851–856 (2023).

[222] A. Roy and M. Devoret, "Introduction to parametric amplification of quantum signals with Josephson circuits", C. R. Phys. **17**, 740–755 (2016).

[223] Y. V. Fominov and D. S. Mikhailov, "Asymmetric higher-harmonic SQUID as a Josephson diode", Phys. Rev. B **106**, 134514 (2022).

[224] H. Paik, D. I. Schuster, L. S. Bishop, G. Kirchmair, G. Catelani, A. P. Sears, B. R. Johnson, M. J. Reagor, L. Frunzio, L. I. Glazman, S. M. Girvin, M. H. Devoret, and R. J. Schoelkopf, "Observation of High Coherence in Josephson Junction Qubits Measured in a Three-Dimensional Circuit QED Architecture", Phys. Rev. Lett. **107**, 240501 (2011).

[225] G. Kirchmair, B. Vlastakis, Z. Leghtas, S. E. Nigg, H. Paik, E. Ginossar, M. Mirrahimi, L. Frunzio, S. M. Girvin, and R. J. Schoelkopf, "Observation of quantum state collapse and revival due to the single-photon Kerr effect", Nature **495**, 205–209 (2013).

[226] D. M. Pozar, *Microwave Engineering* (Wiley, Chichester, England, UK, Dec. 2011).

[227] L. Grünhaupt, U. von Lüpke, D. Gusenkova, S. T. Skacel, N. Maleeva, S. Schlör, A. Bilmes, H. Rotzinger, A. V. Ustinov, M. Weides, and I. M. Pop, "An argon ion beam milling process for native AlOx layers enabling coherent superconducting contacts", Appl. Phys. Lett. **111**, 072601 (2017).

[228] A. A. Clerk and D. W. Utami, "Using a qubit to measure photon-number statistics of a driven thermal oscillator", Phys. Rev. A **75**, 042302 (2007).

[229] G. Zhang, Y. Liu, J. J. Raftery, and A. A. Houck, "Suppression of photon shot noise dephasing in a tunable coupling superconducting qubit", npj Quantum Inf. **3**, 1–4 (2017).

[230] D. Willsch and D. Rieger, "Spectroscopy Data and Model Parameters for: Observation of Josephson Harmonics in Tunnel Junctions", `10.26165/JUELICH-DATA/LGRHUH` (2023).

[231] Q. Ficheux, S. Jezouin, Z. Leghtas, and B. Huard, "Dynamics of a qubit while simultaneously monitoring its relaxation and dephasing", Nat. Commun. **9**, 1–6 (2018).

[232] D. C. McKay, T. Alexander, L. Bello, M. J. Biercuk, L. Bishop, J. Chen, J. M. Chow, A. D. Córcoles, D. Egger, S. Filipp, J. Gomez, M. Hush, A. Javadi-Abhari, D. Moreda, P. Nation, B. Paulovicks, E. Winston, C. J. Wood, J. Wootton, and J. M. Gambetta, "Qiskit Backend Specifications for OpenQASM and OpenPulse Experiments", arXiv, `10.48550/arXiv.1809.03452` (2018).

[233] T. Alexander, N. Kanazawa, D. J. Egger, L. Capelluto, C. J. Wood, A. Javadi-Abhari, and D. C. McKay, "Qiskit pulse: programming quantum computers through the cloud with pulses", Quantum Sci. Technol. **5**, 044006 (2020).

[234] J. A. Schreier, A. A. Houck, J. Koch, D. I. Schuster, B. R. Johnson, J. M. Chow, J. M. Gambetta, J. Majer, L. Frunzio, M. H. Devoret, S. M. Girvin, and R. J. Schoelkopf, "Suppressing charge noise decoherence in superconducting charge qubits", Phys. Rev. B **77**, 180502 (2008).

[235] A. Schneider, J. Braumüller, L. Guo, P. Stehle, H. Rotzinger, M. Marthaler, A. V. Ustinov, and M. Weides, "Local sensing with the multilevel ac Stark effect", Phys. Rev. A **97**, 062334 (2018).

[236] J. E. Dennis and R. B. Schnabel, *Numerical methods for unconstrained optimization and nonlinear equations* (Society for Industrial and Applied Mathematics, 1996).

[237] W. H. Press, S. A. Teukolsky, W. T. Vetterling, and B. P. Flannery, *Numerical recipes 3rd edition: the art of scientific computing* (Cambridge University Press, New York, USA, 2007).

[238] J. Nocedal and S. J. Wright, *Numerical optimization*, Springer Series in Operations Research and Financial Engineering (Springer New York, NY, 2006).

[239] TensorFlow Developers, *TensorFlow v2.8.0*, version v2.8.0, TensorFlow Probability v0.15.0 (2022).

[240] C. Berke, E. Varvelis, S. Trebst, A. Altland, and D. P. DiVincenzo, "Transmon platform for quantum computing challenged by chaotic fluctuations", Nat. Commun. **13**, 1–10 (2022).